POLITECNICO
MILANO 1863

SCUOLA DI INGEGNERIA INDUSTRIALE
E DELL'INFORMAZIONE

Response Analysis of a Seven-Turbines Floating Offshore Wind Farm in the North Sea with Different Turbulent Inflows

TESI DI LAUREA MAGISTRALE IN
ENERGY ENGINEERING
INGEGNERIA ENERGETICA

Author: **Alessio Scaparrotti**

Student ID: 977859
Advisor: Sara Muggiasca
Co-advisor: Alessandro Fontanella
Academic Year: 2021-22

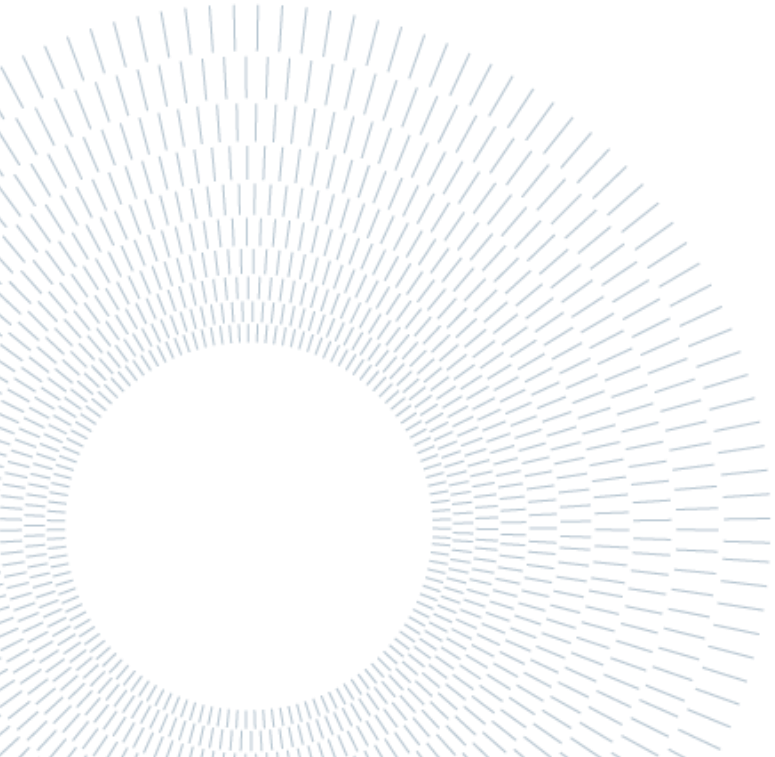

Abstract

In this master thesis the response of a hexagonal 5D staggered layout wind farm, composed by seven IEA 15-MW Floating Offshore Wind Turbines, with the environmental conditions of a North-Sea site, has been evaluated.
Three different turbulent wind inflows have been applied to the plant: two are characterized by a Kaimal spectrum, with coherence in all the three wind components and just in the horizontal component, respectively, and the remaining one is a Mann turbulent wind.
The software FAST.Farm has been the tool to simulate the farm operation, while the turbulent wind time-series data have been generated with TurbSim, for the Kaimal cases, and Mann Turbulence Generator, for the Mann one.
The first step has been to test the methodology on a farm with two 8D distanced aligned turbines, to then apply it to the plant configuration under analysis.
Lastly, a comparison between the floating farm and a monopile farm, with the same layout and environmental conditions, has been set up.
As a result, the floating configuration under study has been evidenced to be good from all the analyzed points of view; in particular, just two of the seven rotors operate in waked conditions and the layout ensures acceptable plant performance and relatively contained platform motions and reasonable axial stresses and short-terms fatigue damages for all the turbines and inflows.
Using instead bottom-fixed turbines would be better, in terms of quantity and quality of extractable power, but unfeasible with these environmental conditions; the water depth characterizing the site (200m) does not permit the installation of this type of technology. The comparison, in fact, has not been made to be end in itself, but it has permitted to find out and confirm some of the conclusions concerning the floating case.
The real contributions of this master thesis, anyway, have been those of increasing the robustness of the FAST.Farm use and developing models for the future studies of Politecnico di Milano's Galleria del Vento. The latters are, in fact, focusing on the offshore floating wind energy, contributing to the spread of this promising technology, and so to the decarbonisation.

Key-words: Floating Offshore Wind Farm, FAST.Farm, Turbulence, Wakes, Wind Turbines, Wind Energy

Abstract in italiano

In questa tesi magistrale viene analizzato il responso di un parco eolico esagonale di sette IEA 15-MW Floating Offshore Wind Turbines sfalsate di 5D, con le condizioni ambientali di un sito nel Mare del Nord.
L'impianto è stato sottoposto a tre tipologie di flussi ventosi turbolenti differenti: due caratterizzati da uno spettro di Kaimal, rispettivamente con coerenza in tutte e tre le componenti del vento e solo nella componente orizzontale, e il rimanente consiste in una turbolenza di Mann.
Lo strumento utilizzato per simulare il funzionamento della centrale è stato FAST.Farm, mentre i dati delle serie temporali del vento turbolento sono stati generati con TurbSim, per i casi di Kaimal, e Mann Turbulence Generator, per quello di Mann.
Il punto di partenza è stato testare la metodologia su un impianto di due turbine allineate distanziate di 8D, per poi applicarlo alla configurazione oggetto dello studio.
Infine è stato condotto un paragone tra il parco galleggiante e uno con fondazioni monopile, con la stesso assetto e stesse condizioni ambientali.
Come risultato, la configurazione galleggiante studiata è risultata essere buona da tutti i punti di vista analizzati; in particolare, solo due dei sette aereogeneratori subiscono le scie degli altri e la disposizione garantisce prestazioni accettabili e movimenti della piattaforma relativamente contenuti e ragionevoli sforzi assiali e danni a fatica a breve termine ragionevoli per tutte le turbine e i flussi considerati.
Utilizzare turbine monopile sarebbe meglio in termini di quantità e qualità della potenza estraibile, ma infattibile con queste condizioni ambientali; la profondità dell'acqua del sito (200m) non permette l'installazione di questo tipo di tecnologia. Il paragone, infatti, non è stato fatto per essere fine a se stesso, ma ha permesso di trovare e confermare alcune delle conclusioni riguardanti il caso galleggiante.
Il vero contributo di questa tesi magistrale, tuttavia, è stato quello di rafforzare l'utilizzo di FAST.Farm e sviluppare modelli per i futuri studi della Galleria del Vento del Politecnico di Milano. Questi sono infatti focalizzati sull'energia eolica offshore galleggiante, contribuendo alla diffusione di questa tecnologia promettente e, quindi, alla decarbonizzazione.

Parole chiave: Parchi Eolici Offshore galleggianti, FAST.Farm, Turbolenza, Scie, Turbine Eoliche, Energia Eolica

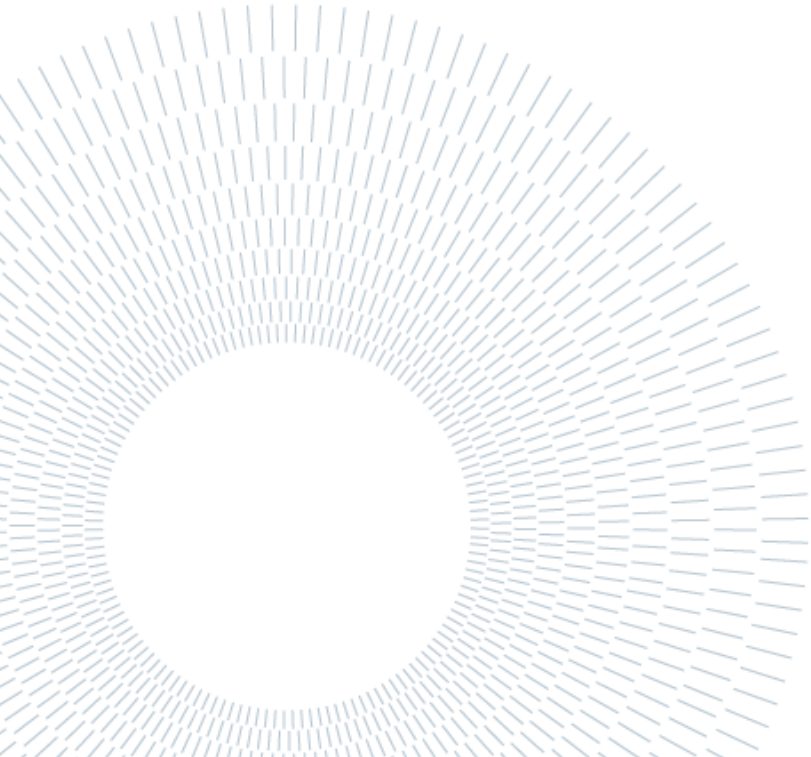

Contents

Introduction

Wind represent one of the most important renewable energy sources. It can be considered an indirect form of solar energy: the sun, infact, leads to different air masses heating, which reflects into density inhomogeneities and so into convective motions. The kinetic energy associated to the air movements can be converted into mechanical power by wind turbines and then, thanks to electrical machines, into electrical power, which is injected into the grid.
Wind energy plays a key role in the transition toward decarbonisation of the world and in particular of Italy. In fact, in 2022 the Italian actual electricity generation from wind was 20353.3 GWh, consisting in about 7.4% of the 2022 Italian actual electricity generation [1], and for about 6.4% of the 2022 Italian load [2], and it is expected to become at least 25100 GWh within 2030, according with the objectives of Piano Nazionale Integrato per l'Energia e il Clima (PNEIC) [3].
Moreover the Italian wind power installed capacity was 11.70 GW in 2022 [4], i.e. about 9.9% of the total Italian installed capacity, and it should reach 30.17 GW according to the PNEIC pathway [3]. The increase of the wind installed capacity in Italy has been visible in the last decade, as confirmed from Figure 1 [5], but, to meet the PNEIC objectives, wind installed capacity must continue not only to rise, but also a boost of the growing rate is needed.

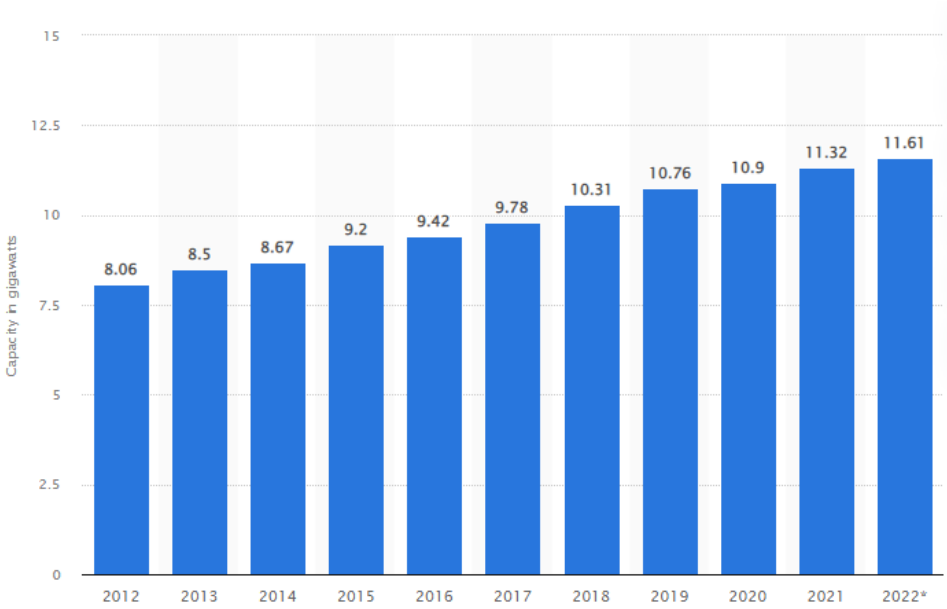

Figure 1: Total installed wind power capacity in Italy from 2012 to 2022. Figure by Statista.

The spread of wind energy technologies is due to Research & Development (R&D) and Learning-By-Doing mechanisms, which make these power production solutions always more profitable and efficient. R&D consists in scientific studies conducted in specific institutes, while Learning-By-Doing consists in gaining and consolidating design skills from the increase of the amount of effective on-field installation. Both these two processes are more and more focusing on offshore wind technologies.

The wind over sea areas represents in fact a huge potential to be exploited: the energy content is generally much greater with respect to the onshore wind; this is because of the greater and more constant wind velocity, greater full load hours (up to 4500 h [6]), greater and more available sites and lower complexity of the terrain. Moreover there are less visual and environmental impact. On the other hand, offshore wind technologies have higher specific plant costs: 3000÷4000 €/KW vs 1400÷2000 €/KW of the onshore ones in 2021 [6]. Farms in the sea, in fact, require on-field installation with vessels, and are characterized by high operation and maintenance (O&M) costs. The power losses are higher too, for the long submarine cables which have to arrive till the land. They also suffer from harsh conditions in term of loads and corrosion, higher turbulence and gusts content of the wind, causing worse power quality.

Anyway offshore wind power plant are becoming more and more profitable, as confirmed by the National Renewables Energy Laboratory (NREL) forecasts. The latters concern the Levelized Cost of Electricity (LCOE), one of the most relevant parameters to analyse the profitability of an electricity production plant, and the capital and fixed operational expenditure (CAPEX and fixed OPEX or fixed O&M) for offshore wind (Figure 2) [7]. They are differentiated into a Conservative Scenario (turbine size remaining consistent with the one of the technology solutions available today in the markets), a Moderate Scenario (turbine size increasing at a rate commensurate with the recent years growth) and an Advanced Scenario (turbine size increasing at a rate that is considerably higher than the one of recent years).

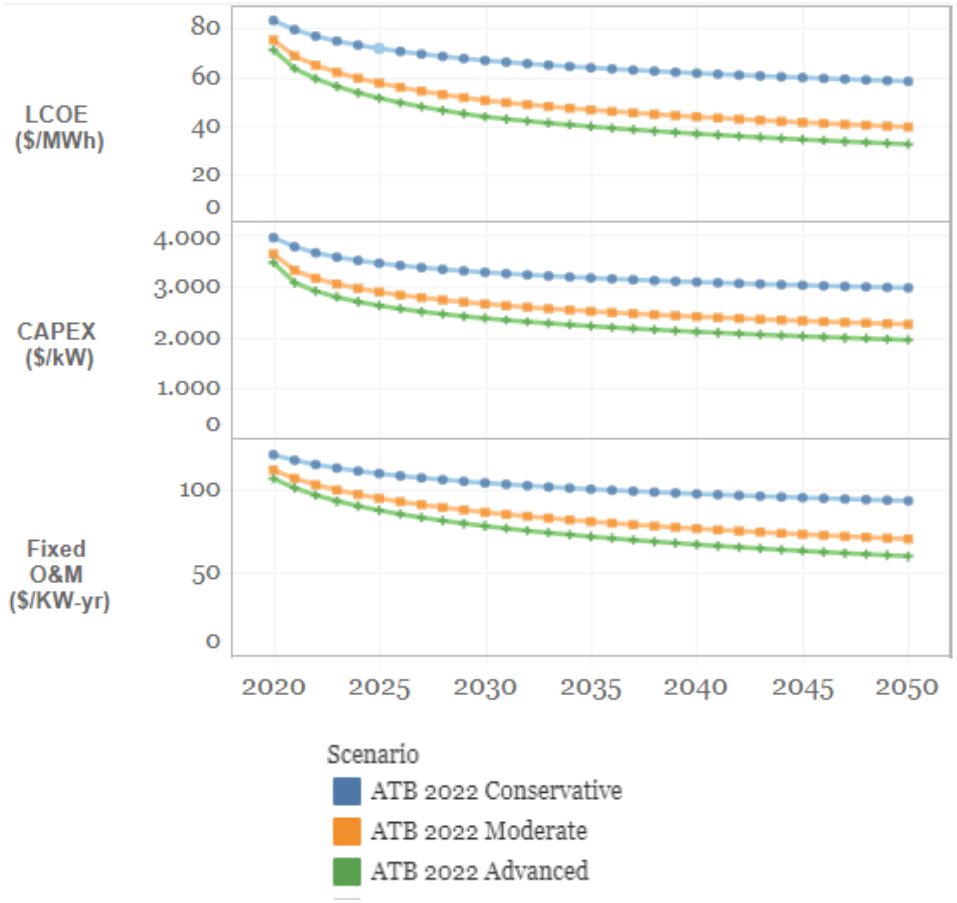

Figure 2: LCOE, CAPEX and fixed O&M Annual Technology Baseline (ATB) NREL projections for offshore wind energy under the hypothesis of Wind Resource Class 3 (from 9.13 m/s to 9.31 m/s wind speed).

Offshore wind farms are composed by groupings of wind turbines, which can be distinguished into bottom-fixed and floating.

The first are fixed to the seabed thanks to a substructure, while the second, object of the present analysis, are based on floating devices anchored through mooring lines. Different floating foundation typologies exist and the one used in this thesis will be presented later (Section 1.4).

Floating wind turbines permits to exploit wind of deep marine areas (depth higher than 60 m), reducing the visual and environmental impact and increasing the possible dimensions of the plant. However, all the disadvantages of offshore wind farms, mentioned above, get worse with a floating configuration, making the design more complex to cope with them: bigger dimensions of the farm and distances from the coast means higher capital costs and maintenance expenditures, loads (from waves for example), corrosion, blades ice formation and turbulence. For these reasons the reliability has to be the maximum possible, to reduce failures probability and so the number of repair operations.

A comparison between the CAPEX of bottom fixed turbines and floating ones in 2020 is shown in Figure 3 [7]. In this picture the balance of system (BOS) consists in the upfront CAPEX

for installing the wind plant and its components excluding the turbine (accounted in CAPEX Turbine). Soft costs, instead, cover insurance, project financing, construction contingency costs, and decommissioning costs.

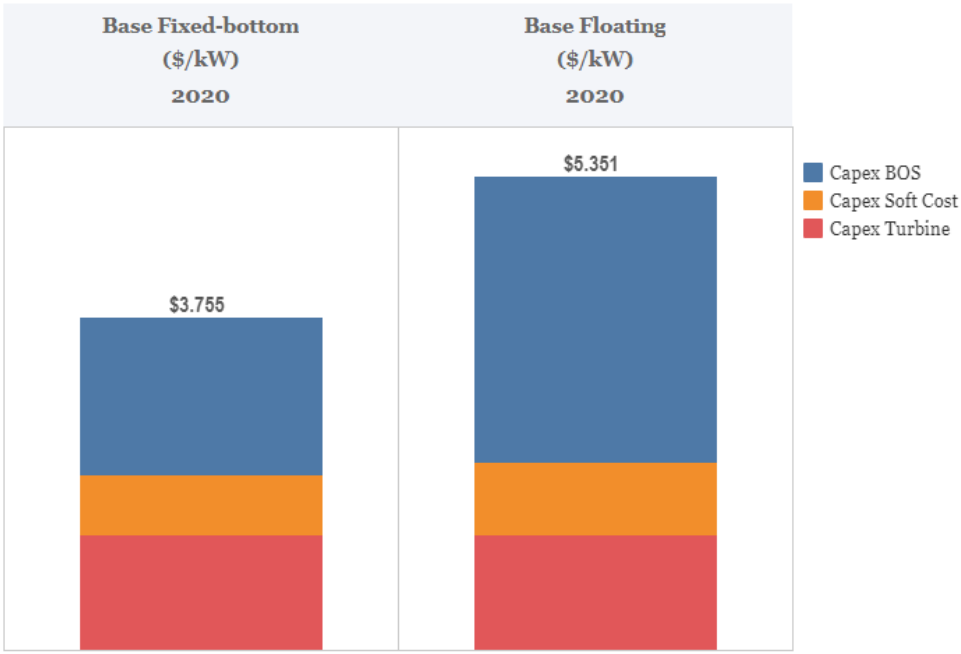

Figure 3: NREL CAPEX comparison between fixed bottom offshore wind turbines and offshore floating ones in 2020.

Thesis Motivations and Goals

The feasibility of a floating wind farm should be evaluated considering each specific case, accounting for meteorological data and forecasts of the resource (wind), local energy market and identification of the optimal layout.

To optimize the LCOE, the arrangement of the turbines in the space should be studied with particular care; the wakes of the upwind rotors, characterized by lower mean velocity and higher turbulence with respect to the undisturbed flux, in fact, reduce the performance (in terms of extracted power) of the downwind ones and increase the fatigue damages.

The effect of this issue could be lowered as much as possible by adopting particular configuration, such as the one analysed in the present work.

The aim of this analysis is to asses the response of a seven-turbines offshore floating wind farm configuration placed in the North Sea and subjected to three different turbulent inflow typologies.

The tool used to simulate the farm operation has been FAST.Farm; the real contributions of this master thesis have been, in fact, to make the use of this software

more robust to develop models for the researches of the Politecnico di Milano's Mechanical Department, concerning the wind energy.

Thesis Organization

The present document is organized as follow:

- Chapter 1 is a description of the IEA 15-MW Floating Offshore Wind Turbine, the turbine model adopted;
- Chapter 2 introduces the adopted tools, which have been FAST.Farm (for the farm operation simulations) TurbSim and Mann Turbulence Generator (to generate the turbulent wind time-series data) and MLife (to asses the fatigue damages);
- In Chapter 3 the methodology on the basis of the study is tested on a farm of two 8D distanced aligned turbines;
- Chapter 4 is an analysis of the response of the seven-turbines layout under study with the application of three different turbulent inflow typologies;
- Chapter 5 is a comparison among the analysed floating farm and a monopile plant with an analogous layout;
- Chapter 6 summarizes the general conclusions and depicts the possible future developments.

1 IEA Wind 15-Megawatt Offshore Reference Wind Turbine with UMaine VolturnUS-S Reference Platform

International Energy Agency (IEA) Wind 15-Megawatt Offshore Reference Wind Turbine [8], coupled with the University of Maine (UMaine) VolturnUS-S Reference Platform [9], represent the subject of this study, in which they are together referred to as IEA 15-MW Floating Offshore Wind Turbine. A reference wind turbine serves as open benchmarks for wind energy studies and has a publicly available design, typically realistic but not fully optimized.

This reference wind turbine has been designed by National Renewable Energy Laboratory (NREL), sponsored by the U.S. Department of Energy, together with Technical University of Denmark (DTU), sponsored by the European Union's H2020 Program, through the second work package of International Energy Agency (IEA) Wind Task 37 concerning Wind Energy Systems Engineering: Integrated RD&D.
Its rated extractable power is 15 MW, as indicated in the name.

The original design was for the offshore monopile configuration but it has been adapted for floating offshore by University of Maine, by adding a floating platform and changing the tower proprieties and, slightly, the control dynamic.
A rendering of the offshore floating reference turbine can be appreciated in Figure 1.1, while Figure 1.2 is a representation of the coordinates reference system used to the define the platform-related quantities. The system components, instead, are depicted in plan and elevation views in Figure 1.3. The system comprises a four-column, three-radial and one central, steel semisubmersible platform held on station via a three-line catenary mooring array. The tower, different from the original one of bottom-fixed case, is connected to the central column of the platform. The rotor nacelle assembly (RNA) is placed at a hub height of 150 m above the still water line (SWL). When installed, the platform has a draft of 20 m with a 15 m freeboard to the upper deck of the columns.The mooring lines of the spread catenary system span radially to anchors located 837.60 m from the tower's centreline.

The completely assembled unit displaces 20.206 m^3 of 1.025 kg/m^3-dense seawater, corresponding to a 1.263t tower, a 991t RNA, and a 17.839t ballasted platform with 6.065kN of mooring vertical pretension.

Figure 1.1: Rendering of the IEA 15-MW Offshore Reference Wind Turbine with UMaine VolturnUS-S Reference Platform. Figure courtesy of the University of Maine.

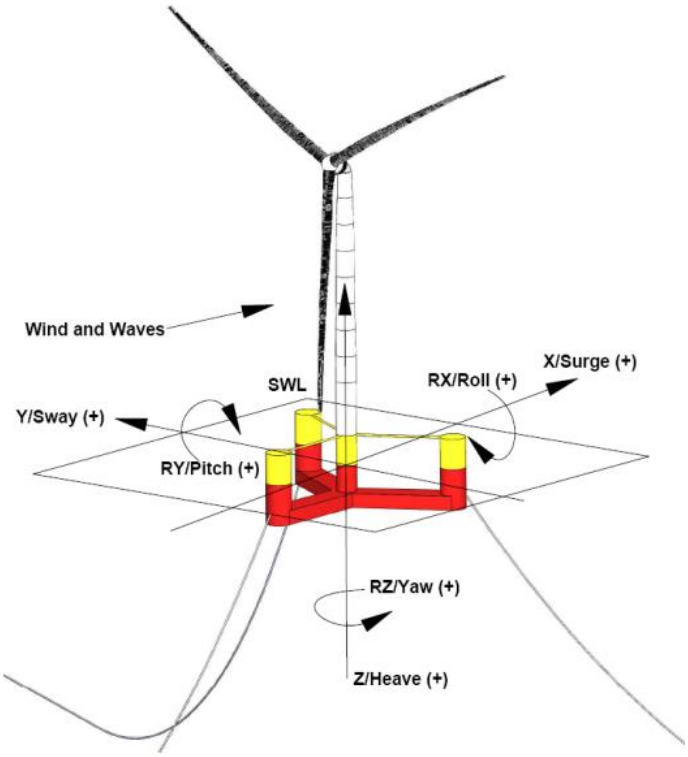

Figure 1.2: IEA 15-MW Floating Offshore Wind Turbine reference coordinate system. Figure courtesy of the University of Maine.

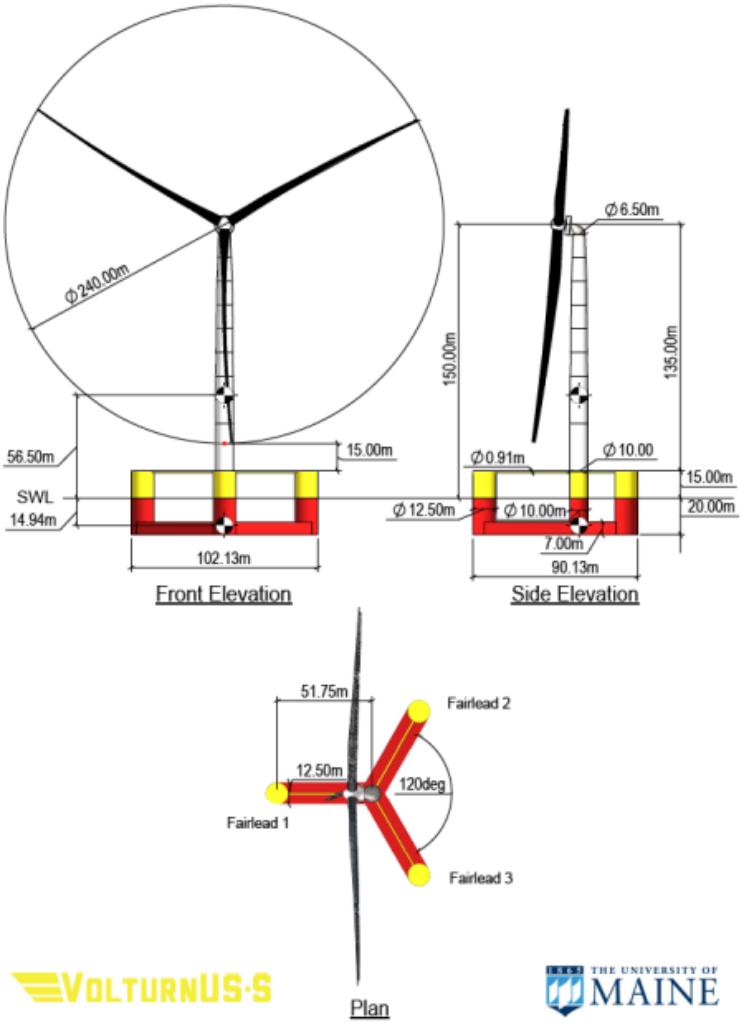

Figure 1.3: Views of the IEA 15-MW Floating Offshore Wind Turbine's components with their dimensions. Figure courtesy of the University of Maine.

1.1. Blade Proprieties

The IEA Wind 15-MW reference turbine blades are long 117 m, with a diameter of 5.2 m at the root, and a maximum chord of 5.77 m in correspondence of around 20% span. The overall blade mass is around 65 metric tons, with a design to achieve a power coefficient (c_p) of 0.489, based on DTU FFA-W3 series of airfoils (Figure 1.4).

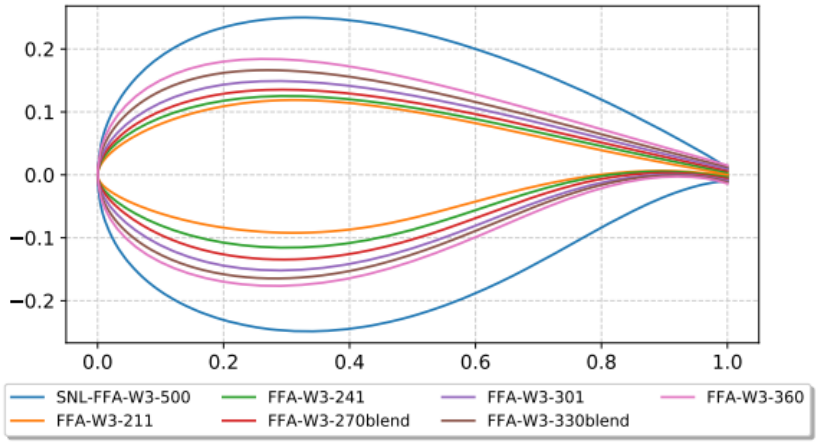

Figure 1.4: DTU FFA-W3 airfoil family used in the IEA Wind 15-MW blade design.

1.2. Nacelle, Drivetrain and Hub Proprieties

The IEA Wind 15-MW Reference Wind Turbine has a direct-drive, simple and compact nacelle layout, encompassing a permanent-magnet, synchronous, radial flux generator with a full load electrical efficiency equals to 0.9655. A yaw system, based on double-row, angular, contact ball bearings, responsible for the nacelle orientation is present too. Its scope is to make the rotor facing the wind in the desired way, acting on the yaw angle, the angle between the rotor axis and the wind main direction. It can also move the nacelle along the vertical axis.

1.3. Tower Proprieties

The floating tower has been designed in order to be adapted to the platform. It has, in fact, higher stiffness requirements than the original NREL-DTU one, because of the increased inertial and gravity loads resulting from platform motion. It has been designed as an isotropic steel tube with free-free boundary conditions. The design is constrained by frequency considerations. In particular, the first fore-aft and side-side natural frequencies, around 0.5 Hz, are outside (above) rotation speed (1P) and blade passing (3P) ranges.

The tower base and hub height are 15 m and 150 m respectively and the total flexible tower length is 129.495 m. The maximum outer diameter and the tower-top one are 10 m and 6.5 m respectively. The mass of the semisubmersible tower is 1.263 t.

1.4. UMaine VolturnUS-S Semisubmersible Platform

The adopted steel semisubmersible reference platform is compound of four columns: three 12.5 m-diameter buoyant columns radially spaced with centres (that are 51.75 m from the tower's vertical axis) and a fourth buoyant column, holding up the platform-tower interface, located at the centre of the platform in the surge-sway plane (Figure 1.3), connected among them. The total mass of the platform on station is 17,854 t. The allowed platform motions, indicated in Figure 1.2, have the following natural frequencies: 0.007 Hz for surge and sway, 0.049 Hz for heave, 0.036 Hz for roll and pitch and 0.011 Hz for Yaw.

1.5. Mooring System Proprieties

The UMaine VolturnUS-S chain mooring system consists of three studless R3 chain catenary lines with a nominal (bar) diameter of 185 mm and a breaking strength of 22 286 kN. Each of them is connected at the fairlead to one of the platform's three outer columns at 14 m below the SWL. The lines span radially to anchors spaced equally at 120 degrees in the surge-sway plane Figure 1.5.
Considering a water depth of 200 m the catenary lines are long 850m and the anchors, placed on the seabed, spaced radially 837.60 m from the tower's centreline.

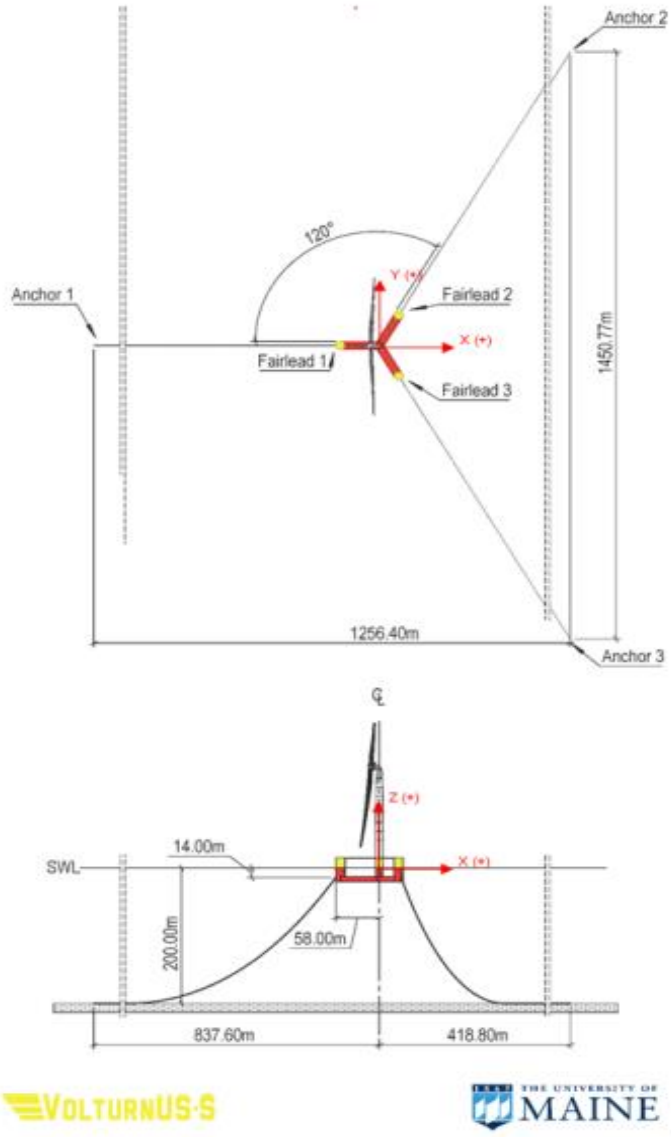

Figure 1.5: Plan (top) and elevation (bottom) views of the mooring system arrangement within the inertia frame. Figure courtesy of the University of Maine.

1.6. Rotor Performance and Control Strategy

Rotor performance strictly depends on the controller behaviour and pitch schedule. The NREL Reference OpenSource Controller (ROSCO) [10], with slightly changes to account for the platform dynamics [9], is the one adopted.

The rotor operates with a minimum rotational speed of 5 rpm; in this way 3-period (3P) interference with the tower natural frequencies is avoided. The rated rotational speed is 7.55 rpm, obtained for a wind velocity of 10.59 m/s. The rotor operates with a

0° pitch setting at the design tip-speed ratio (TSR) of 9, and with positive pitch at low wind speeds to track maximum power maintaining the minimum rotor speed. At the rated wind speed of 10.59 m/s the rotor starts to pitch.
Two active proportional integral (PI) controllers are deployed for the generator torque and blade pitch angles, with saturation limits on rotor speeds and blade pitch angles. The controller operation can be divided into three regions on the basis of the horizontal hub wind velocity (U_{hub}) (Figure 1.6):

- Region 1.5: minimum rotor speed; 3m/s ≤ U_{hub} ≤ 6.98 m/s. A PI controller on the generator torque is used to maintain the minimum rotor speed of 5 rpm. The minimum blade pitch angles are defined such that C_P is maximized.
- Region 2: optimal TSR; 6.98 m/s ≤ U_{hub} ≤ 10.59 m/s. In this range of below-rated wind speeds, the rotor speed is regulated so that the turbine operates at the optimal TSR, using a PI controller on the generator torque;
- Region 3: rated generator torque; 10.59 m/s ≤ U_{hub} ≤ 25 m/s. In above-rated wind velocities, a PI controller on the blade pitch angle regulates the rotor speed with the aim to stay at its rated value, 7.55 rpm.

To determinate the optimal rotor speeds in below-rated operation and the minimum blade pitch angles during minimum rotor speed operation, a Kalman filter-based extended wind speed estimator is employed. In Region 2.5, a setpoint-smoothing methodology [11] to ensure smooth transitions between control regions is implemented. Since the rated rotor speed is reached at rated torque, the Region 2.5 is negligible.
The PI gains for the generator torque and blade pitch controllers, determined with the ROSCO generic tuning methodology [11], are set in the DISCON OpenFAST input file (Section 2.1.1.1).

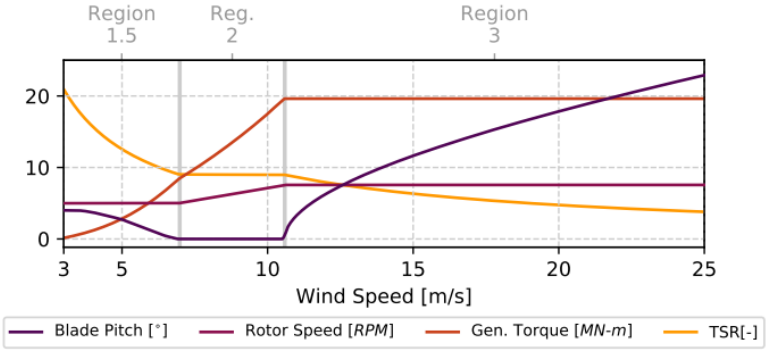

(a) Controller regulation trajectory.

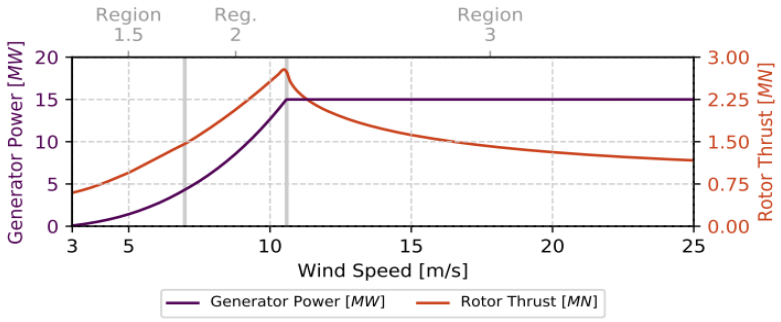

(b) Power and thrust curve.

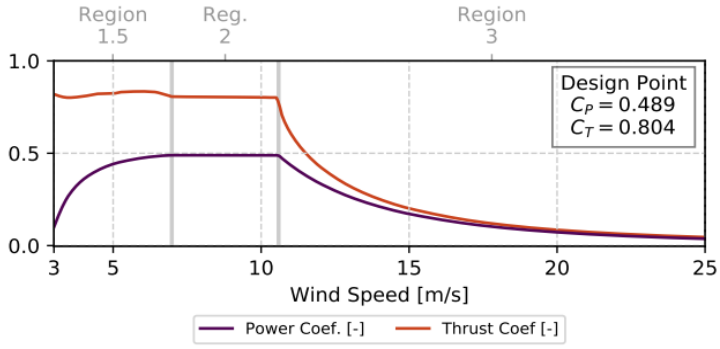

(c) Aerodynamic performance coefficients.

Figure 1.6: Blade element momentum performance and operation of the 15-MW rotor with the ROSCO controller.

1.7. Model Availability and Its Use

The IEA 15-MW Floating Offshore Wind Turbine model is open-source and available for several analysis tools, such as OpenFAST (Section 2.1.1.1). All the necessary files can be found on GitHub [12].

In this work, the OpenFAST model of the floating turbine has been used. In particular it has been adapted for FAST.Farm (Section 2.1), to reproduce floating wind farms composed by these turbines.

2 Tools

2.1. FAST.Farm

FAST.Farm is a midfidelity nonlinear time-domain multiphysics engineering open-source tool, developed by NREL, for predicting wind turbines power performance and structural loads within a wind farm [13], and it is the main software used to carry out this analysis. FAST.Farm uses OpenFAST (Section 2.1.1.1) [14] to solve the aero-hydro-servo-elastic dynamics of each individual turbine, but additional physics for wind farm-wide ambient wind in the atmospheric boundary layer, such as wake deficits, advection, deflection, meandering, and merging, are accounted. Moreover, a wind farm super-controller, a wind-farm-wide control logic aiming to the overall plant performance improvement, can be adopted. In this work, anyway, it has not been used. FAST.Farm is based on some dynamic wake meandering (DWM) model principles, passive tracer modelling of wake meandering included (Section 2.1.1.2), but it maintains a relatively low computational cost. In the present work, FAST.Farm has been used to simulate the behaviour of the floating wind plant under study.

2.1.1. FAST.Farm Framework and Theory

FAST.Farm is composed of multiple submodels interconnected through a driver code, which drives the overall discrete time-domain solution forward; each of them represents a different physics domain of the wind farm. There are: one module for the Super-Controller (SC), not used in this analysis, one for OpenFAST (OF) (Section 2.1.1.1), one for the Wake Dynamics (WD) (Section 2.1.1.2) and one for the Ambient Wind and Array Effects (AWAE) (Section 2.1.1.3). For OF and WD modules, there is one instance for each wind turbine/rotor. OF, WD and AWAE modules are explained in the next subsections, while The FAST.Farm structure is presented in Figure 2.1. FAST.Farm can be compiled and run in serial or parallel mode. Parallelization is possible through OpenMP, allowing FAST.Farm to take advantage of multicore computers: it divides computational tasks among the cores within a node to speed up the simulations.

All the inputs needed to run FAST.Farm, are read from several text-format input files, containing the proprieties and the data of the wind turbines and of the ambient conditions with unit of measures of the International System of Units (SI system). The

aero-hydro-servo-elastic output variables calculated by FAST.Farm are stored in time-series text-based or binary results files concerning the single turbines and the entire farm. Visualization output files (full 3D low- and high-resolution disturbed wind data output files, ".vtk") are available too.

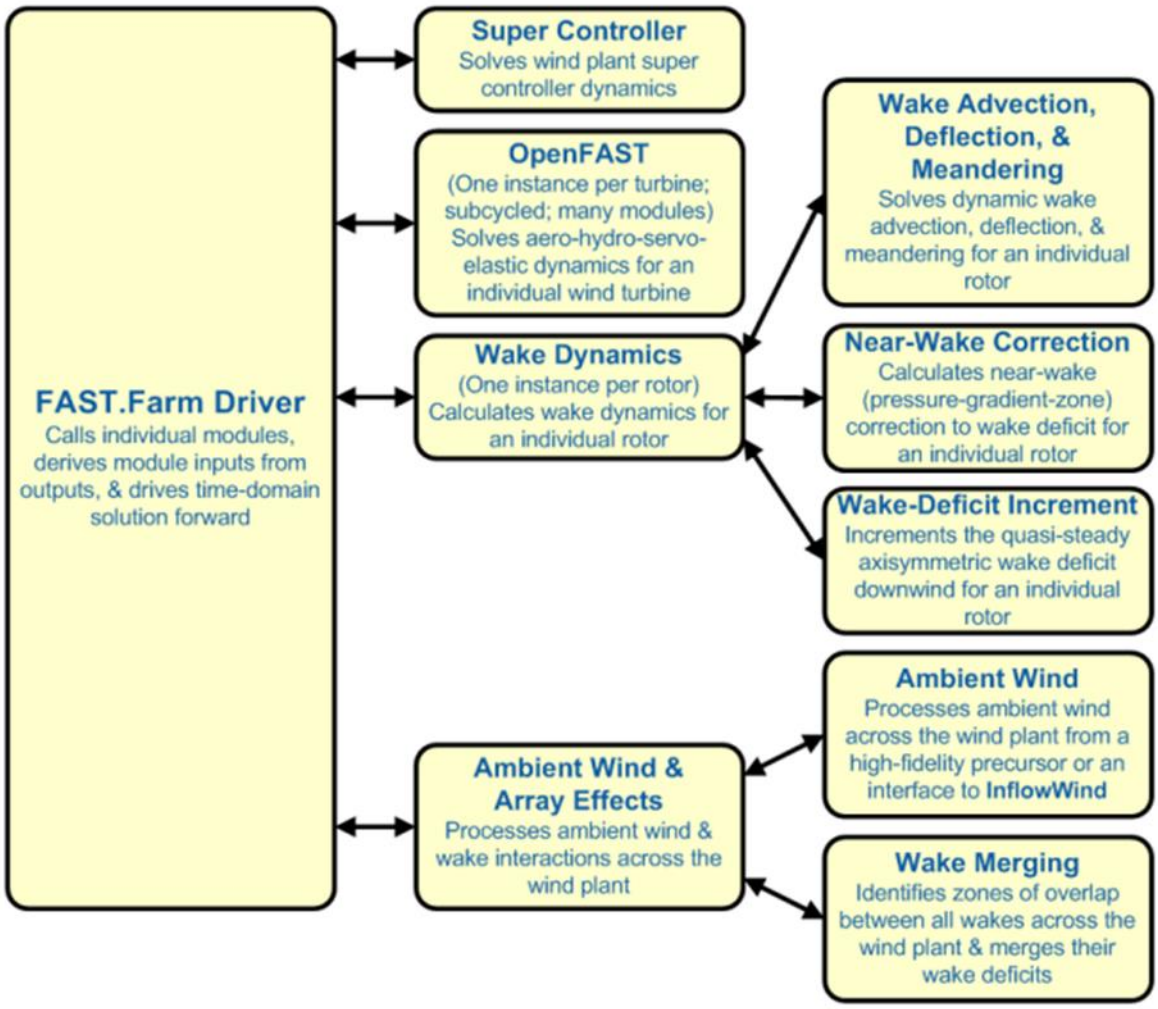

Figure 2.1: FAST.Farm submodels hierarchy.

2.1.1.1. OpenFAST Module

The OF module enables the coupling of OpenFAST tool [14] to FAST.Farm. OpenFAST models the dynamics (loads and motions) of the single turbines in the wind farm, considering the environmental contributions/effects of wind inflow and, for offshore systems, waves, current, and ice and coupled system response of the full system (the rotor, drivetrain, nacelle, tower, controller, and, for offshore systems, the substructure and station-keeping system. OpenFAST is in turn composed by several modules corresponding to different physical domains of the coupled aero-hydro-servo-elastic solution and requiring one or more input files (Figure 2.2).

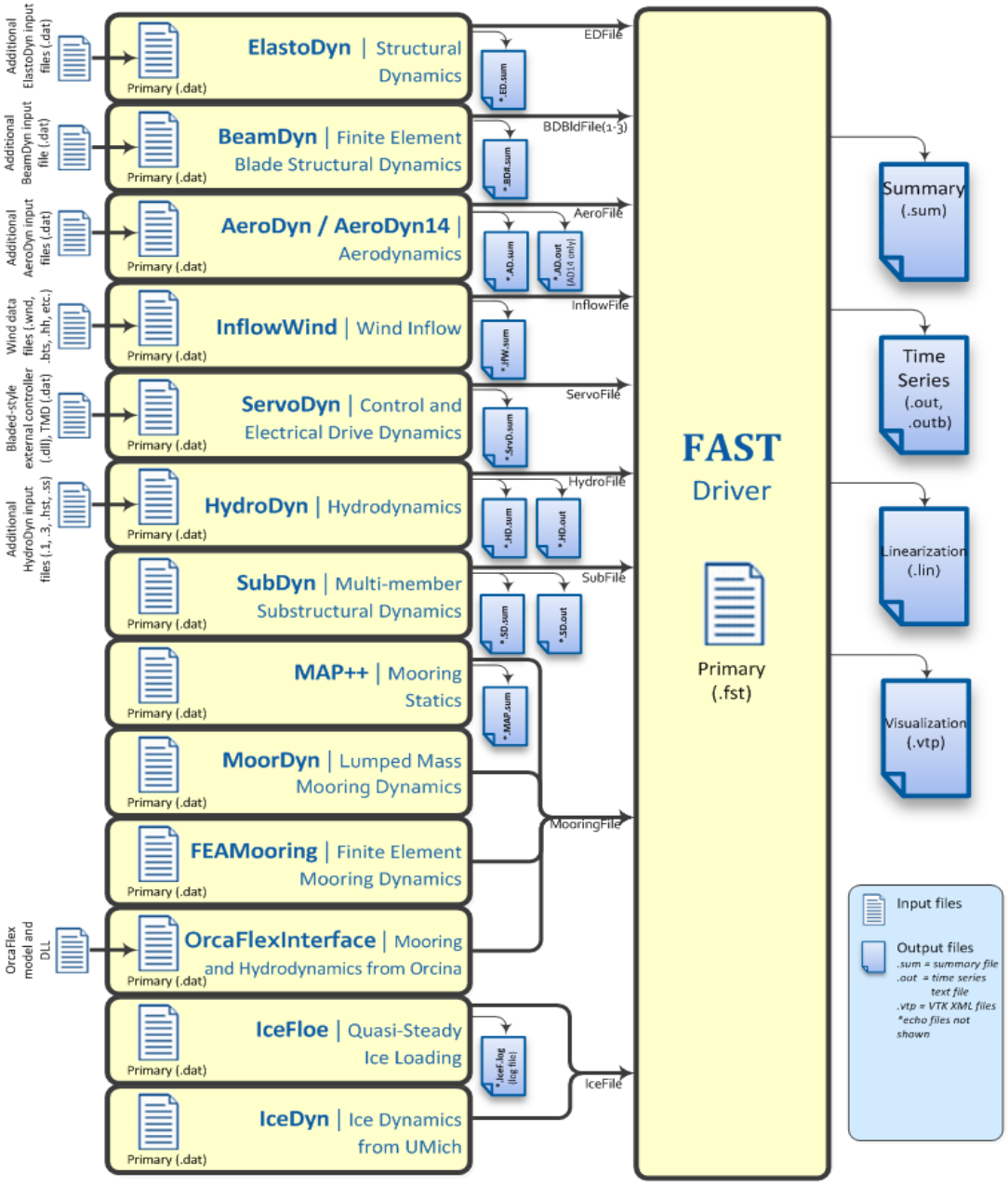

Figure 2.2: OpenFAST scheme.

2.1.1.2. Wake Dynamics Module

The WD module computes wake dynamics for an individual rotor, including wake advection, deflection, and meandering, a near-wake correction and a wake-deficit increment. The near-wake correction accounts for the effect of the pressure-gradient zone in correspondence of the wake on the wake deficit. The wake-deficit increment treats the nominally downwind shift of the quasi-steady-state axisymmetric wake deficit. An axisymmetric finite-difference grid (**Errore. L'origine riferimento non è stata trovata.**) consisting of a fixed number of wake planes, each with a fixed radial grid of *NumRadii* nodes with a radial increment *dr*, is used for the discrete time resolution of the wake-deficit evolution. Each wake plane is a sort of cross section of the wake wherein the wake deficit is calculated. The FAST.Farm wake-dynamics solution is extended with respect to the passive tracer solution for transverse wake meandering (horizontal and vertical fluctuating movement of the wake) [15], in order to account for wake deflection and wake advection.

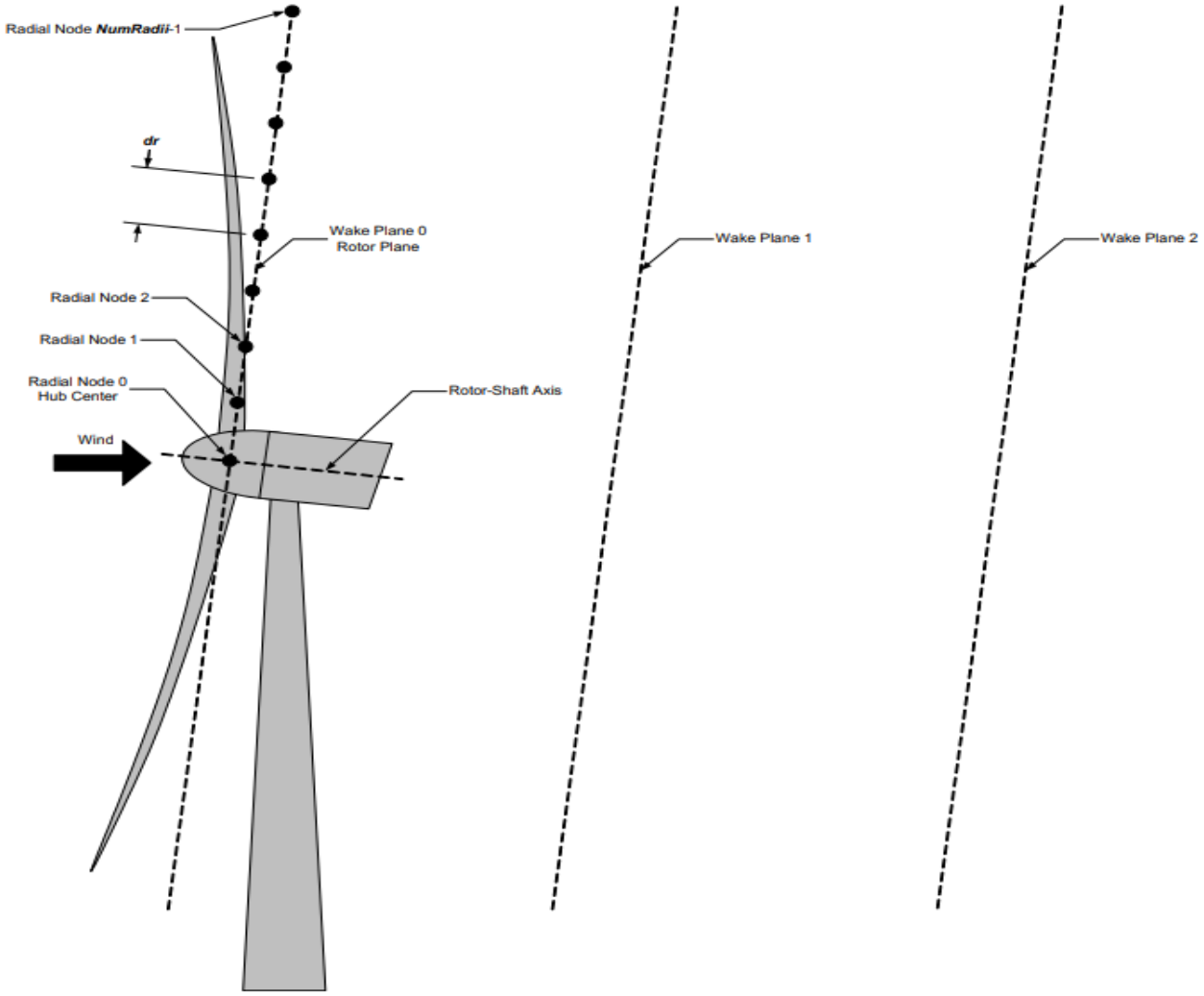

Figure 2.3: Example of radial finite-difference grid. For clarity of the illustration, the number and size of the wake planes are shown smaller than they should be.

The near-wake correction submodel of the WD module computes the wake-velocity deficits at the rotor disk, considers them as boundaries for the wake-deficit evolution. The near-wake correction accounts for the drop-in wind speed and for the wake radial expansion in the pressure-gradient zone behind the rotor. In the far-wake region, further downwind, the wake deficit is approximately Gaussian and recovers to free stream due to the turbulent transfer of momentum into the wake from the ambient wind across the wake shear layer. Wake-deficit evolution consists in this flow-speed reduction and gradual free stream recovery. FAST.Farm WD module models the wake-deficit evolution using the thin shear-layer approximation of the Reynolds-averaged Navier-Stokes equations under quasi-steady-state conditions, with axisymmetric coordinates and an eddy-viscosity formulation for the turbulence closure.

2.1.1.3. Ambient Wind and Array Effects Module

The AWAE module elaborates ambient wind and wake interactions across the wind farm. It includes the ambient wind submodel, which processes ambient wind across the wind farm, and the wake-merging submodel, which identifies overlapping zones between all wakes across the wind farm and merges their wake deficits. Wake volumes are on the base of the AWAE module calculations; they are volumes made by a (possibly curved) cylinder starting at a wake plane and extending to the next adjacent one along the line connecting the two wake planes centres (Figure 2.4). The AWAE module output calculation is the only major calculation that cannot be solved in parallel to OpenFAST.

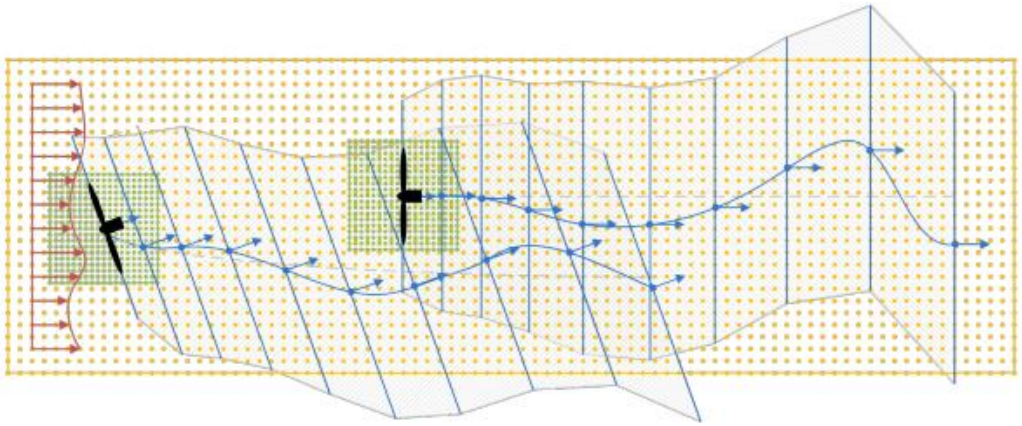

Figure 2.4: Wake planes, wake volumes, and zones of wake overlap for a two-turbine wind farm, with the upwind turbine yawed.

Ambient wind data can be generated with a high-fidelity precursor simulation, or with an interface to the InflowWind module in OpenFAST. The latter is the modality used in the present work and it permits the employment of simple ambient wind: steady

wind, uniform wind (not used in this analysis), discrete wind events (not employed in the present work), or synthetically generated turbulent wind data. If steady wind conditions are enabled, the horizontal wind speed for a reference height has to be set. The wind velocity at different heights is calculated through a power law (Equation 2.1):

$$\boldsymbol{U_h} = U_{ref}\left(\frac{h_h}{h_{ref}}\right)^{\alpha_{PL}} \tag{2.1}$$

Where:

- U_h is the horizontal ambient wind speed at the generic height h_h,
- U_{ref} is the horizontal ambient wind speed at the reference height h_{ref},
- α_{PL} is the power law exponent, which depends on the ambient conditions and on the type of terrain. It has to be defined empirically to have an accurate wind velocity estimation.

The steady undisturbed wind speed distribution remains constant during all the simulation time, changing only with the interaction with obstacles (wind turbines).
Synthetically generated turbulence, instead, can be obtained with TurbSim (Section 2.2.1) or with Mann Turbulence Generator (Section 2.2.2). Both have been used in this work.
The ambient wind data to be used in FAST.Farm, must be available in two different resolutions in both space and time: since AWAE module makes a spatial average across wake planes of the wind, FAST.Farm needs a low-resolution wind domain, encompassing the entire wind farm considering any possible displacement of the turbines, which can be potentially placed everywhere in it; high-resolution wind domains around each wind turbine (capable to contain any turbine movement) is also needed for an accurate loads estimation. The latter domains have a finer resolution, defined by the user, both in space and time, with respect to the low-resolution one, with which overlap in some regions of the space.
These wind data represent the largest memory requirement of FAST.Farm.

The wake-merging submodel of the AWAE module identifies zones of wake overlap between all wakes across the wind farm by finding wake volumes that overlap in space. In these zones, the axial and transverse (radial) wake deficits components are superimposed (wake-merging).

FAST.Farm allows the generation of particular output files to visualize the ambient wind and wake interactions across the wind farm; the Visualization Toolkit (VTK)-formatted output files.

2.2. Synthetic Turbulence Generator

Turbulent ambient wind data to feed FAST.Farm with, can be synthetically generated with external tools. In this work, two different turbulence software have been used for this purpose: TurbSim and Mann Turbulence Generator.

2.2.1. TurbSim

TurbSim [16] is an open-source stochastic turbulence simulator, developed by NREL with the aim to provide a numerical simulation of a turbulent full-field flow for supporting the design of wind turbines. The simulated inflow turbulence environments, in fact, can be used to feed many wind turbines/farms simulation codes and incorporate many of the important fluid dynamic features adversely influencing aeroelastic response and loading of the turbines.

TurbSim simulate randomized coherent turbulent structures; they are characterized by concentrated vorticity, appreciable scale and lifetime and recurrent flow organization, reflecting the spatiotemporal turbulent velocity field relationships seen in instabilities associated with nocturnal boundary layer flows. This vortex coherence is superimposed on a further randomized background turbulent field, generated by one of the diabatic (non-neutral) user-selected spectral models. The randomized scaling of these structures is modelled as a combination of non-homogenous Poisson [17] and Lognormal Stochastic Processes [18].
An input (".inp") file is needed to run the software, in which are defined: the first and second random seeds; the characteristic grid; the length of the generated analysis time series; the time-step; the spectral model (the ones available are specifically described in the TurbSim guide [16]); the meteorological boundary conditions (e.g. mean wind speed, reference height, desired turbulence intensity, the wind profile type and the power law exponent); and the spatial coherence parameters.
The random seeds are used to randomize the phases (one per frequency per grid point per wind component) for the velocity time-series.

For what concern the characteristic grid, it is two-dimensional and its points are the ones in which the wind velocity is calculated. This grid has to be set so that all the farm/turbine result encompassed in lateral (Y) and vertical (Z) direction. There are no specifications in X direction: The grid Y-Z plane, in fact, moves through the turbine along the positive X axis at the mean hub-height wind speed. An example of this "marching" grid can be seen in Figure 2.5, in which also the convection for the coordinates system of reference is defined.

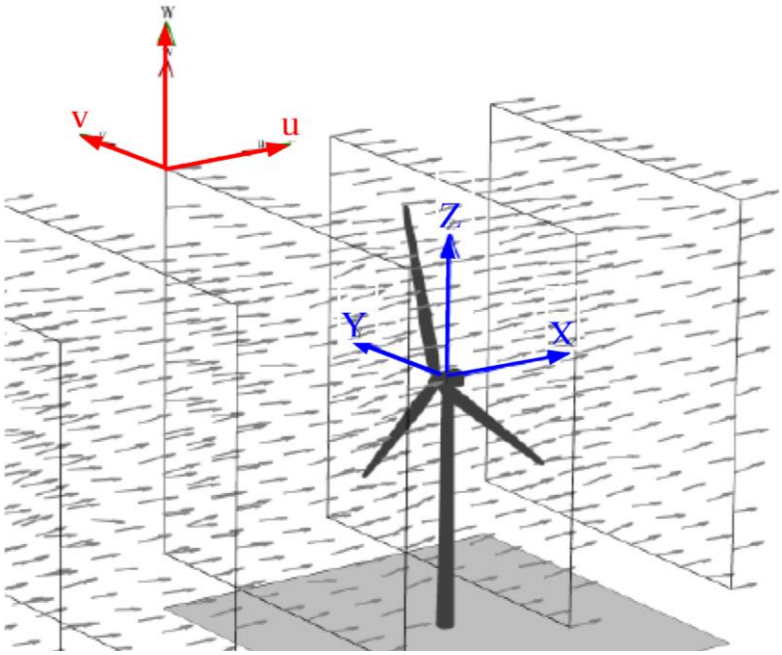

Figure 2.5: Example of TurbSim grid.

TurbSim generates wind velocities transversely throughout the domain using u-, v-, and w-spatial-coherence models based on a selection of coherence model equations and their associated parameters. Considering the coherence components, u is the longitudinal (streamwise) one, v is the tranverse (crosswise) one and w is the vertical one, as depicted in Figure 2.5. Among the available models, the one used in the present analysis is the International Electrotechnical Commission (IEC) spatial-coherence model, in which the spatial coherence is computed using Equation 2.2.

$$\boldsymbol{Coh_{i,j_k}(f)} = \exp\left(-a_k\sqrt{\left(\frac{r_{ijf}}{V_{Advect}}\right)^2 + \left(r_{ij}b_k\right)^2}\right) \tag{2.2}$$

Where:

- V_{Advect} is the hub height average wind speed specified in TurbSim [m/s], which coincides with the advection speed in the OpenFAST InflowWind module of FAST.Farm [13];
- Coh_{i,j_k} is the spatial coherence between points i and j for the velocity components k=u,v,w;
- r_{ij} represents the distance between points i and j;
- f is the cyclic frequency;
- a_k is the coherence decrement parameter [-];
- b_k is the coherence offset parameter [m^{-1}].

The spatial coherent model and the a_k and b_k parameters for each component has to be specified.

In addition, there are several available output file formats, the one used in the this work to feed the OpenFAST Inflow File, is the full-field time-series data in TurbSim/AeroDyn form (".bts").

2.2.2. Mann Turbulence Generator

Mann Turbulence Generator [19] is an open-source software developed by DTU to generate turbulence time-series wind data for each velocity components, u, v and w, following the Mann model. It was born as a pre-processing tool for HAWC2 simulation code [20], but it can be used also for OpenFAST and FAST.Farm.

The Mann turbulence model [21] is a spectral tensor von Kármán based model, combining rapid distortion theory (RDT) and eddy lifetime considerations [22]. From RDT the spectral tensor "stretching" evolution equation, with the tensor becoming more and more "anisotropic" with time, is taken. Moreover, RDT influence the lateral–vertical coherence in the rotor plane [23]. With the assumption of incompressible isotropic turbulence [24], the spectral tensor between two points *i* and *j* can be evaluated as (Equation 2.3):

$$\boldsymbol{\Phi_{i,j}}(\boldsymbol{k}) = \frac{E(k)}{4\pi k^4}\left(\delta_{i,j}k^2 - k_i k_j\right) \qquad (2.3)$$

Where:

- $K = (k_1, k_2, k_3) = \frac{2\pi f}{\bar{U}}$ (2.4)
  is the non-dimensional spatial wavenumber for the three component directions; *f* is the frequency and $\bar{U}$ is the mean wind speed;
- $\delta_{i,j}$ represents the Dirac's delta function;
- $E(k) = \alpha\epsilon^{\frac{2}{3}}L^{\frac{5}{3}}\frac{L^4k^4}{(1+L^2k^2)^{\frac{17}{6}}}$ (2.5)
  is the energy spectrum (von Kàrmàn formulation [25]) with:
- $\alpha\epsilon^{2/3}$, representing the Kolmogorov constant multiplied with the specific turbulent kinetic energy viscous dissipation raised to the power of two-thirds;
- *L* representing the length scale;
- Γ representing the eddies lifetime-related non-dimensional parameter.

The parameters which the user has to specify in the Mann Turbulence Generator input file (".bat") are $\alpha\epsilon^{2/3}$, *L*, Γ , the casual seed and the geometrical parameters for the 3-D discretization grid definition. The latter must encompass all the farm. Moreover, the number of grid points (nx, ny and nz) and the grid extensions in x, y and z direction must be a power of 2 for a software constraint. The coordinate reference system in the

same of the FAST.Farm one, except for the x-axis positive verse convention, which is opposite.

From the spectral tensor components the turbulent velocity field components can be found using an approximation by discrete Fourier transform [23]. They can be found in IEC standard 2019-Annex C [26];

With respect to the Kaimal spectrum and the other exponential coherence model, the Mann turbulence model provides a 3-D spectral tensor including u-, v- and w-components correlation. This correlation is not present, instead, in the Kaimal model and it makes the Mann model better for lidar measurements analyses [22].

Mann Turbulence Generator output one binary file (".bin") for each wind component, which can be used to feed FAST.Farm by recalling them in the "OpenFAST InflowWind file.

2.3. MLife

MLife is an open-source NREL tool, working in MATLAB environment, developed for the wind turbine tests, and aero-elastic, dynamic simulations results post-processing [27]. MLife's aims consist to compute statistics and to estimate fatigue, in accordance with IEC 61400-1 edition 3 Annex G [28], for one or more time-series. The fatigue calculations include:

- short-term damage-equivalent loads (DELs) and damage rates: they are based on single time-series;
- lifetime DEL results: they the entire set of time-series data;
- accumulated lifetime damage;
- time until failure.

In the present analysis just short-term DELs have been calculated. A DEL is a constant-amplitude fatigue-load occurring at a fixed load-mean and frequency and producing the equivalent damage as the variable spectrum loads which takes place during a fatigue solicitation. In Section 2.3.1, the modalities for their calculation are explained [27]. The other available fatigue calculations, not performed in this work, can be found in the MLife Theory Manual [27].

The program inputs are a text file with settings (".mlif"), and one or more loads or stresses time-series data files or matlab structs. The outputs, instead, can be MATLAB variables, text or binary output files (".out" or ".outb", respectively), and/or Excel formatted files.

2.3.1. Short-Term DELs Calculation

Fatigue damage are damages due to fluctuating loads over a period of the design life (for short-term fatigue) or the entire design life (for lifetime fatigue) of the subject, which is a wind turbine for MLife. Individual hysteresis cycles, characterized by a load-mean and range, are obtained from the breaking down of these fluctuating loads and by matching local minima with local maxima in the time-series, like rainflow counting. MLife uses Miner's Rule (Palmgren, 1924; Miner, 1945) to linearly accumulate damages with each of these cycles. The short-term accumulated damage D_j^{ST} from time-series j is calculated as follows:

$$\boldsymbol{D_j^{ST}} = \sum_i \frac{n_{ji}}{N_{ji}} \qquad (2.6)$$

Where:

- n_{ji} is the extrapolated cycle count for the i[th] cycle and j[th] time-series. It is extrapolated differently depending on the design load case (DLC) classification of the time-series data (Power Production, Parked, Discrete Events). The extrapolation of the damage-cycle counts rely on the wind turbine location wind speed. MLife, among the inputs, need the hub wind velocity time-series and models the wind with a binned Weibull distribution;
- N_{ji} is the cycles to failure and it is calculated as

$$\boldsymbol{N_{ji}} = \left(\frac{L^{ult} - |L^{MF}|}{\left(\frac{1}{2} L_{ji}^{RF}\right)} \right)^m ; \qquad (2.7)$$

- L^{ult} is the ultimate design load of the component, specified by the user;
- L^{MF} is the fixed load-mean;
- m is the Whöler exponent, specified by the user;
- L_{ji}^{RF} is the load range of the cycle about a fixed load-mean value.

The latter expression is valid under the hypothesis that the fatigue cycles occur over a fixed load-mean, whereas the actual occurrence is over a load means spectrum. A correction, the Goodman correction, concerning this issue can be used, if enabled by the user, within MLife. Anyway, it has not been used in the present work.

From short-term accumulated damage, MLife estimates a short-term DEL for each input time-series, as shown in the following procedure:

$$\boldsymbol{D_j^{ST}} = \sum_i \frac{n_{ji}}{N_{ji}} = \frac{n_j^{STeq}}{N_j^{eq}} \qquad (2.8)$$

- n_j^{STeq} is the total equivalent fatigue counts for time-series j, calculated as a product of the DEL frequency, f^{eq}, and the elapsed time of time-series j, T_j,

$$\boldsymbol{n_j^{STeq}} = f^{eq}\, T_j ; \qquad (2.9)$$

- N_j^{eq} represents the j[th] time-series equivalent number of cycles until failure and it is calculaded as

$$\boldsymbol{N_j^{eq}} = \left(\frac{L^{ult} - |L^{MF}|}{\left(\frac{1}{2}DEL_j^{STF}\right)}\right)^m \quad (2.10)$$

The short-term DEL for time-series j about a fixed mean, DEL_j^{STF}, is found by rearranging Equation 2.7:

$$\boldsymbol{DEL_j^{STF}} = \left(\frac{\sum_i (n_{ji}\left(L_{ji}^{RF}\right)^m)}{n_j^{STeq}}\right)^{\frac{1}{m}} \quad (2.11)$$

3 Wake Analysis of a Two Turbines Configuration

The starting point of this work has been the analysis of the effects of the wakes on the response of a two IEA 15-MW Floating Offshore Wind Turbines configuration. A procedure similar to the one used by A. Wise and E. E. Bachynski in their study "Analysis of wake effects on global responses for a floating two-turbine case" [29] has been followed. The aim was that of reproduce this method with slightly differences (explained later in Section 3.1) on IEA 15-MW Floating Offshore Wind Turbines, and then use it on a more complex geometry (see Chapter 4), using the results of the two-turbines analysis as a benchmark.

The response of the turbines has been investigated in terms of flow field, wake meandering, hubs wind velocity and turbulence intensity, platform motions, axial stresses and short terms fatigue damages on the tower and on the mooring system.

3.1. Methodology

The methodology of the A. Wise and E. E. Bachynski study "Analysis of wake effects on global responses for a floating two-turbine case" [29] has been reproduced but the involved turbine model is different: in the reference paper, DTU 10 MW reference turbines [30], each supported by a CSC semi-submersible platform [31], are used, while, in the present analysis, IEA Wind 15-Megawatt Offshore Reference Wind Turbines with UMaine VolturnUS-S Reference Platforms (See Chapter 1).

Moreover, the calculation of the fatigue damages conducted is different from the one of the paper, as explained later (Section 3.1.6).

3.1.1. Geometrical Layout and Resolution

As in the reference paper, the two IEA 15-MW Floating Offshore Wind Turbines have been placed aligned in the principal direction of the undisturbed wind flow (x), at a distance of 8 diameters (8D) from each other.

The FAST.Farm low-resolution domain (Section 2.1.1.3) has been set so that to have the same spatial and temporal discretization of the Wise and Bachynski study [29] and to encompass all the turbines considering any possible displacement:

- Origin in x, y and z direction: 0 m, -150 m, 10 m. The origin in z has not been placed to 0 (SWL) because FAST.Farm low-resolution domain in z need to encompass all the tower, which starts at around 15m over SWL (Figure 1.3), but not necessarily the platform and in order to better match the TurbSim grid (see Section 2.2.1);
- Spatial steps Δx, Δy and Δz: 25 m, 10 m, 10 m (as in the paper);
- Number of points in x, y and z: 200, 31, 28;
- Resulting grid dimensions (length, width, height): 4975 m, 300 m, 270 m.
- Time step: 2 s (as in the paper).

The turbines have been placed, in x, y and z respectively:

- Upwind turbine: 500 m, 0 m, 0 m
- Downwind turbine: 2435.52 m, 0 m, 0 m. It is 8D far from the upwind turbine in x direction, since the diameter D is equal to 241.94 m.

The hub of both the rotors is at a height of 148.35 m.

The FAST.Farm high-resolution domains (Section 2.1.1.3), one for each turbines, have the same dimensions and discretization among them and they are more defined both in terms of space and time with respect to the low-resolution one. They starts 100 m before the turbine in x direction, turbines are placed exactly in the centre of the own high-domain in y direction and the origin in z has been set to 10 m as the low-resolution domain. The spatial discretization is the same of the paper (Δx=10 m, Δy=5 m and Δz= 5 m) and the number of points in x, y and z directions is 25, 57 and 55 respectively, resulting in a length, width and height of 240 m, 280 m, 270 m. In this way, each high-resolution domain encompass its turbine and any possible displacement. The time step for the high-resolution domains has been configured to 0.5 s; the temporal resolution is slightly worse than the one of the reference paper (around 0.33 s).

Either the low- and the high-resolution domains extend symmetrically in y direction toward both negative and positive values and the turbine is in the centre. In x direction, instead, the part behind the turbine is bigger than the part ahead in order to better study and visualize the wakes.

The present two turbines configuration is visualized in the low-resolution domain in Figure 3.1, while the grids of the low- and high-resolution domains are shown together in Figure 3.2.

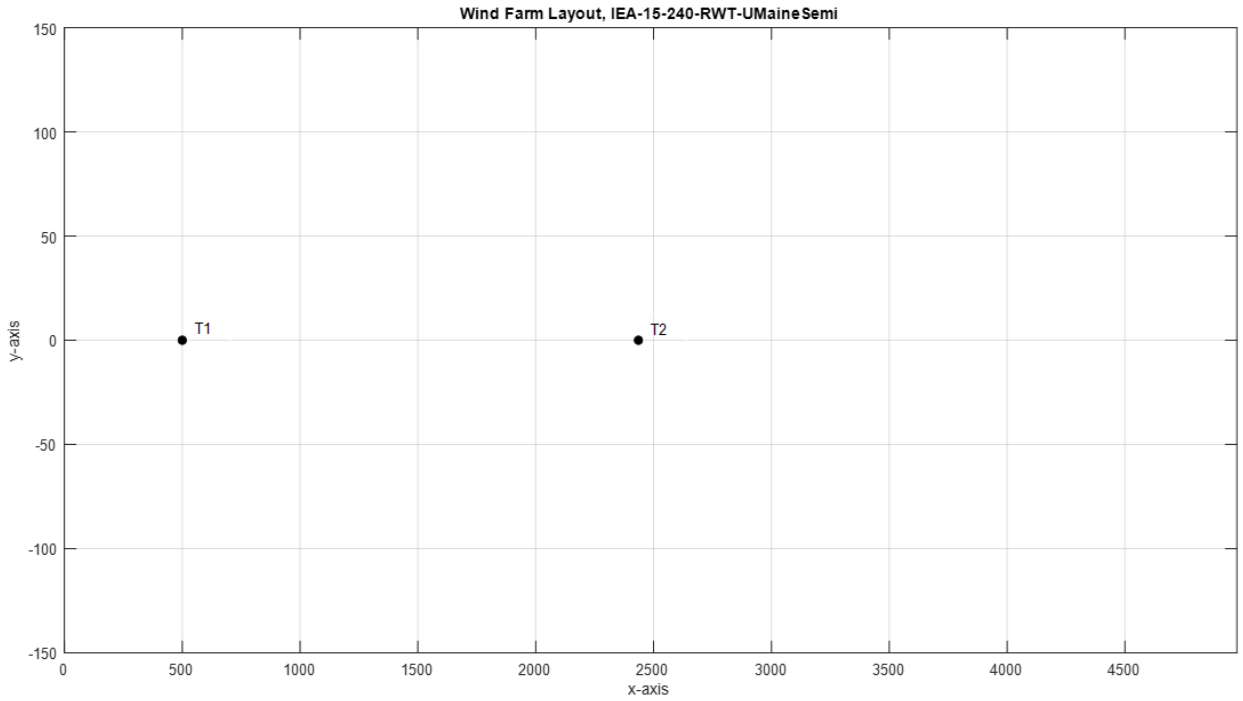

Figure 3.1: Two IEA 15-MW Floating Offshore Wind Turbines configuration visualized in the FAST.Farm low-resolution domain.

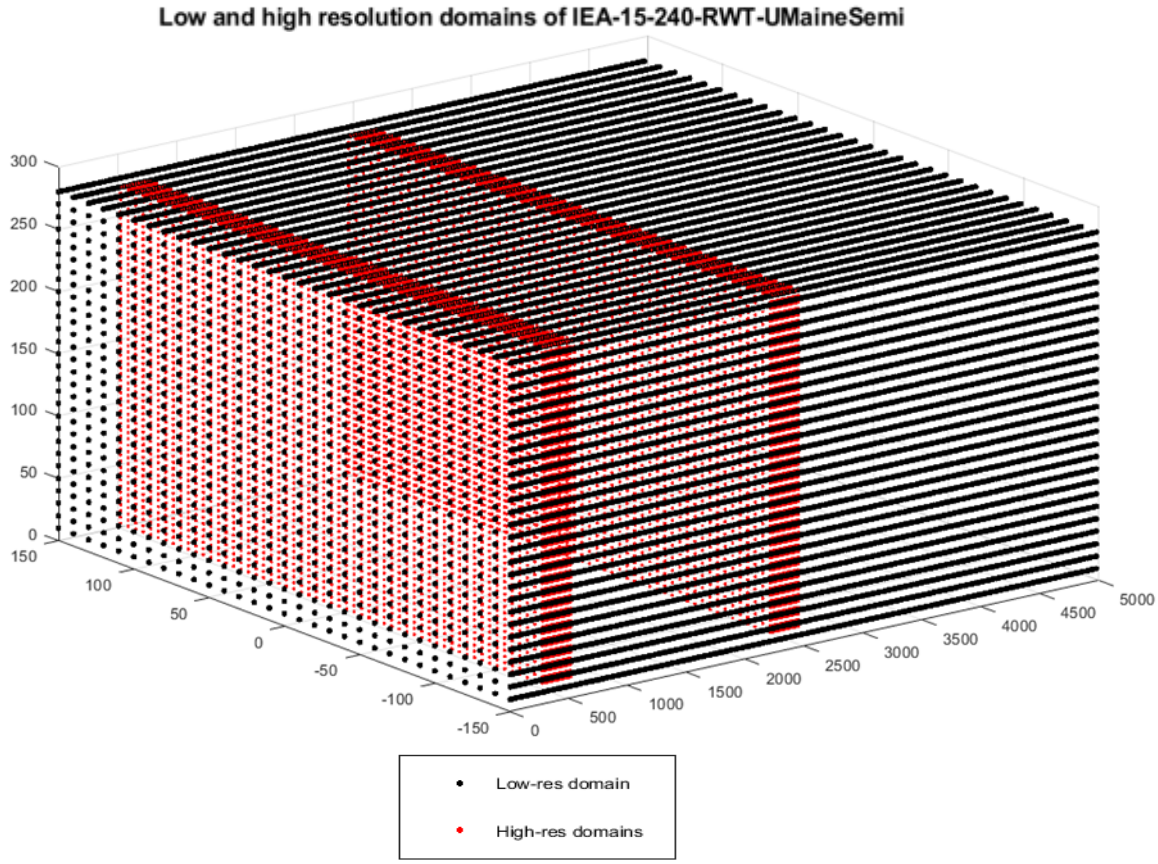

Figure 3.2: FAST.Farm low- and high-resolution domains grid of the two IEA 15-MW Floating Offshore Wind Turbines configuration.

For what concerns the wake radial finite-difference grid (Section 2.1.1.2), 140 wake planes, each with 52 radial nodes radially distanced 6 m among them have been set.

3.1.2. Environmental Conditions

The ambient conditions of the reference paper [29] has been reproduced in order to eliminate the influence of the environmental differences on the turbines response. The reference location was a Norwegian site in the North Sea, depicted as Site 14 in the Figure 3.3 [32]. Its environmental conditions data, used in the reference paper as well as in this analysis, have been derived from Lin Li, Zhen Gao and Torgeir Moan's study [32] and they are listed below.

- Water depth: 200 m;
- Main inflow wind direction: x;
- Hub-height reference wind speed: 10 m/s (slightly below the nominal one for the present turbine, i.e. 10.59 m/s (Section 1.6));
- Shear exponent: 0.055 (α_{PL} in Equation 2.1, Section 2.1.1.3)
- Wave spectrum in accordance with the IEC 61400-3 standard [33];
- Wave height: 2.5 m;
- Wave peak period: 9.5 s;

Figure 3.3: Reference location among other potential European offshore sites.

3.1.3. Pre-simulation Identification

When a FAST.Farm simulation is launched, the first parameters values of the time-series, which are obtained, are distorted. The simulation is, in fact, characterized by a transient in the first time steps: the pre-simulation. After the identification of its duration, pre-simulation has to be removed, when data are post-processed.

To identify it, a specific simulation of the model with steady wind conditions (Section 2.1.1.3) at the hub-height velocity of the analysis (10 m/s) and with parked turbines, has been carried on. Turbines have been stopped through the application of the HSS brake. To find out the transient, the trend of the disturbed horizontal wind velocity in the last point in x-direction of the low-resolution domain at the same z and y of the turbines hub has been analysed. To better figure out where the wind velocity has been evaluated in the low-resolution domain, Figure 3.4 has been inserted.

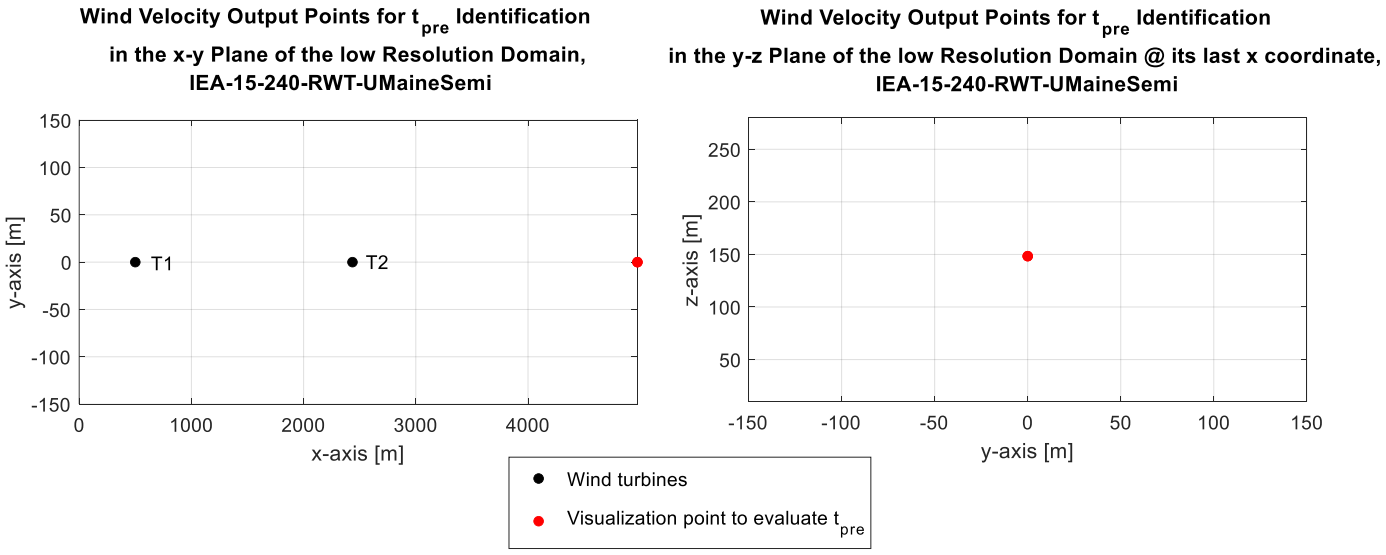

Figure 3.4: Disturbed horizontal wind velocity output point to evaluate the pre-simulation duration, visualized in the x-y (left) and y-z (right) planes of the low-resolution domain.

In Figure 3.5 the trend of the disturbed horizontal wind velocity in the aforementioned point is depicted. The instant of end of the transient (t_{pre}) has been identified as 1450 s, keeping a security margin in excess, to account for differences in unsteady conditions and rotating blades. It is highlighted with a vertical red line in the figure. The time-history of all the FAST.Farm output parameters before t_{pre} have been deleted in the data post-processing.

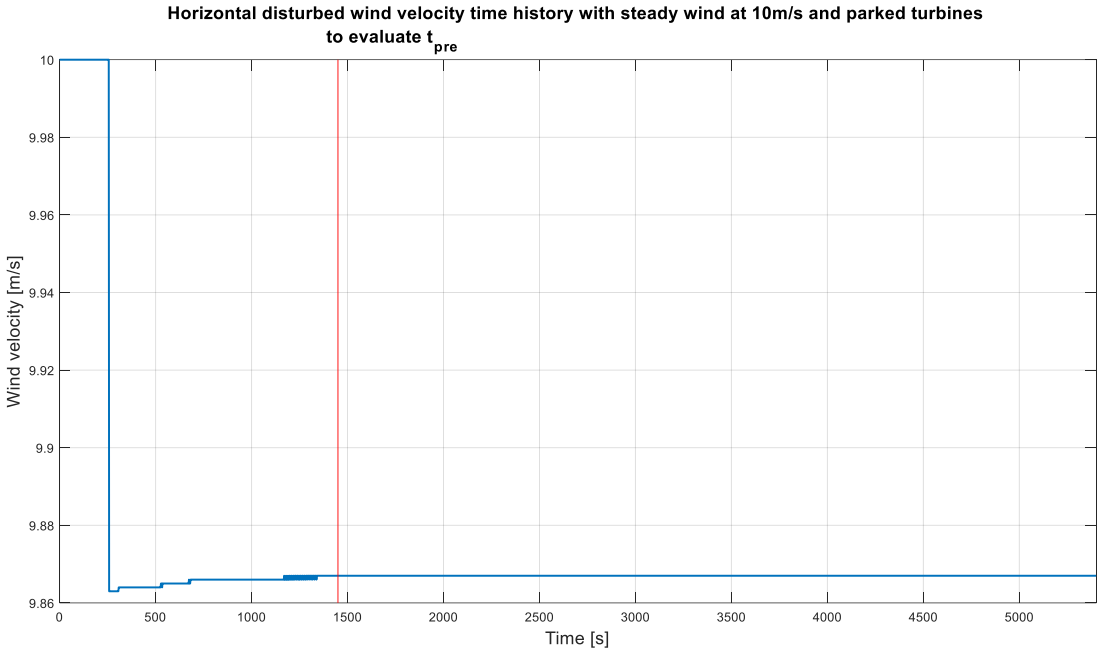

Figure 3.5: Horizontal disturbed wind velocity trend with steady wind condition at 10 m/s and parked turbines in the low-resolution domain point to evaluate t_{pre}.

3.1.4. Simulations

Different full-field turbulent inflow wind data time-series have been used as input in the InflowWind file of FAST.Farm (Section 2.1.1.3) and for each of them a FAST.Farm simulation of the model of 1 h (3600 s), pre-simulation excluded, as recommended by IEC standard [33], have been performed.

In particular, three turbulence models have been analysed and for each of them, in order to take into account the long natural periods and the stochastic variations impact, six inflow time-series have been generated by varying just the casual seed (Section 2.2.1 and 2.2.2), resulting in eighteen different inflow time-series in total and so in eighteen FAST.Farm simulations.

The considered turbulence models have been the same of the reference paper [29]:

- Kaimal Model with u, v and w spatial coherence component (*Kaimal-Coh u, v, w*): this type of turbulence has been simulated with Turbsim (Section 2.2.1). A Turbsim grid 300 m (from -150 m to +150 m) wide (y direction) and 280 m high (z direction) of 28x28 points, encompassing all the low-resolution domain in y and z direction, has been set. Spatial coherence have components in all the three wind directions and the parameters values for a_u, b_u, a_v, b_v, a_w and b_w have been set to 10; 0 m^{-1}; 7.5, 0 m^{-1}; 7.5 and 0 m^{-1}, respectively. In this way a realistic wake meandering behaviour have been induced.

- Kaimal Model with just u spatial coherence component (*Kaimal-Coh u*): this turbulent case have been reproduced with Turbsim too, using an analogue Turbsim grid. Spatial coherence have been considered just with u component and to the related parameters a_u, b_u, a_v, b_v, a_w and b_w have been assigned values respectively of 12; 3.5273×10^{-4} m^{-1}; ∞; 0 m^{-}; ∞ and 0 m^{-1}. This model permits to isolate the wake meandering effects on the farm's response.
- Mann Model (*Mann*): the wind inflow time series of this model have been generated with Mann Turbulence Generator (Section 2.2.2). A 3-D (x, y and z) grid of 256x64x64 points and 32 m, 16 m and 8 m of x, y and z spatial steps, respectively, encompassing all the low-resolution domain, has been set. For what concern the parameters, a value of 0.10 $m^{4/3}$ has been assigned to $\alpha\epsilon^{2/3}$, 33.6 m to L and 3.9 to Γ. In this way, the Mann model results fit to the Kaimal spectrum, in accordance with the IEC standard.

3.1.5. Axial Stresses Calculation

Axial stresses σ have been calculated at the tower base and top in the downstream point on the external shell, which is the most critical point of the tower cross section [29] [34]. The calculation has been performed using the time-history of the axial force N_z and of the bending moments M_x (roll or side-to-side moment) and M_y (pitch or fore-aft moment) at the lower and higher section of the tower respectively, through Equation 3.1 [29].

$$\sigma(r,\theta) = \frac{N_z}{A} - \frac{M_x}{I_x} r\cos(\theta) + \frac{M_y}{I_y} r\cos(\theta) \qquad (3.1)$$

Where:

r is the radial coordinate of the tower. The external radius r_e is considered, which is

5 m at the tower base and 3.25 m at he tower top (Section 1.3) (Figure 3.6);

θ is the angular coordinate of the tower cross-sectional area (Figure 3.6). A θ of 180° has been considered in order to calculate the stresses on the downstream point of the section.

A is the cross sectional area and, for a circular crown, as in this case, it is calculated as:

$$A = \pi(r_e^2 - r_i^2) \qquad (3.2)$$

With an external radius r_e, assuming the values indicated above, and the internal one r_i of 4.92 m at the tower base and 3.23 m at the tower top (Section 1.3) (Figure 3.6);

I_x and I_y are the second moments of area, which, for the circular crown, are calculated as:

$$I_x = \frac{\pi}{4}(r_e^4 - r_i^4) = I_y \quad (3.3)$$

The bending moments M_x and M_y refer to the FAST.farm tower coordinate system, depicted in Figure 3.7 [13], for what concern the tower base, and to the FAST.Farm base-plate coordinate systemshown in Figure 3.8 [13], for the tower top.

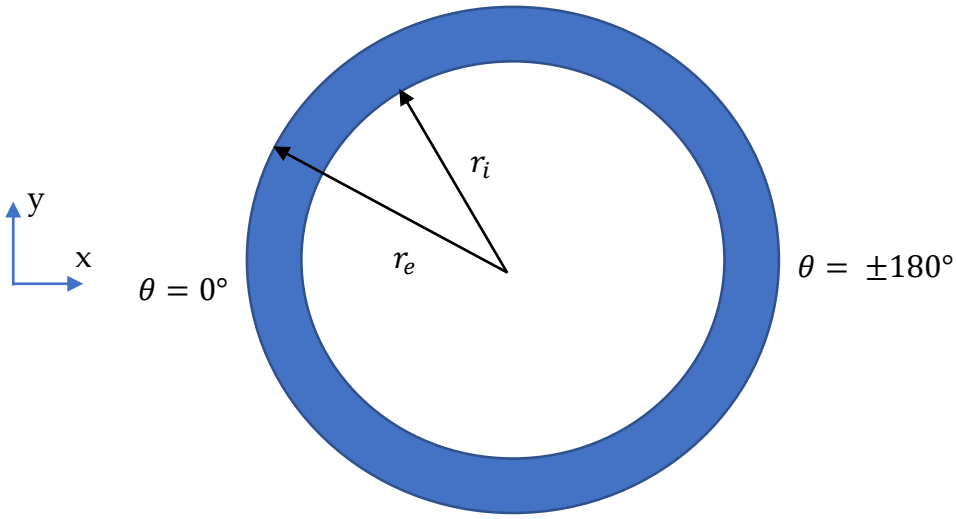

Figure 3.6: Example of circular crown cross sectional area of the wind turbine tower.

Figure 3.7: Tower top coordinates reference system. It is fixed to the support platform, so it rotates and translates with the platform. X_t points the nominal downwind direction.

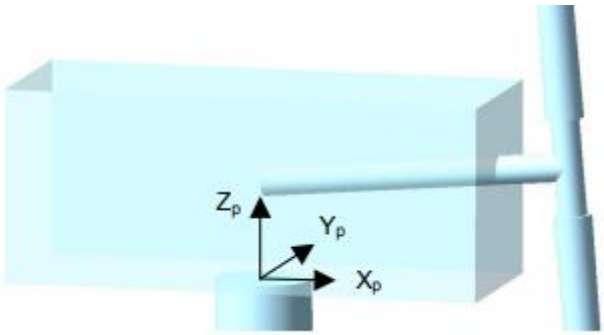

Figure 3.8: Base-plate coordinates reference system. It is fixed to the tower top and so it rotates and translates with the platform, not with the nacelle. When there is not tower deflection, X_p is aligned with X_t.

Axial stresses have been also calculated at the fairlead of the three mooring lines (Figure 1.5) through Equation 3.1 with zero bending moments and considering the fairlead tension as N_z (positive if pointing toward the fairlead) and the cross-section midpoint closest to the fairlead.
In this case, as cross-sectional area A, the circular section of the mooring lines' chain has been considered, which has been calculated as:

$$A = \pi \left(\frac{D_{nc}}{2}\right)^2 \qquad (3.4)$$

Where D_{nc} is the nominal chain diameter of the mooring lines and it is worth 0.185 m (Section 1.5).

For what concerns the shear stresses, instead, they have been not investigated, since they leads to significantly smaller fatigue damages [29].

3.1.6. Fatigue Damages Evaluation

The 1-h short term DELs have been evaluated for the axial force (N_z) and for the total moment M_{tot}, calculated as the vector sum of M_x and M_y, at both tower base and top and for the fairlead tension of the three mooring lines. The calculation have been performed through MLife [Section 2.3], by feeding the software with the time-series of the aforementioned loads.

This one of the main difference with respect the reference paper [29]. In the latter, in fact, the fatigue damages are calculated in terms of equivalent stresses and not loads, using a rainflow cycle counter, the Palmgren-Miners (Palmgren, 1924; Miner, 1945) rule and a low-pass filter.

The fatigue damages have been, instead, calculated in the present work in terms of loads, because this is the most used method in literature to evaluate fatigue by post-processing the FAST.Farm output data.

3.2. Results

3.2.1. Flow Visualization and Wakes Centre

Figure 3.9 represents an instantaneous colormap to visualize the horizontal wind velocity in the x-y plane of the low-resolution domain at the hub height, for the last instant of the first simulation of the *Kaimal-Coh u,v,w*, *Kaimal-Coh u* and *Mann* method, respectively. Figure 3.10, instead, depicts the instantaneous wake centre positions, outputted by FAST.Farm, in the x-y plane of the low-resolution domain normalized on the turbines' diameter at the hub height, for the last instant of the first simulation of each of the three turbulence cases.

Considering the two Kaimal models and looking at these two figures it is clear the effect of the lateral and vertical coherence components on the pattern of the wake. The wake in the *Kaimal-Coh u,v,w* case, in fact, is more irregular while in the case with just u coherence component is more composed and with less meandering. Since the wake meandering is a large-scale turbulence driven phenomenon, v and w components affect it significantly, even if they are smaller with respect to the horizontal wind velocity. For what concern the Mann model, the influence of all the three component is clear and it can be seen from Figure 3.9 that its coherent structures are more stretched with respect to the Kaimal cases. This is a characteristic of the Mann model [35] and influence a lot the turbine response as shown in the other results presented further on.

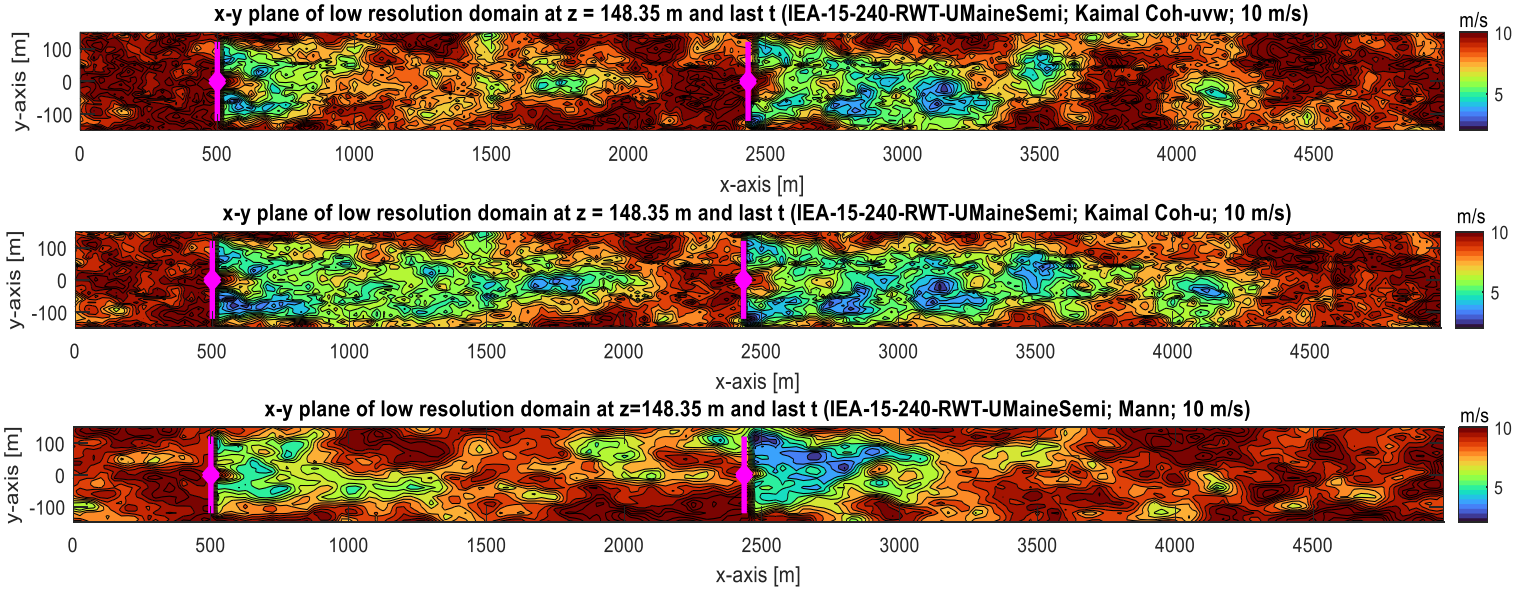

Figure 3.9: Instantaneous (last simulation instant) horizontal wind speed colormap for the first simulation of the *Kaimal-Coh u,v,w* , *Kaimal-Coh u* and *Mann* turbulence case in the low-resolution domain of the two IEA 15-MW Floating Offshore Wind Turbines configuration. Rotors are represented in magenta.

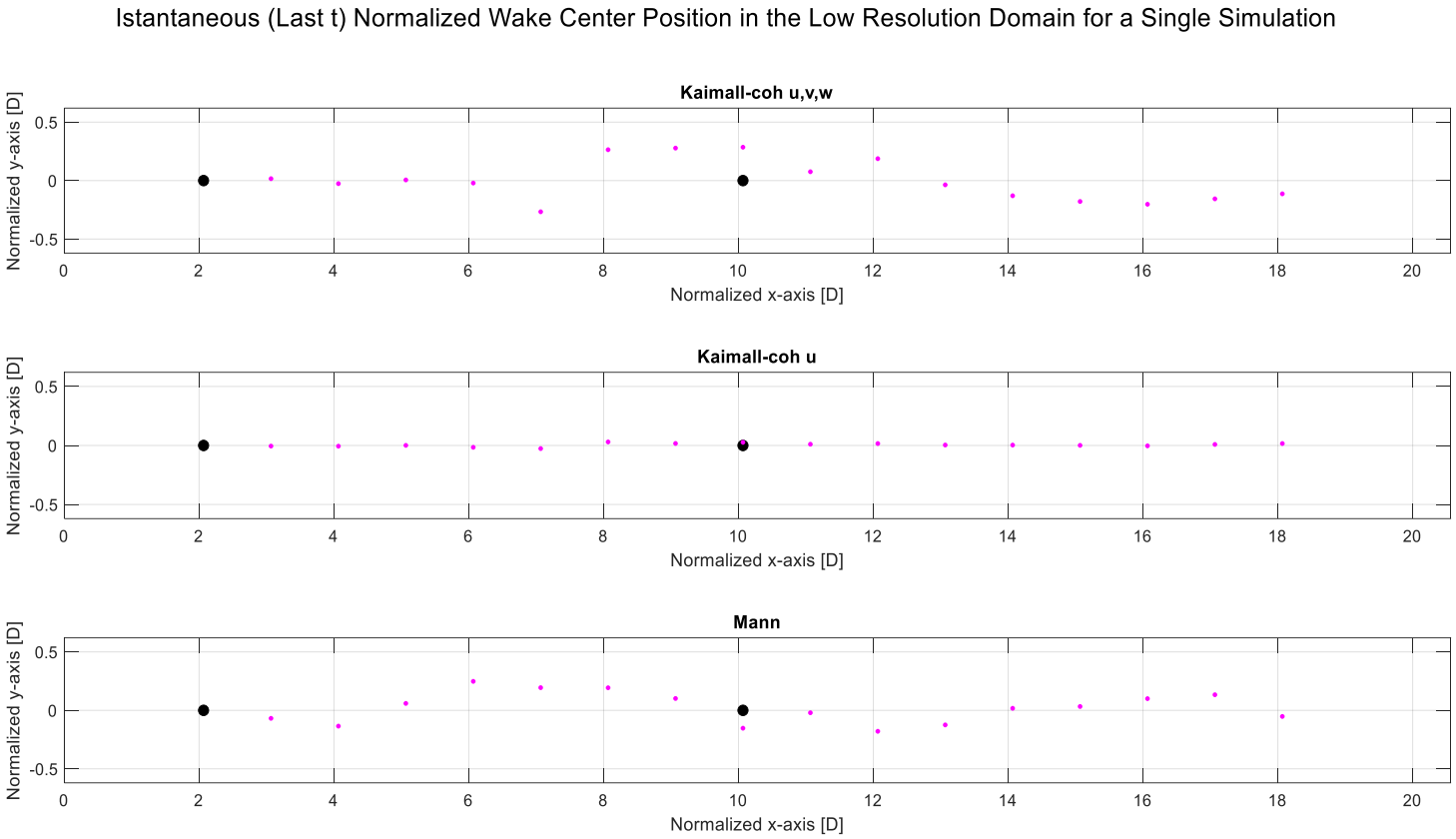

Figure 3.10: Instantaneous (last simulation instant) wake center position for the first simulation of the *Kaimal-Coh u,v,w* , *Kaimal-Coh u* and *Mann* turbulence case in the normalized low-resolution domain of the two IEA 15-MW Floating Offshore Wind Turbines configuration. Rotors are represented in black.

Figure 3.9 and Figure 3.10 shown the flow in just one instant, but the conclusions are valid also considering all the simulation, as confirmed by Figure 3.11.

It shows, in fact, the time-series for the first simulation and the probability density function and the power spectral density averaged over six simulation, of the wake centre lateral position at 8D in x direction from the turbine's hub, for each of the three turbulence models and for each wind turbine. The models which have all the three coherence components (*Mann and Kaimal-Coh u,v,w*) show a remarkable lateral meandering in both the turbines'wake; it is clear by looking at the time-series plots. The 8D y-meandering variance, anyway, is higher for the *Kaimal - Coh u, v, w* case, for both the rotors (around 0.25 D^2 for both) than for the *Mann* one (about 0.08 D^2 for both the turbines), as visible from the PDFs. For what concern *Kaimal - Coh u* simulations, the meandering in y direction is really limited. By watching at the power spectral density graphs, Kaimal - Coh u, v, w and Mann result in a 8D lateral wake meandering

in a frequency range of 0-0.02 Hz for both the turbines and the first (of this two) method is characterized by the lowest frequency behaviour.

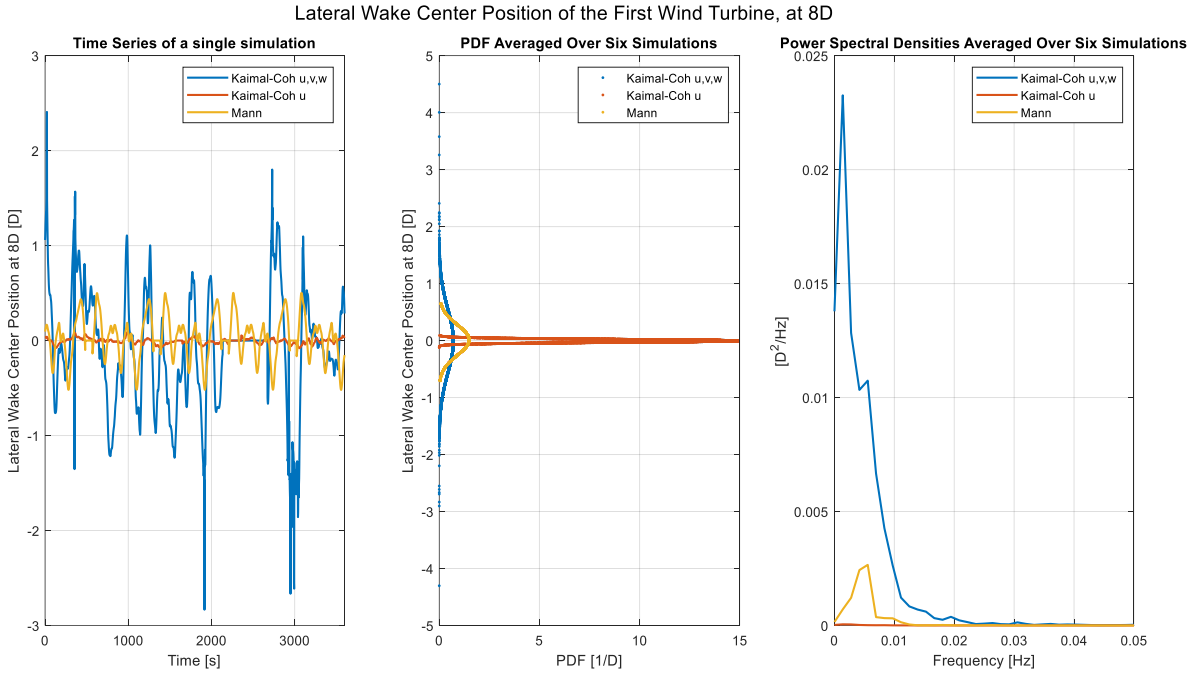

(a) First wind turbine.

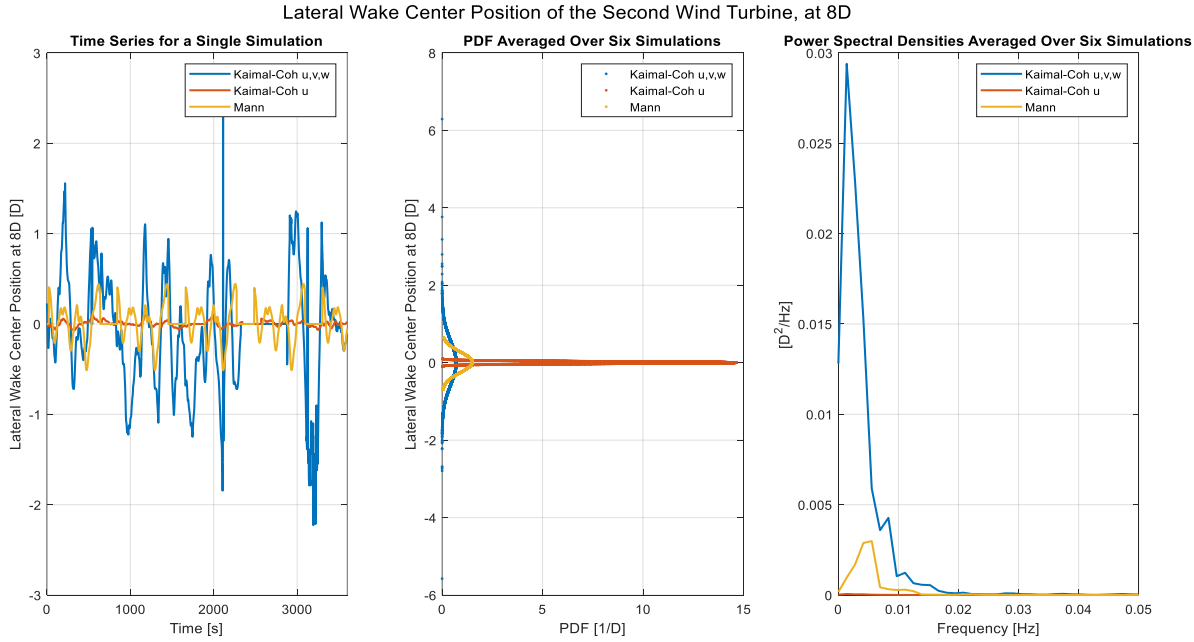

(b) Second wind turbine.

Figure 3.11: 8D lateral wake center position, normalized over the diameter, time-series for the first simulation (left), probability density function (centre) and power spectral densities (right) averaged over six simulations for each turbulence model, for the first (a) and second (b) wind turbine.

3.2.2. Wind Velocity and Turbulence Intensity at the Hubs

Mean horizontal wind velocity and turbulence intensity values at the hub of the two turbines are shown in Figure 3.12 and Figure 3.13, respectively. For each turbulence model, the downwind turbine experiences a decrease of the wind speed and an increase of the TI and so, a reduction of the performance. The greatest wind velocity and TI variations happen in the *Kaimal-Coh u* case: this is due to the fact that this model is the one characterized by the lower lateral meandering (Section 3.2.1) and so the downwind rotor is always in a waked condition. In the *Kaimal-Coh u,v,w* and *Mann* cases, instead, in some instants the wake generated by the upwind turbine avoids the second rotor thanks to the meandering, as shown for example in Figure 3.10. This is an evidence that the main wake characteristic influencing the hub-height wind velocity "felt" by the rotor is the wake-deficit (Section 2.1.1.2).

For what concern the mean hub wind speed, the first undergo a velocity almost equal to the reference one (10 m/s) for each inflow type, while for the second one, it is about 8.82%, 13.87% and 11.88% lower, for the *Kaimal-Coh u,v,w*, *Kaimal-Coh u* and *Mann*, respectively.

Considering the TI, the 6-simulations averaged values are included between 14% and 15% for T1 and between almost 18% and 19% for T2.

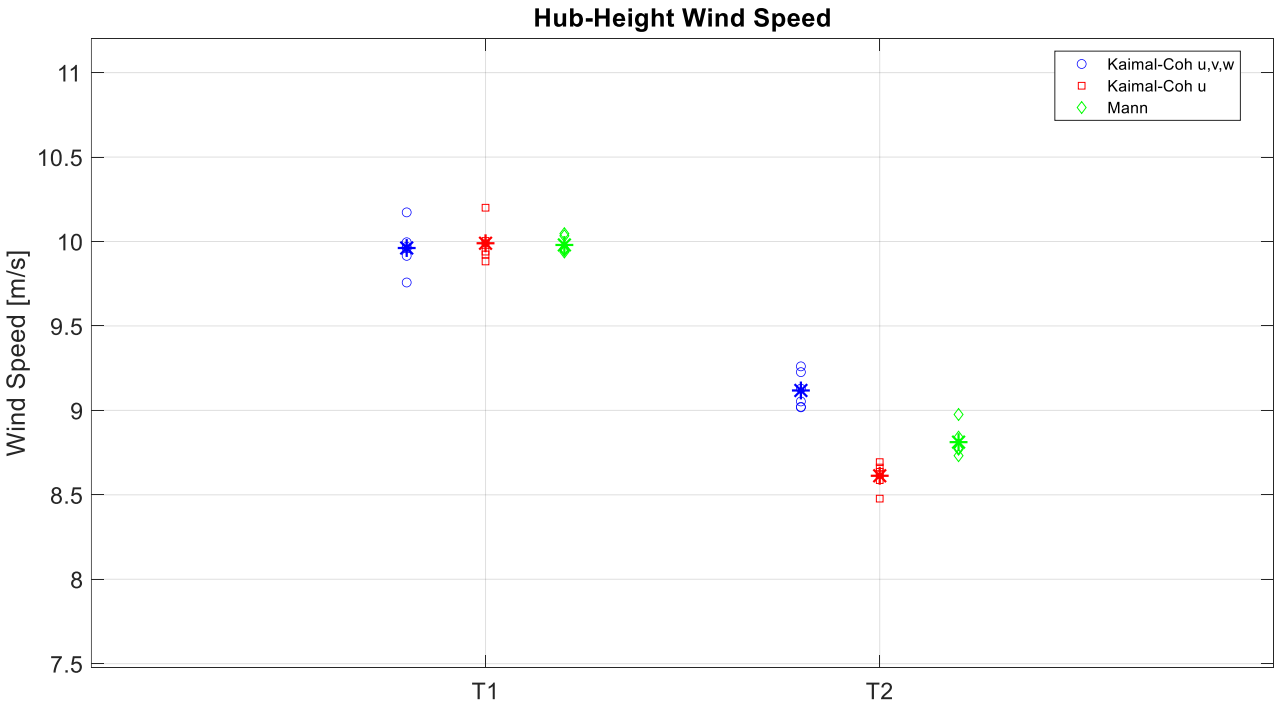

Figure 3.12: Hub-height wind speed for each wind turbine and turbulence case. Each marker represents the mean value of one simulation except for the asterisk, which represents the average over the six simulation.

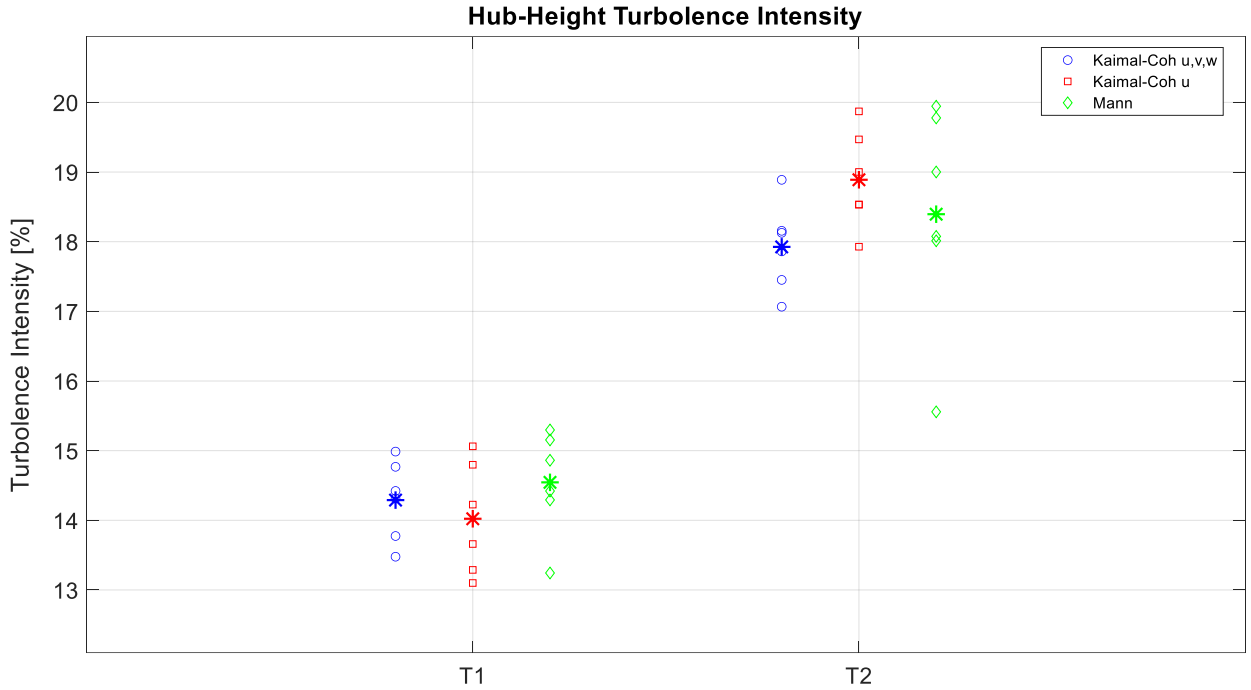

Figure 3.13: Hub-height turbulence intensity for each wind turbine and turbulence case. Each marker represents the value of one simulation except for the asterisk, which represents the average over the six simulation.

3.2.3. Platform Motions

In Figure 3.15, Figure 3.14 and Figure 3.16 are represented, respectively, the platform surge, pitch and yaw standard deviations for each wind turbine and inflow method. These three motions are referred to the reference system defined in Figure 1.2. The platform of the downwind rotor is characterized by bigger standard deviation of the motions for all the inflow typologies.

Considering the *Mann* simulations, they present a lower standard deviation for surge and pitch and a higher one for yaw with respect to the *Kaimal* realizations. This could be explainable by the larger coherent structures characterizing the *Mann* inflow field (Section 3.2.1): they are non-centred structures symmetric with respect to horizontal or vertical planes. For *Kaimal*, instead, the coherent structures are centred in the domain and occurs in pairs, opposing diagonal symmetrically [36]. The resulting force distribution on the rotor is, therefore, more even for the *Kaimal* cases. for the *Kaimal*

cases.

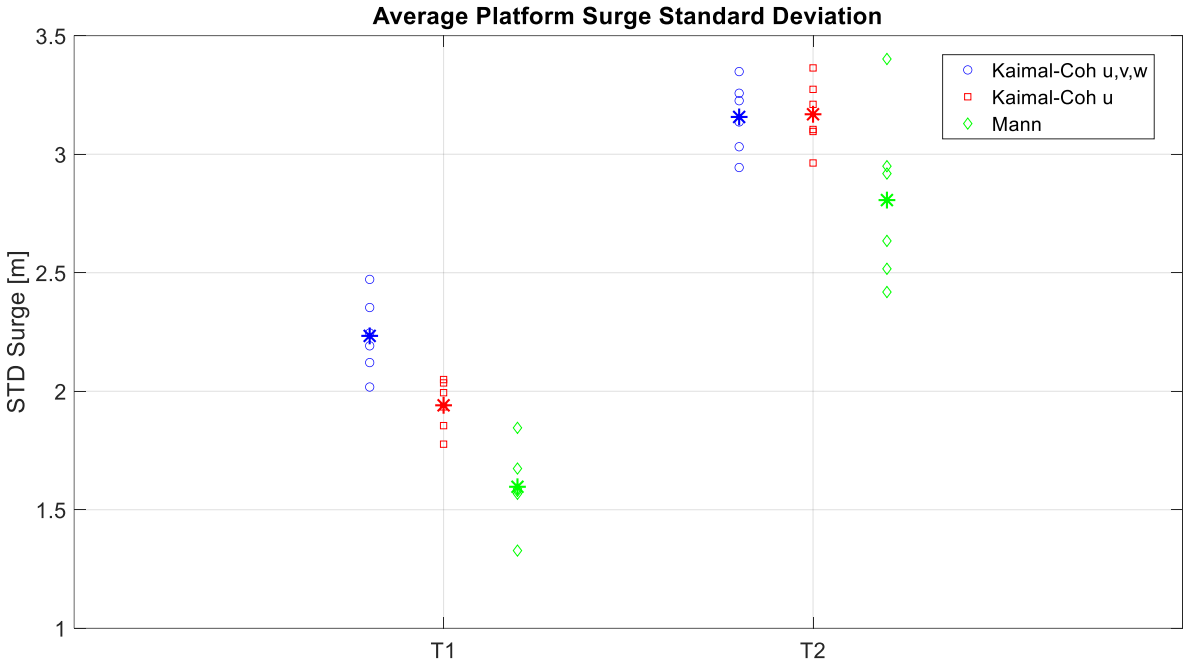

Figure 3.15: Platform Surge standard deviation for each wind turbine and turbulence case. Each marker represents the value of one simulation except for the asterisk, which represents the average over the six simulation.

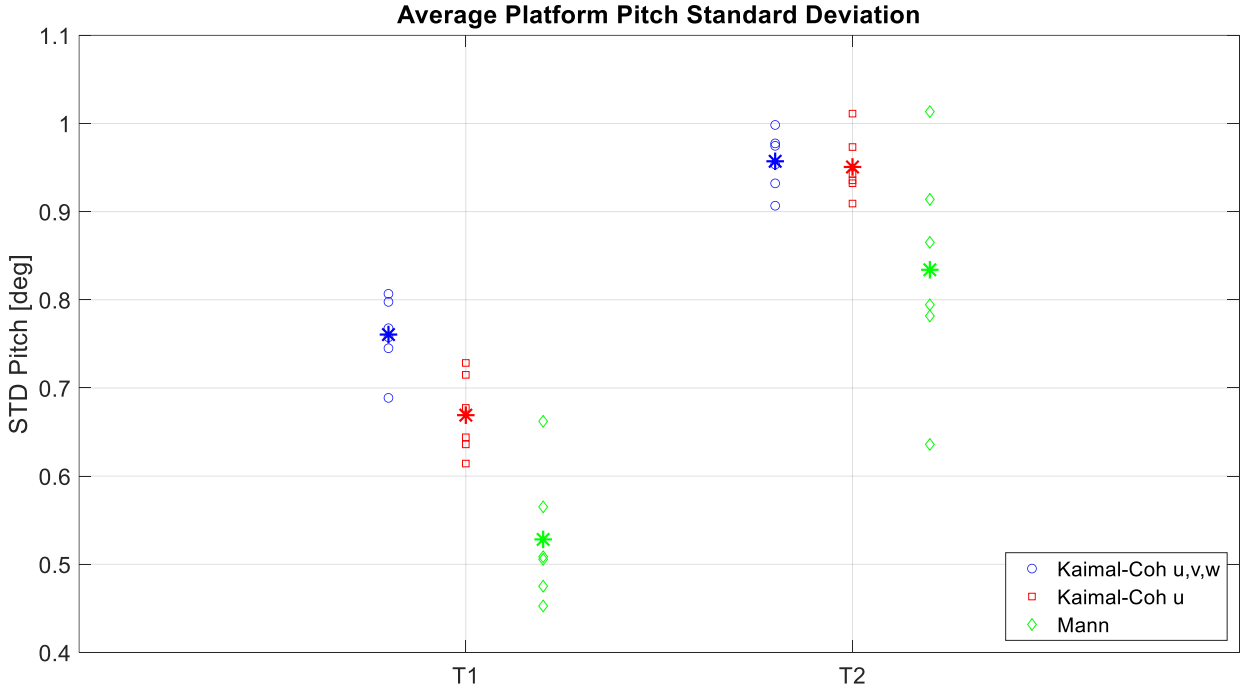

Figure 3.14: Platform pitch standard deviation for each wind turbine and turbulence case. Each marker represents the value of one simulation except for the asterisk, which represents the average over the six simulation.

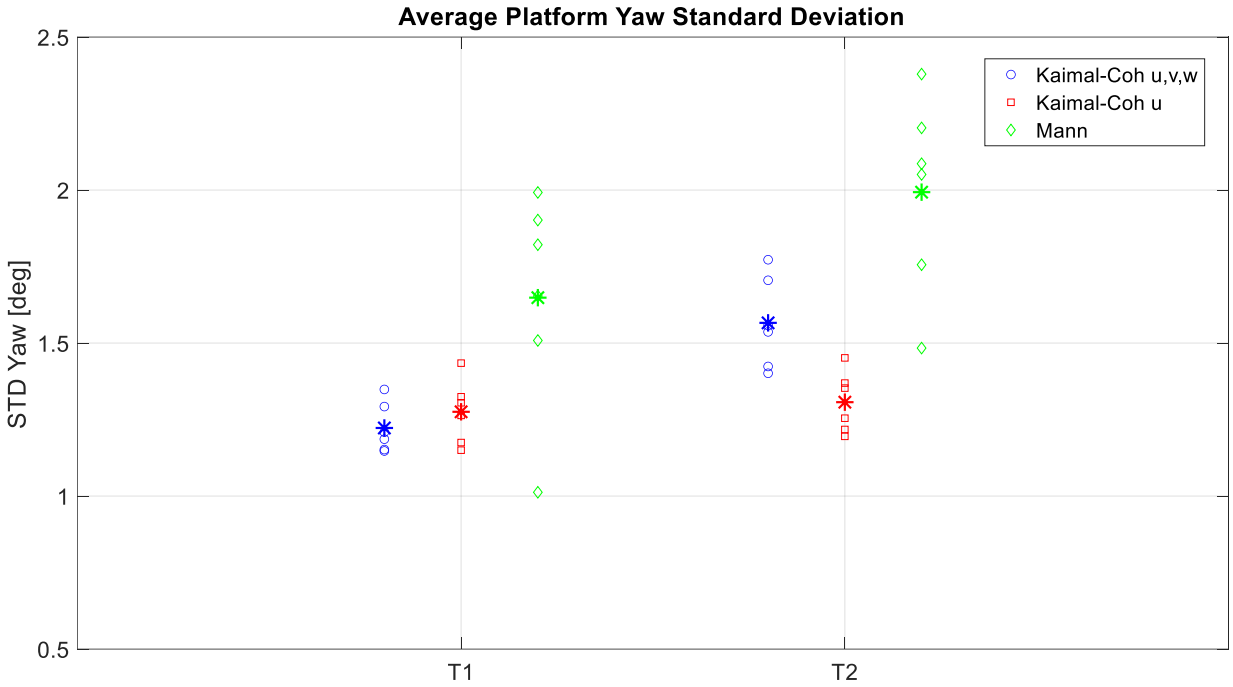

Figure 3.16: Platform yaw standard deviation for each wind turbine and turbulence case. Each marker represents the mean value of one simulation except for the asterisk, which represents the average over the six simulation.

From the PSD of the platform motions (Figure 3.17), an increase of their low-frequency (0-0.02 Hz) behaviour for the downwind turbine can be observed: it is due to the wake meandering, characterized by low frequencies (Section 3.2.1). Moreover, the peaks at the motions natural frequencies (Section 1.4) are visible.

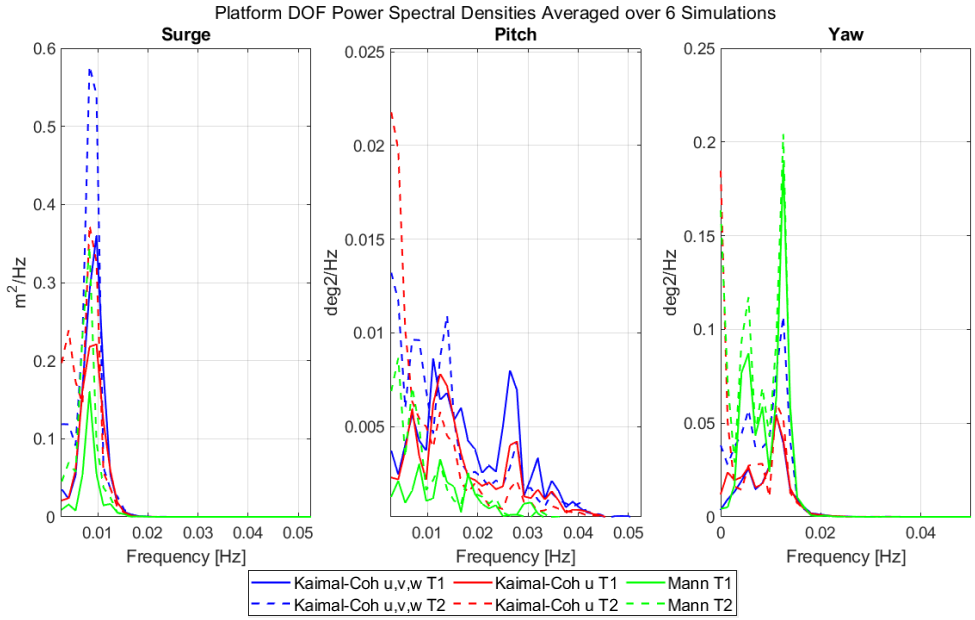

Figure 3.17: Platform motions power spectral density for each turbulence case and for each turbine.

3.2.4. Axial Stresses

Figure 3.18, shows the power spectral density of the axial stresses on the tower base and top, in the downstream point of the external shell with respect to the inflow. The plots are split into low-frequencies, wave-frequencies and tower-frequencies, each with a different ordinate scale. For both the turbines and for all the turbulence cases, the biggest amount of energy is in the low-frequency range (bigger order of magnitude), the one of the wake meandering, either for tower base either for top. For these frequency, in fact, the PSD of the axial stresses is bigger for the waked turbine. In the rightmost subplots, instead, it is possible to see the peaks for the tower pitch and bending frequencies and the effect of the 3P excitation. There is no interface between the tower natural frequencies and the 3P frequency, the frequency at which blades pass by the tower (i.e. three times the rotor frequency) (Section 1.3). 3P frequencies, one for each turbine and inflow model, are listed in Table 3.1. These excitations can impose large moments due to the tall tower [37] and affect the short-term DELs because of the high number of cycles they are calculated with. The 3P response is greater for the *Mann* turbulence than for the *Kaimal* cases. This is in accordance with literature [35] [36].

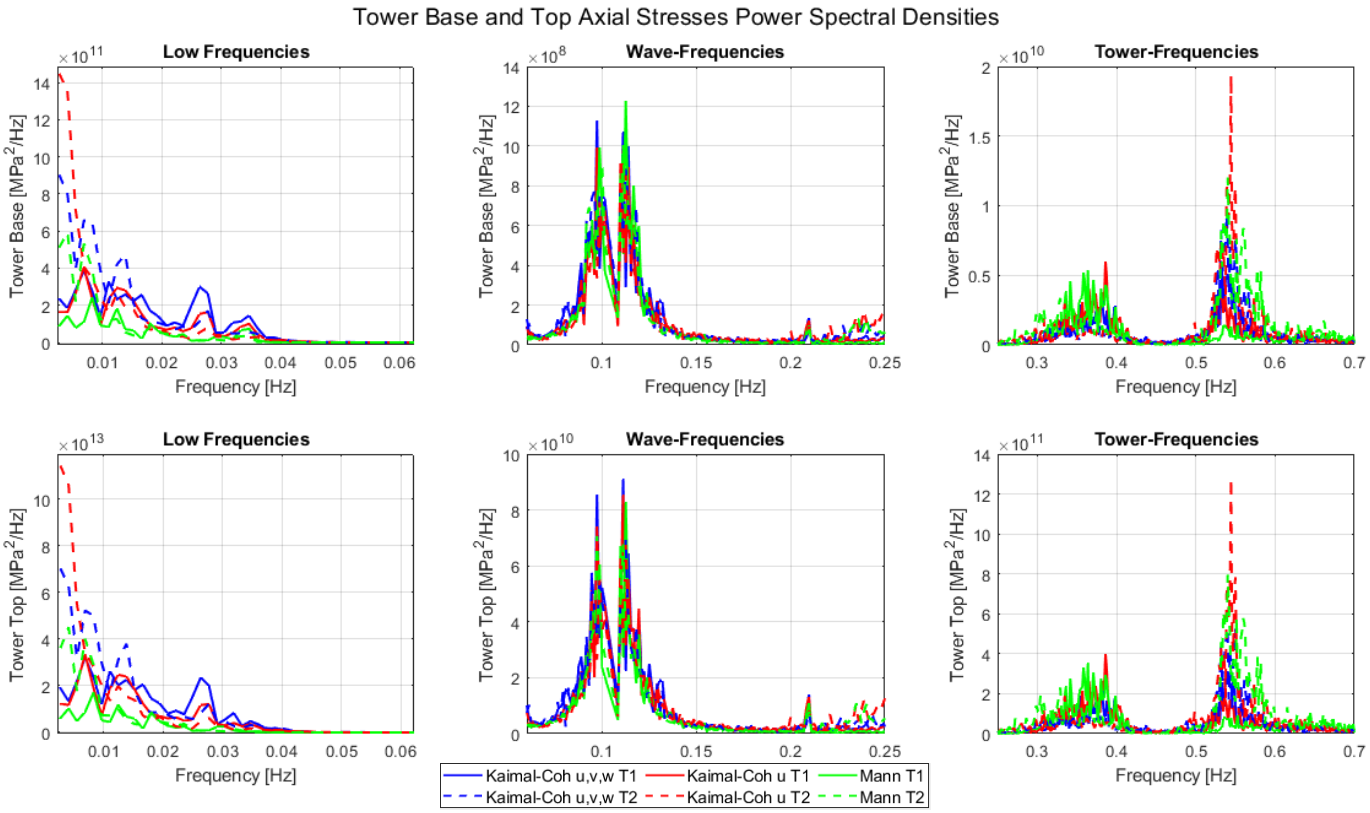

Figure 3.18: Tower base and top axial stresses power spectral density, separated into low-, wave-, and tower-ranges.

Table 3.1: 3P frequency for each wind turbine and turbulence case.

Turbulence Cases	T1	T2
Kaimal-Coh u,v,w	0.350 Hz	0.327 Hz
Kaimal-Coh u	0.352 Hz	0.315 Hz
Mann	0.354 Hz	0.321 Hz

Figure 3.19 depicts the PSD of axial stresses on the fairleads of the three mooring lines (Figure 1.5). The plots are split in the aforementioned frequency ranges, as the previous figure. In the low-frequency range, the one with the highest energy content, the trends for the second turbine are higher than the first one, for each mooring line, since it is in waked conditions, and the greatest responses are obtained with *Kaimal-Coh u, v, w* case for the first mooring line and with *Mann* for the second and third ones. In the rightmost subplot, it is possible to see the relevant peaks at the tower pitch and bending frequencies and the 3P responses. Moreover, the rotor torque moment leads to a slight roll offset; it makes the first mooring line stiffer, causing a higher response in the high-frequency range with respect to the other two mooring lines.

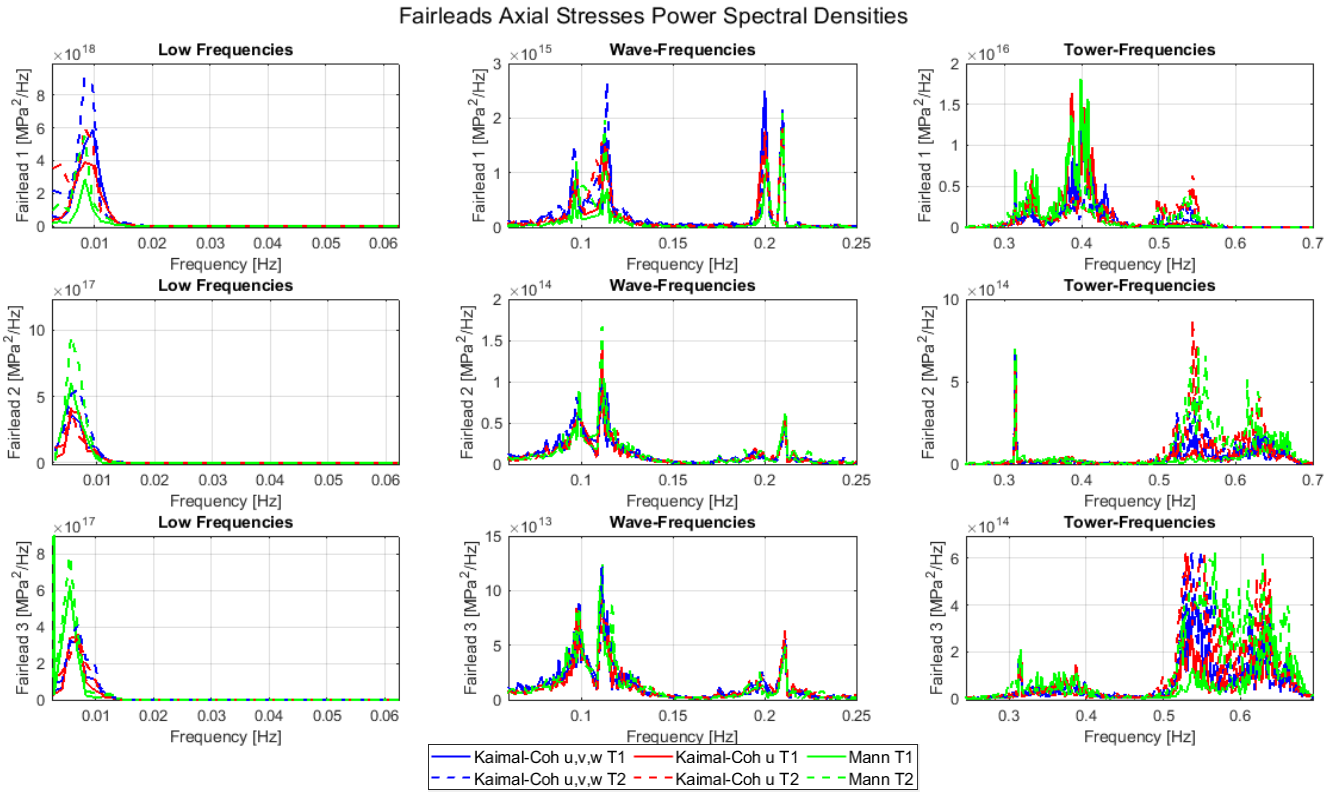

Figure 3.19: Mooring lines fairleads axial stresses power spectral density, separated into low-, wave-, and tower- ranges.

3.2.5. Fatigue Damages

For *Kaimal-Coh u,vw*, *Kaimal-Coh-u* and *Mann*, the second turbine mean 1-h x and y combined moments DELs averaged over the six simulation, increases, respectively, of 4.39%, 7.05% and 10.74% with respect to the first one at the tower base and of 4.59%, 3.83% and 4.62% at the tower top (Figure 3.20). This is a consequence of the added turbulence due to the wake from the upstream rotor [37]. In addition, it is possible to note how the DELs are higher for the tower base than for the top. At the top, *Mann* damages result the greatest ones, indicating that the tower top is more sensitive to the 3P frequency responses, which are higher for the *Mann* inflow than in the *Kaimal* cases (Figure 3.18).

The DELs due to the axial force acting on the tower have not been shown because they are much smaller than the ones caused by the moments, both for tower base and top.

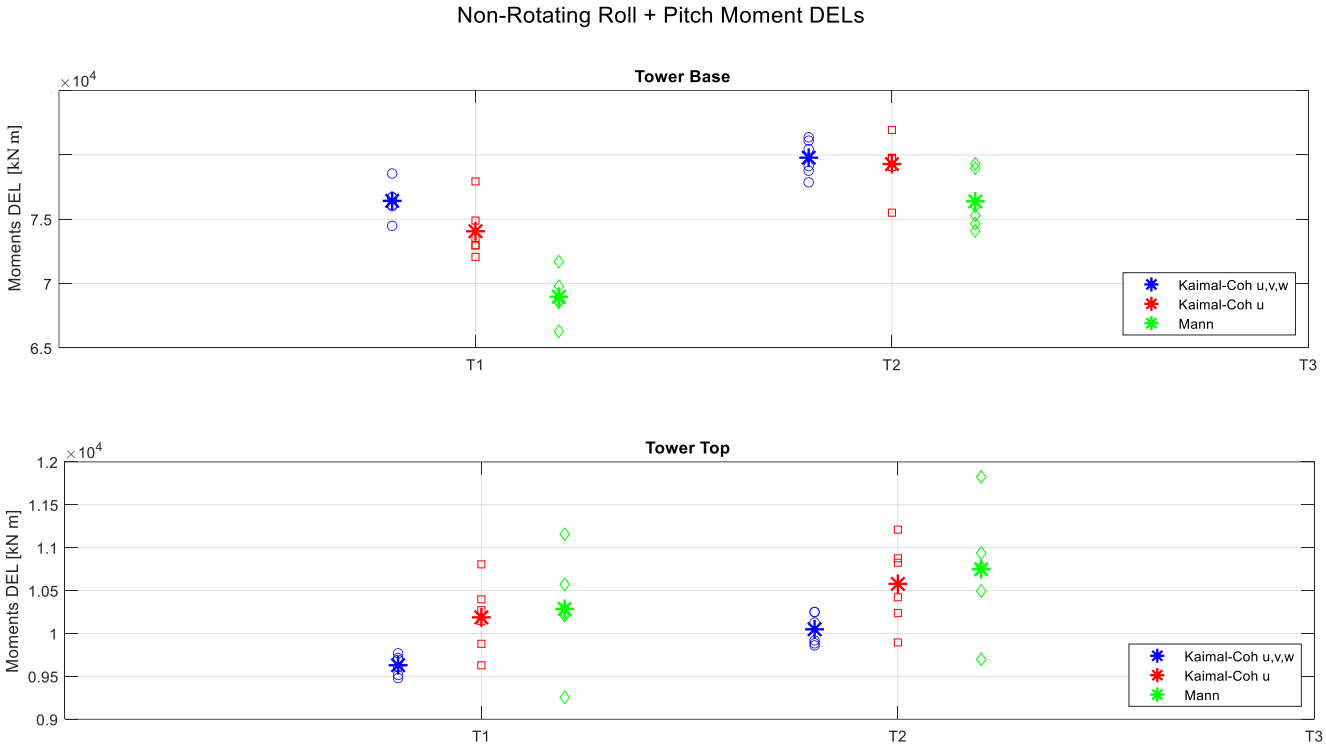

Figure 3.20: Tower base and top short-term DELs for each wind turbine and turbulence case. Each marker represents the mean value of one simulation except for the asterisk, which represents the average over the six simulation.

For *Kaimal-Coh u,vw*, *Kaimal-Coh-u* and *Mann*, the downwind turbine increases of the mean short term DEL averaged over the six simulation for the mooring lines axial stresses, are, respectively, 17.64%, 19.66% and 22.48% with respect to the upwind one for the first mooring line, 14.70%, 11.82% and 21.17% for the second and 11.50%, 11.85% and 22.81% for the third one. (Figure 3.21). The increase is related to the low-frequency response of the mooring line axial stresses power spectral density.

The first mooring line is the one which suffer the highest DELs and their greatest values occur for the *Kaimal-Coh u, v, w* case. In the second and third one, instead, it is possible to note how the worst fatigue damages are obtained for the *Mann* turbulence. This is in accordance with the fairleads axial stresses response in the low-frequency range, which is the one with the highest energy content (Figure 3.19).

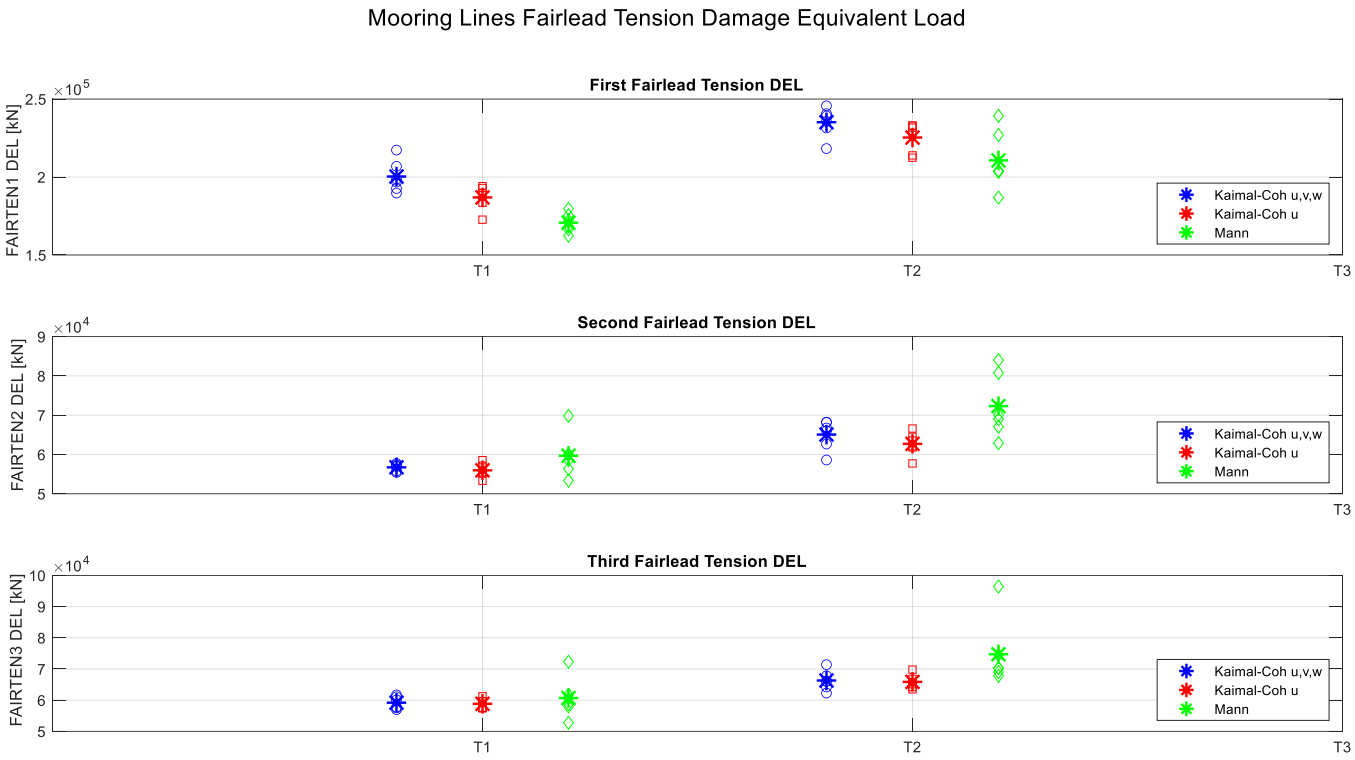

Figure 3.21: Mooring lines short-term DELs for each wind turbine and turbulence case. Each marker represents the mean value of one simulation except for the asterisk, which represents the average over the six simulation.

3.3. Conclusions

The results are coherent with the ones of the reference A. Wise and E. E. Bachynski paper [29]:

- Wake meandering is mainly a low-frequency (0-0.02 Hz) phenomenon and it is the most intense with *Kaimal-Coh u,v,w* and the lowest with *Kaimal-Coh u*;
- *Mann* model presents stretched coherent structures;
- The waked turbine is penalized in terms of hub wind velocity and TI (in particular with *Kaimal-Coh u*), platform motions (especially in the low-frequency range), low-frequency axial stressesand DELs at the tower base and top and at the mooring lines fairleads;
- The platform surge and pitch wake-related increase is the lowest with *Mann*, which, instead, leads to the worst yaw increase;
- The 3P axial stresses excitations are higher with *Mann*;
- Tower top is more sensitive to 3P responses, in terms of DELs, than tower base.
- The mooring systems DELs reflect mainly the low-frequency axial stresses behaviour and are higher for the first line.

There are, anyway, differences in the magnitude of the analysed variables and in the fatigue response, mainly due to the different control dynamic and natural design tower frequencies. For example, in the present case, there is no interface between the 3P frequency and the tower natural frequencies, while in the reference paper the latters are excited by the 3P one, influencing the fatigue damages results.

For each type of turbulence method, it is possible to conclude that the downstream turbine feels a lower horizontal wind velocity and a higher turbulence intensity at the hub, penalizing the quantity and quality of the extractable power. In addition it is characterized by higher platform motions and it suffers from higher low-frequency axial stresses and, consequently, higher fatigue damages than the upstream one, since it operates in waked conditions. In addition, *Kaimal-Coh u,v,w* turbulence implies the biggest wake meandering, the central phenomenon of the present work.

4 Wake Analysis of a Seven Turbines Wind Farm

Once the A. Wise and E. E. Bachynski wakes study [29] has been similarly reproduced on the two-turbines configuration with the IEA 15-MW Floating Offshore Wind Turbine, the method have been extended to a more complex seven-turbines layout, derived from the TotalControl Reference Wind Power Plant (TC RWP) configuration [38].

The considered turbine model has been always the IEA 15-MW Floating Offshore Wind Turbine (Chapter 1).

The aim was that to test the wake influence on the response of the TC RWP arrangement used with the IEA 15-MW Floating Offshore Wind Turbine. A reduced geometry has been anyway analysed since the TC RWP one is composed by 32 turbines, requiring a too high computational cost to perform the simulations.

4.1. Methodology

The adopted methodology is the same of the two-turbines study, in the previous chapter (3.1), inspired to the A. Wise and E. E. Bachynski analysis [29].

4.1.1. Geometrical Layout and Resolution

The geometry object of the present work have been chosen as a seven turbines recurrent subset of the TotalControl Reference Wind Power Plant (TC RWP) [38]. The TC RWP is compound by 32 turbines organised in staggered rows and columns separated among them by 5D, with the wind inflow coming from the left as the main direction (Figure 4.1).

In this configuration, recurrent hexagonal patterns of seven turbines, (six at the vertices and one in the centre) can be identified (Figure 4.1).

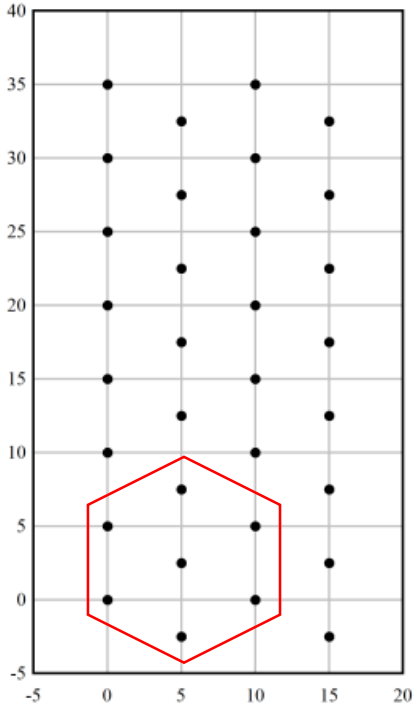

Figure 4.1: TotalControl Reference Wind Power Plant configuration. Axes are normalized on a the diameter of 198 m, the one of the rotors originally used in the TC RWP. The red hexagon indicates the recurrent seven-turbines pattern. The wind inflow comes from the left as main direction.

The arrangement analysed in this chapter, has been derived in this way and it is shown in the FAST.Farm low-resolution domain in Figure 4.2. The principal wind flow direction and verse are the same of the x-axis ones and the turbine's diameter D is 241.94 m. Turbines are referred as T1, T2, T3, T4, T5, T6 and T7, as indicated in the picture. It is important to note that the 5D distance is both among different turbines' lines and columns, but the T1-T6 distance and the T2-T7 one are 10D.

The FAST.Farm low-resolution domain (Section 2.1.1.3) spatial and temporal discretization are the same of the Wise and Bachynski study [29] and of the two-turbine case (Section 3.1.1). Its origin and number of points in x and z direction are the same of the two-turbine layout, while in y they have been set to -1350 m and 271 points, respectively. The turbine at the centre of the hexagon has been placed at y = 0 m. In this way, the low-resolution domain encompasses all the turbines, considering any possible displacement, and the resulting grid dimensions in x, y and z are: 4975 m (from 0 m to 4975 m), 2700 m (from -1350 m to +1350 m) and 270 m (from 10 m to 280 m).

The FAST.Farm high-resolution domains (Section 2.1.1.3), are analogous to the ones of the two-turbies analysis (Section 3.1.1). Each high-resolution domain encompass its turbine and any possible displacement.

The grid of the low- and high-resolution domains are shown together in Figure 4.3.

The parameters of the wake radial finite-difference grid (Section 2.1.1.2) are the same of the previous case too (Section 3.1.1).

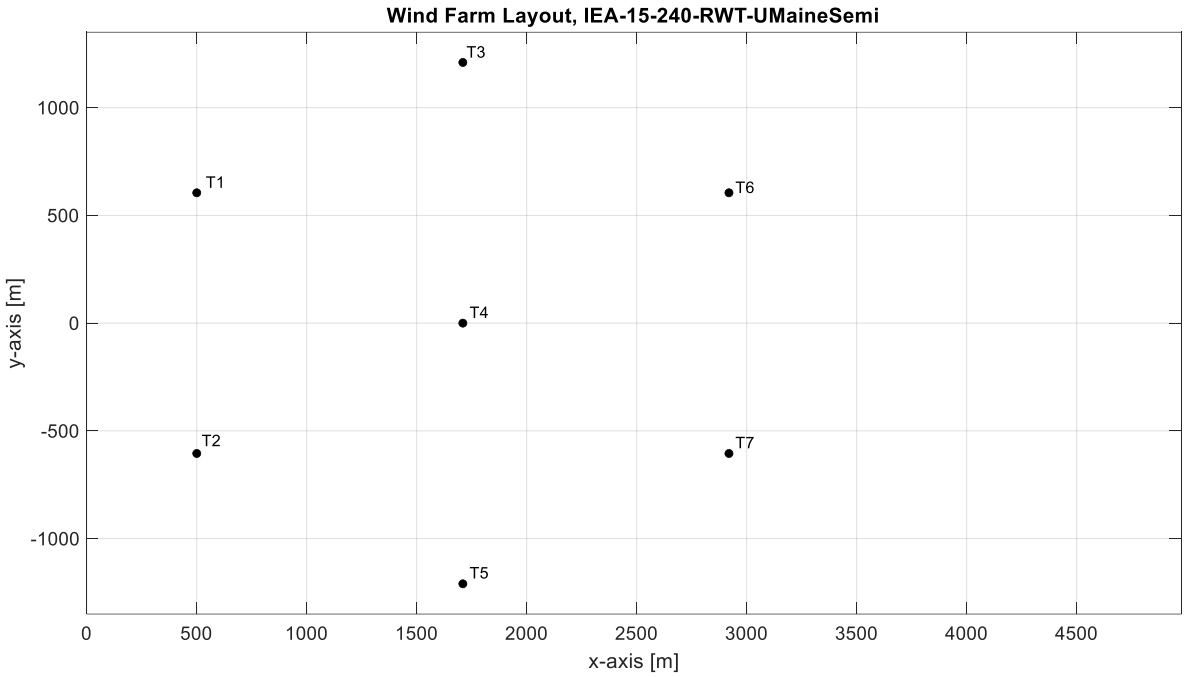

Figure 4.2: Seven IEA 15-MW Floating Offshore Wind Turbines configuration visualized in the FAST.Farm low-resolution domain.

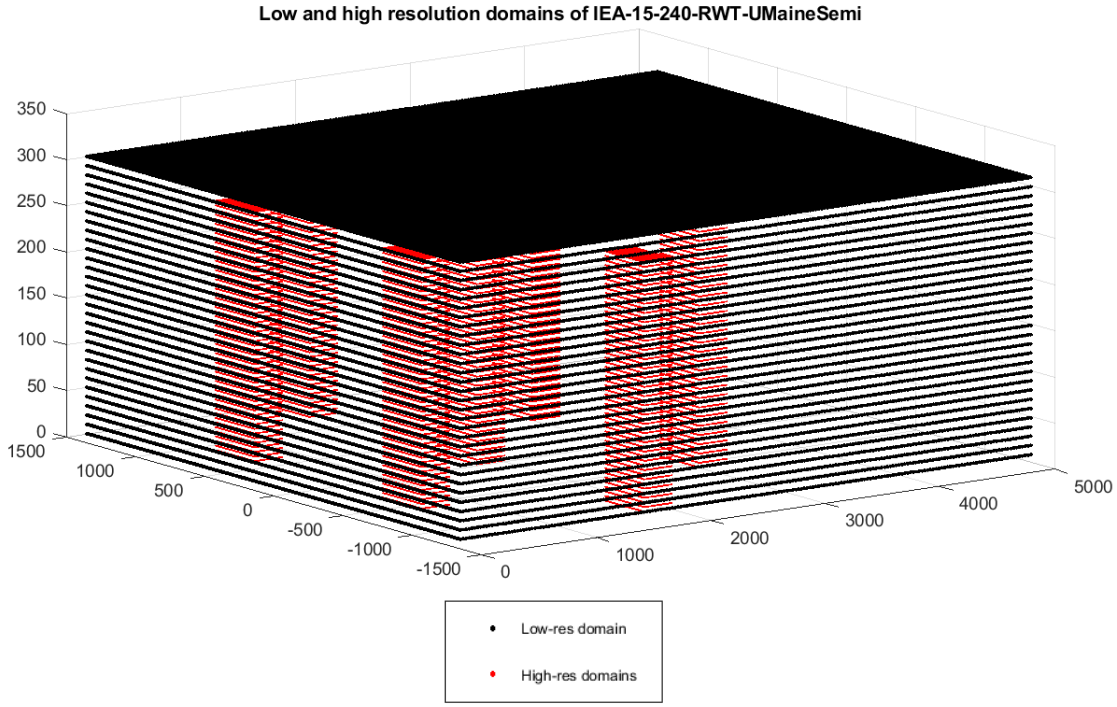

Figure 4.3: FAST.Farm low- and high-resolution domains grid of the seven IEA 15-MW Floating Offshore Wind Turbines configuration.

4.1.2. Environmental Conditions

The same ambient proprieties and North-Sea location of the two-turbines analysis (Section 3.1.2) have been considered.

4.1.3. Pre-Simulation Identification

As for the previous case (Section 3.1.3, the duration of the pre-simulation transient has been identified by running a simulation of the farm with steady wind conditions (Section 2.1.1.3) at the hub-height horizontal wind velocity of the analysis (10 m/s) and parked turbines; the rotors have been stopped through a HSS brake. Then, the trend of the disturbed horizontal wind speed has been observed in five points, which are at the end of the low-resolution domain in x direction (x=4975) and at the hub height (z=148.35 m). They differ among them for the y-coordinate: one point has the y equal to the one of T3, one is aligned in y with T1 and T6, one has the y of the central turbine (T4) and one share the same y of T2 and T7. These points can be visualised in red in the low-resolution domain in Figure 4.4.

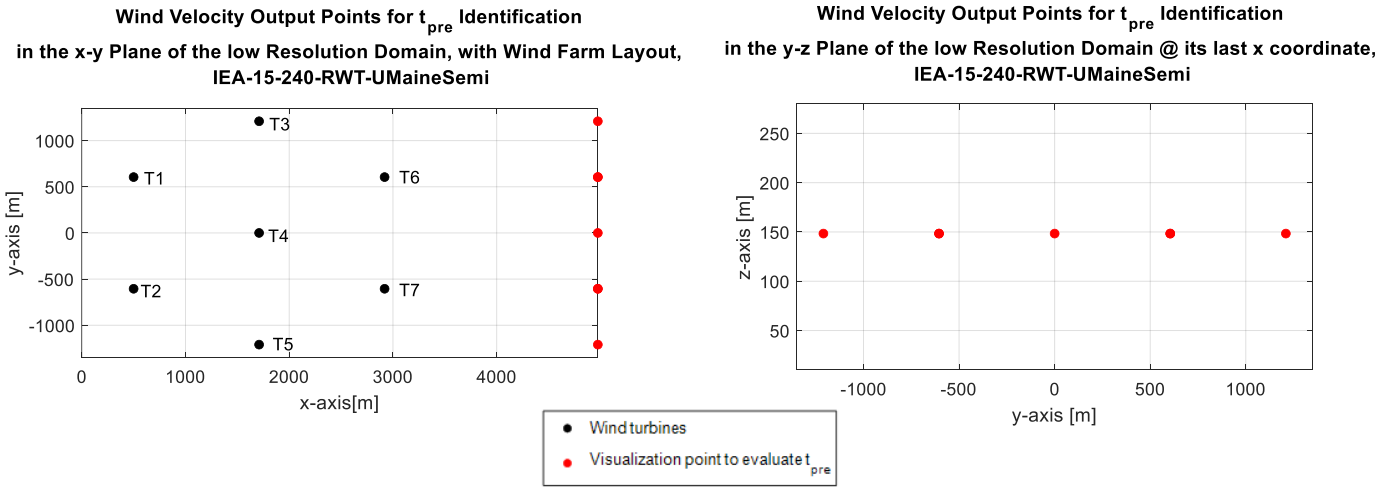

Figure 4.4: Disturbed horizontal wind velocity output points to evaluate the pre-simulation duration, visualized in the x-y (left) and y-z (right) planes of the low-resolution domain.

The case for which the transient is the longest has been obtained for the two downstream points aligned in y respectively with T1-T6 and T2-T7. The time history of the horizontal disturbed wind velocity in these points is plotted in Figure 4.5.
The end instant of the pre-simulation (t_{pre}), indicated with a vertical red line in this figure, has been placed at 1200 s, considering an excess security margin. During the data post-processing, all the analysed FAST.Farm output variables values occurring before t_{pre}, have been not considered. It is noteworthy that t_{pre} is bigger in the seven-turbines case than in the two-turbines configuration (Section 3.1.3). The latter is in fact characterized by stronger perturbations for what concern the last turbine, as demonstrated later in this Section.

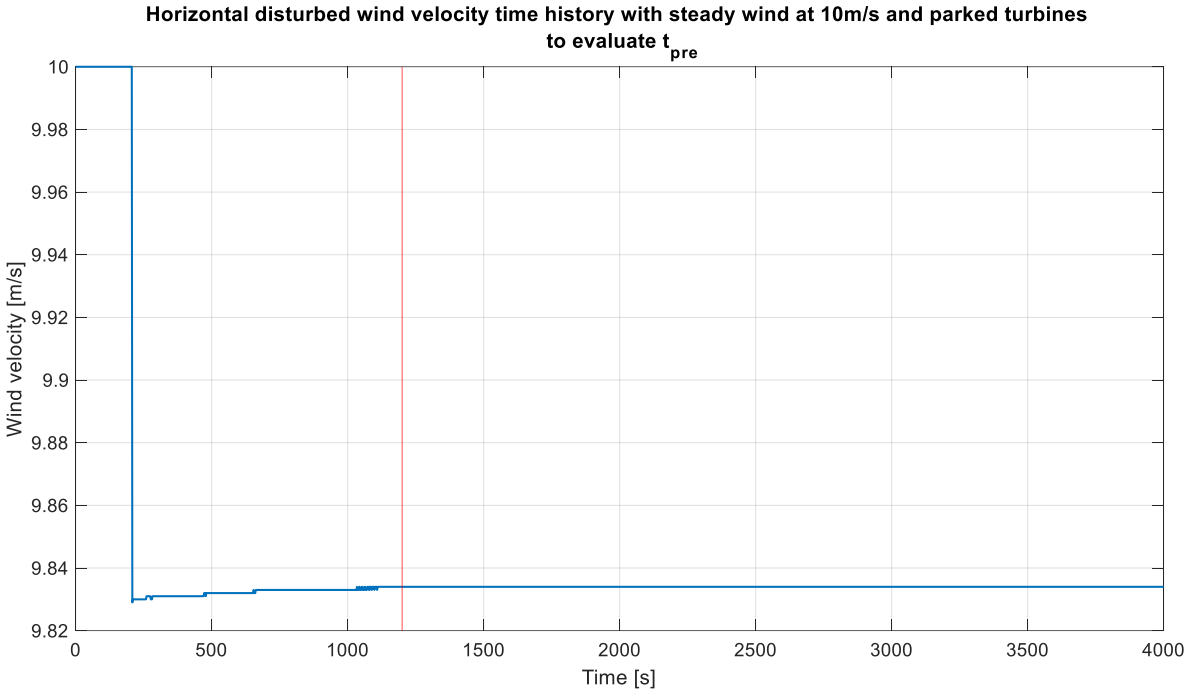

Figure 4.5: Horizontal disturbed wind velocity trend to evaluate t_{pre} with steady wind condition at 10 m/s and parked turbines.

4.1.4. Simulations

As for the two-turbines farm (Section 3.1.4), six simulation of 1 h (4800 s minus 1200s of pre-simulation) for each turbulent inflow model (*Kaimal-Coh u,v,w*, *Kaimal-Coh u* and *Mann*) have been launched, changing the random seed and keeping the other parameters constant and equal to the ones described in Wise and Bachynski study [29].

The dimensions and resolution of the Turbsim grid (Section 2.2.1), for the Kaimal cases, and of the Turbulence Mann Generator grid (Section 2.2.2), for the *Mann* case, have been the only modifications to contain the new and bigger low-resolution domain.

The resolution have been diminished with respect to the two-turbines layout, in order to avoid an excessive computational cost, especially for Turbsim.

4.1.5. Axial Stresses and Fatigue Damages Calculation

The axial stresses and the 1-h DEL at the downstream point (with respect to the wind inflow) of the tower base and top external shell and at the mooring lines fairlead , have been evaluated likewise to the previous case (Sections 3.1.5 and 3.1.6).

4.2. Results

4.2.1. Flow Visualization and Wakes Centre

An instantaneous horizontal wind velocity visualization in the low-resolution domain x-y plane at the hub height, for the last instant of the first simulation of the *Kaimal-Coh u,v,w*, *Kaimal-Coh u* and *Mann* method, respectively, is provided in the colormaps of Figure 4.6. The latter, from which is possible to distinguish wake deflection and merging phenomena, should be seen together with Figure 4.7. It representing the instantaneous wake centre positions in the low-resolution domain x-y plane normalized on the turbines' diameter at the hub height, for the last instant of the first simulation of each of the three turbulence cases. As for the two-turbines case (3.2.1), it is clear that the *Kaimal-Coh u,v,w* implies much more lateral (y) meandering that *Kamal-Coh u*.

The same conclusion is valid also for the vertical (z) meandering, even if it is not shown.

The u, v and w extension of the coherent structures are visible for *Mann* too, and for this inflow model, they are more stretched than the *Kaimal* inflows (Figure 4.6), as for the two-turbine configuration (Section 3.2.1). As explained before, this typical characteristic of the *Mann* turbulence [35] has a great influence on the farm's response.

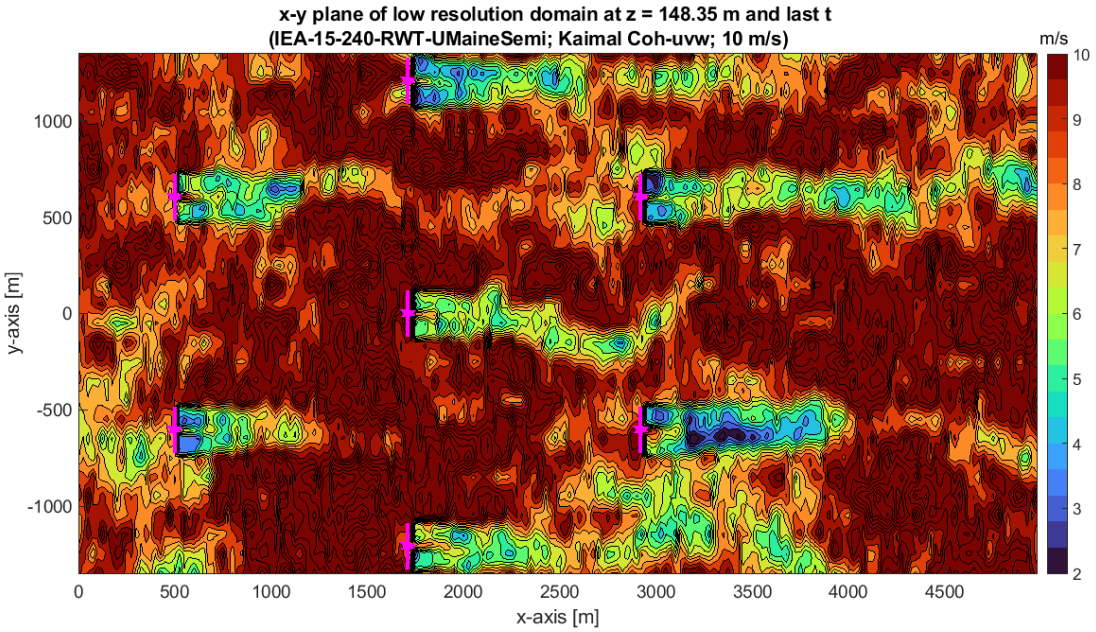

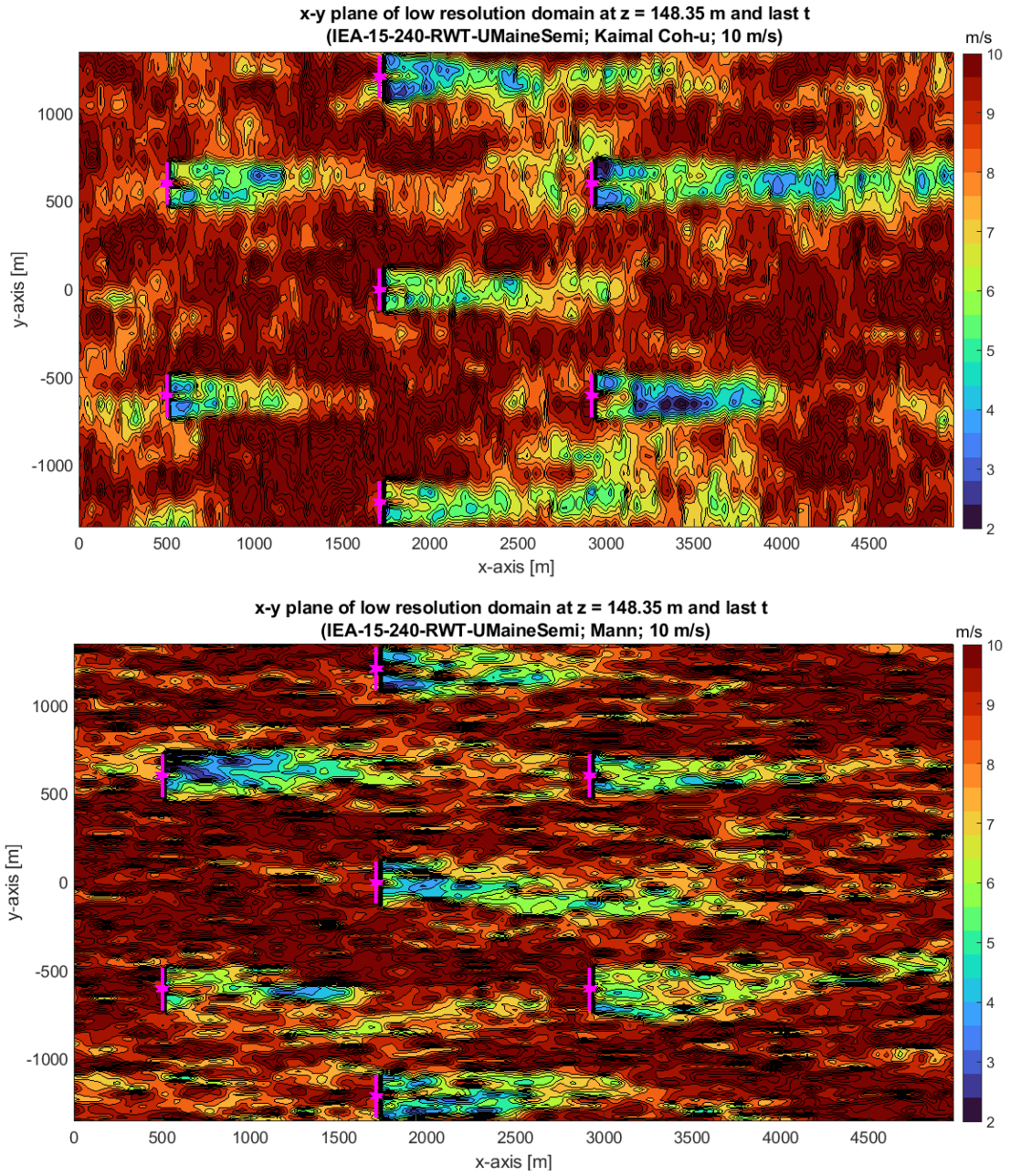

Figure 4.6: Instantaneous (last simulation instant) wind flow field for the first simulation of the *Kaimal-Coh u,v,w* (top) , *Kaimal-Coh u* (middle) and *Mann* (bottom) turbulence case in the low-resolution domain of the seven IEA 15-MW Floating Offshore Wind Turbines configuration. Rotors are repr esented in magenta.

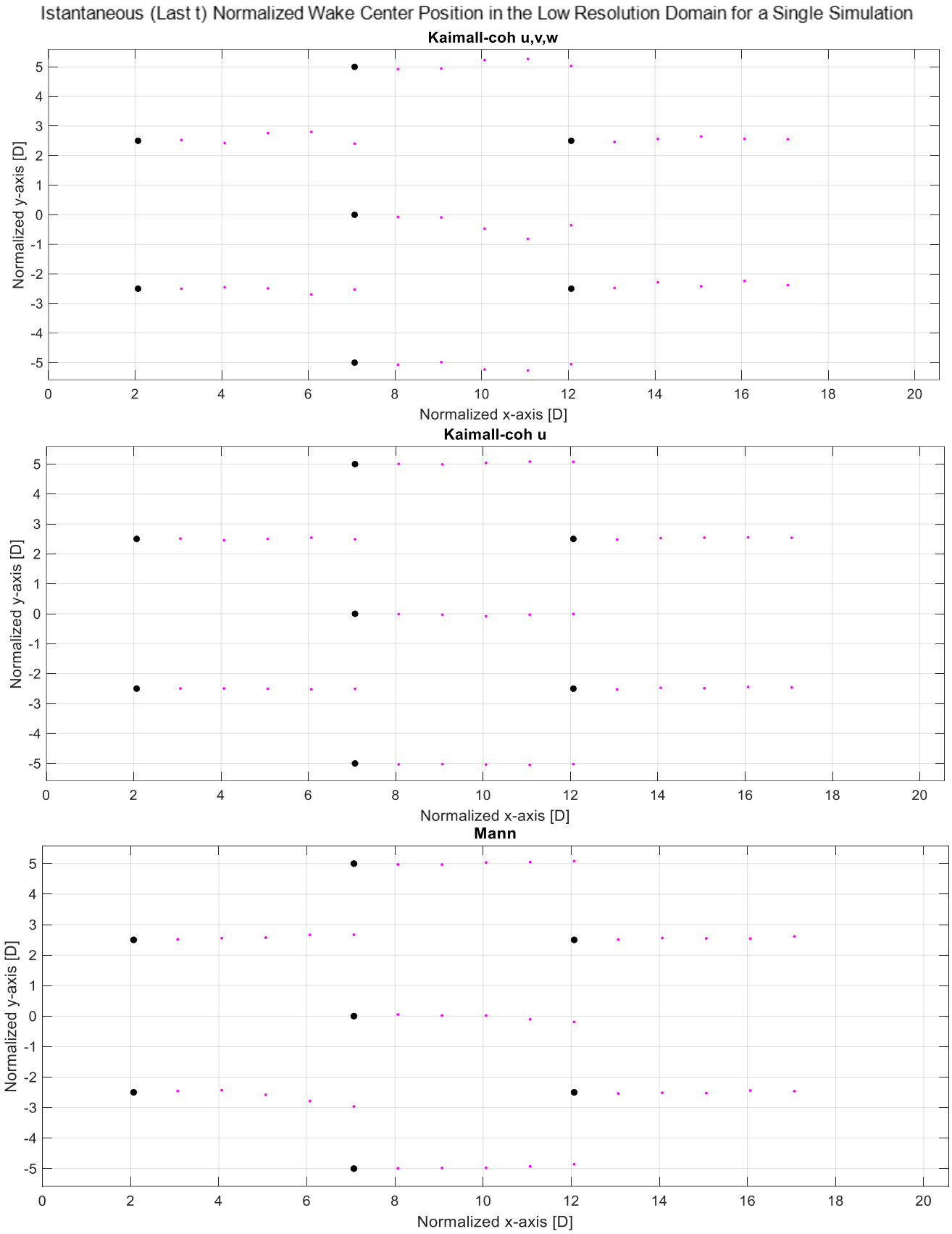

Figure 4.7: Instantaneous (last simulation instant) wake center position till 5D for the first simulation of the *Kaimal-Coh u,v,w* (top) , *Kaimal-Coh u* (middle) and *Mann* (bottom) turbulence case in the normalized low-resolution domain of the two IEA 15-MW Floating Offshore Wind Turbines configuration. Rotors are represented in black.

Considering all the simulation and not just an instantaneous framework, it is more evident, from the wake centre lateral (y) position standard deviation at 5D (Figure 4.8), that, for all the turbines except T3 and T5 (Figure 4.2), the inflow model involving the greatest meandering is the *Kaimal-Coh u,v,w* one, followed by the *Mann* one. The meandering with the *Kaimal-Coh u* model is instead very limited, confirming the upshot of the two-turbine layout.

For T3 and T5, instead, the meandering in the *kaimal* cases becomes more relevant with respect to the other turbines, for which it is, instead, almost constant among them. For these two rotors, the *Kaimal-Coh u* 6-simulations averaged standard deviation of the wake lateral position overcomes the one of the *Mann* case.

The reason is probably the deflection of the wakes of the upwind turbines, T1 and T2 towards T3 and T5 (Figure 4.2) and to the consequent merging of the wakes, occuring less with the Mann model.

This result is anyway not generalizable due to the high randomization characterizing the inflow field in a complex layout farm and the inadequacy of the only standard deviation to summarize completely the wakes' behaviour. The standard deviation for T3 and T5 is, in fact, characterized by a high uncertainty in the *Kaimal* cases, as visible in Figure 4.8 (worst case: ±34.86% for T3 with *Kaimal-Coh u, v, w*).

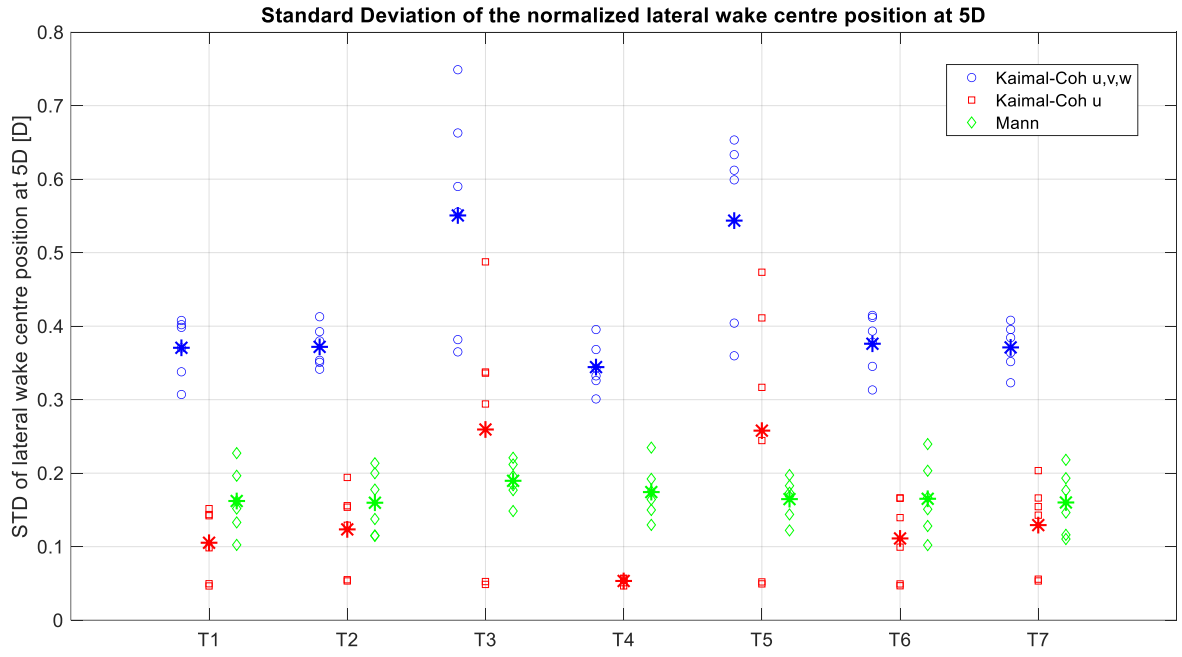

Figure 4.8: Standard deviation of lateral wake center position at 5D downstream from each wind turbine and for each turbulence case. Each marker represents the value of one simulation except for the asterisk, which represents the average over the six simulation.

In Figure 4.9, the power spectral density of the 5D lateral wake meandering for each turbine and turbulence case is depicted. Almost all the energy content is concentred in the 0-0.02 Hz frequency range, for all the turbines with *Kaimal-Coh u,v,w* and *Mann* models.

The PSD with *Kaimal-Coh u* is, instead, very limited, while the highest response is always obtained with the *Kaimal-Coh u,v,w* case, for which it is also the most low-frequency one but presents also components at higher frequencies than for the *Mann* method. This is in accordance with the two-turbines study (Section 3.2.1) and with the Wise and Bachynski analysis [29].

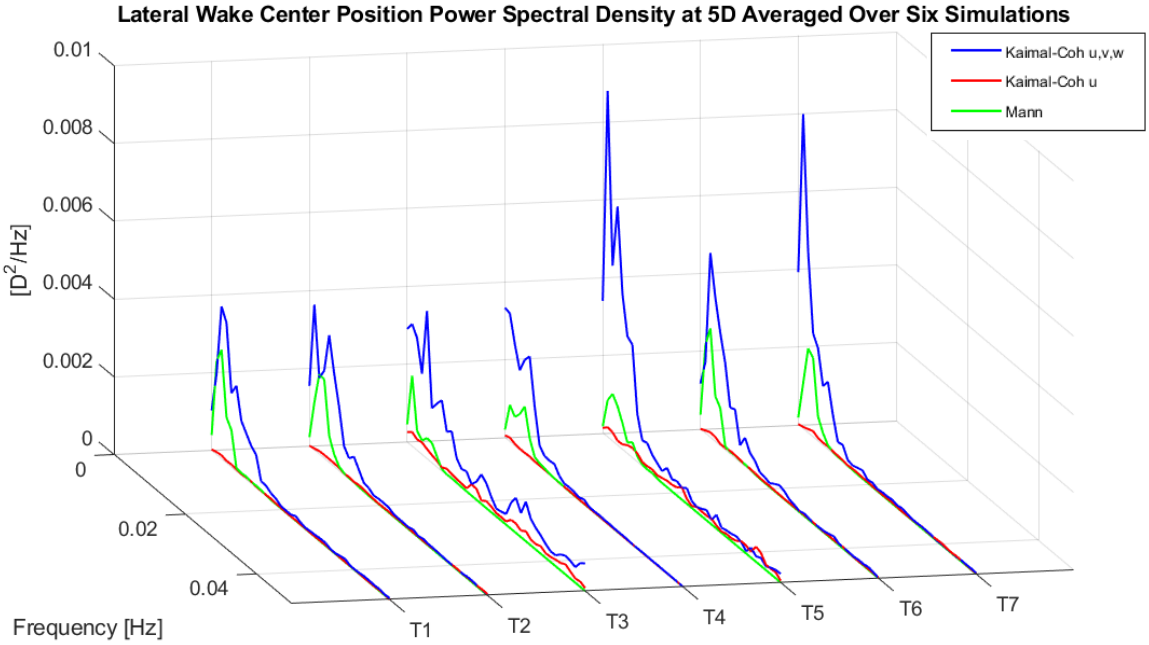

Figure 4.9: Lateral wake center position power spectral density for each wind turbine and turbulence case.

4.2.2. Wind Velocity and Turbulence Intensity at the Hubs

From the mean horizontal wind velocity at the hubs (Figure 4.10), it is possible to observe that for each turbine the offset from the reference speed (10 m/s) is weak, evidencing the goodness of this farm layout in terms of performance. For the first five turbines (T1, T2, T3, T4 and T5), the averaged values are even greater than 10m/s for some cases, and anyway the deviations are very limited (1.10% at most), suggesting that, they don't operate in a waked condition. This will be confirmed later (Sections 5.2.1 and 5.2.2).

The biggest reductions from the reference velocity (10m/s) are, instead, obtained for the most downwind turbines (T6 and T7) in the two *Kaimal* cases; for T6 the hub averaged wind velocity is about 1.86% and 2.31% lower than the reference speed with

Kaimal-Coh u, v, w and with *Kaimal-Coh u*, respectively, while for T7 they are about 2.37% and 3.47%. They are anyway contained values compared to the ones for the downstream turbine in the two-turbines case, $T2_{previous}$ (8.82% with *Kaimal-Coh u, v, w*, 13.87% with *Kaimal-Coh u* and 11.88% with *Mann*, Section 3.2.2).

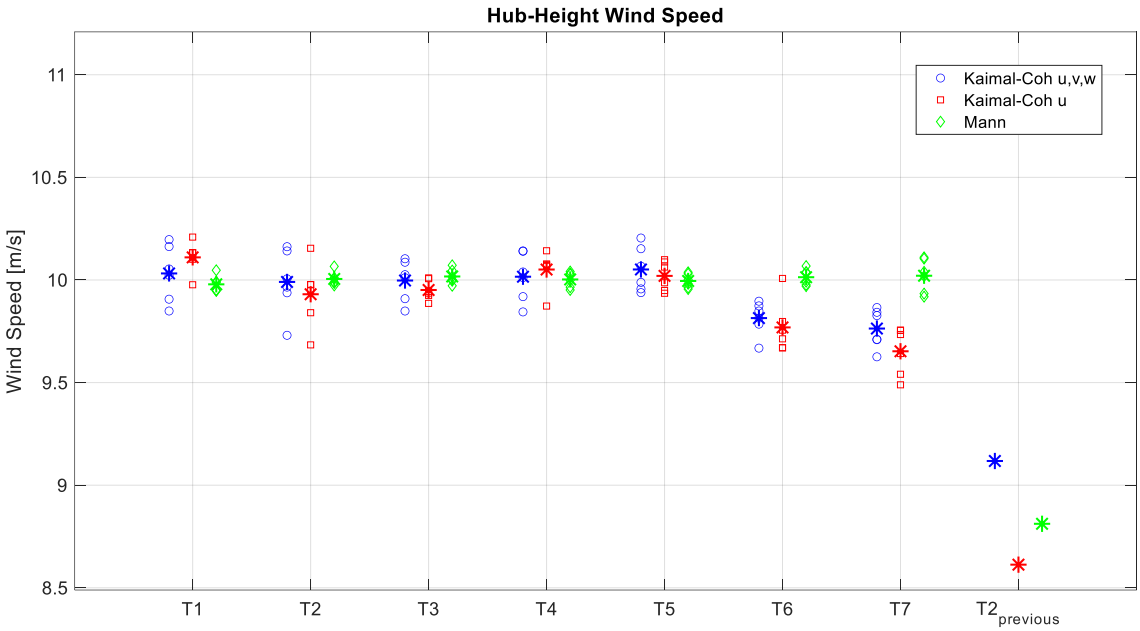

Figure 4.10: Hub wind speed for each wind turbine and turbulence case. Each marker represents the mean value of one simulation except for the asterisk, which represents the average over the six simulation.

Considering the hub turbulence intensity TI (Figure 4.11), the six-simulations averaged values are included between 10.5% and about 14%. In this terms, this layout is therefore better than the unstaggered 8D distanced one (two-turbines case), for which the downstream turbine ($T2_{previous}$) is characterized by averaged values in the range 18% (almost)-19% (Section 3.2.2).

Anyway, the TI estimation is characterized by high uncertainty due to the strong randomization of the turbulent flow field with a farm layout of this type.
This is visible moreover for the *Mann* model, probably because of its larger and non-centred coherent structures. The worst case for the averaged value is at T3 hub in the *Mann* case (14.3%), characterized by an uncertainty of $\pm$ 28.64% (Figure 4.11).

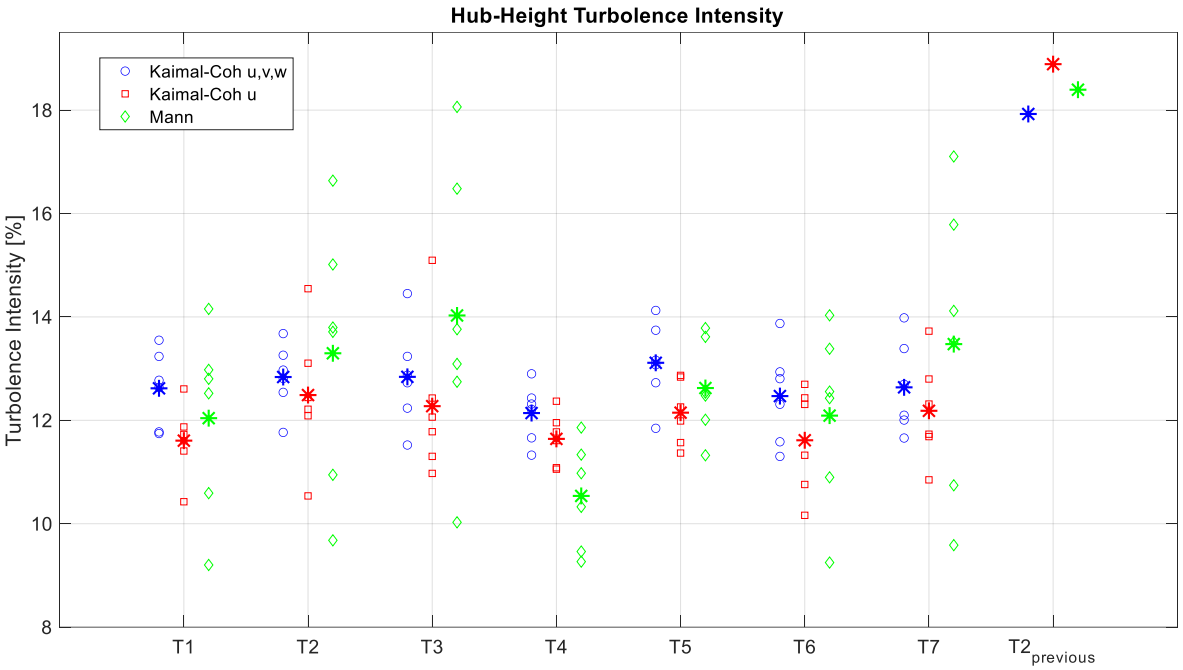

Figure 4.11: Hub turbulence intensity for each wind turbine and turbulence case. Each marker represents the value of one simulation except for the asterisk, which represents the average over the six simulation.

4.2.3. Platform Motions

For what concern the platform motions, surge, pitch and yaw have been analysed, which are defined with respect to the reference system of Figure 1.2. The standard deviations of these motions for each wind turbine and inflow method are shown in Figure 4.12, Figure 4.13 and Figure 4.14.

With *Kaimal-Coh u, v, w* the surge standard deviation averaged over six simulations is for all the turbines among 1.95m and 2.37m, while it is included between 1.71m and 2.01m and between 0.92m and 1.18m with *Kaimal-Coh u* and *Mann*, respectively.

For the pitch, instead, the boundary ranges of the averaged values are 0.74°-0.79° using *Kaimal-Coh u, v, w* spectrum, 0.67°-0.7° with *Kaimal-Coh u* and 0.39°-0.45° for *Mann*.

The limits for the averaged yaw standard deviation are 1.12°-1.24° in the *Kaimal-Coh u,v,w* case, 1.13°-1.24° in the *Kaimal-Coh u* case and 1.55°-1.32° in the *Mann* one.

These values are in all cases and for each turbine, similar to the upwind turbines' (T1 and T2) platform STDs and lower than the ones affecting the downstream turbine's in the two-turbines layout ($T2_{previous}$). In the latter case, the surge, pitch and yaw averaged values ranges are, respectively: 2.81m-3.17m, 0.83°-0.96° and 1.31°-1.99° (Section 3.2.3). Whereas, accordingly with the two-turbines analysis results (Section 3.2.3), comparing the *Mann* inflow with the *Kaimal* ones, the standard deviations are lower

for pitch and surge and higher for yaw. This is due to the stretched non-centered structures of the Mann model, symmetric with respect to horizontal or vertical planes, which, instead, are centred in the domain and occurs opposing diagonal symmetrically in pairs for the *Kaimal* spectra, causing a more even rotor force distribution [45].

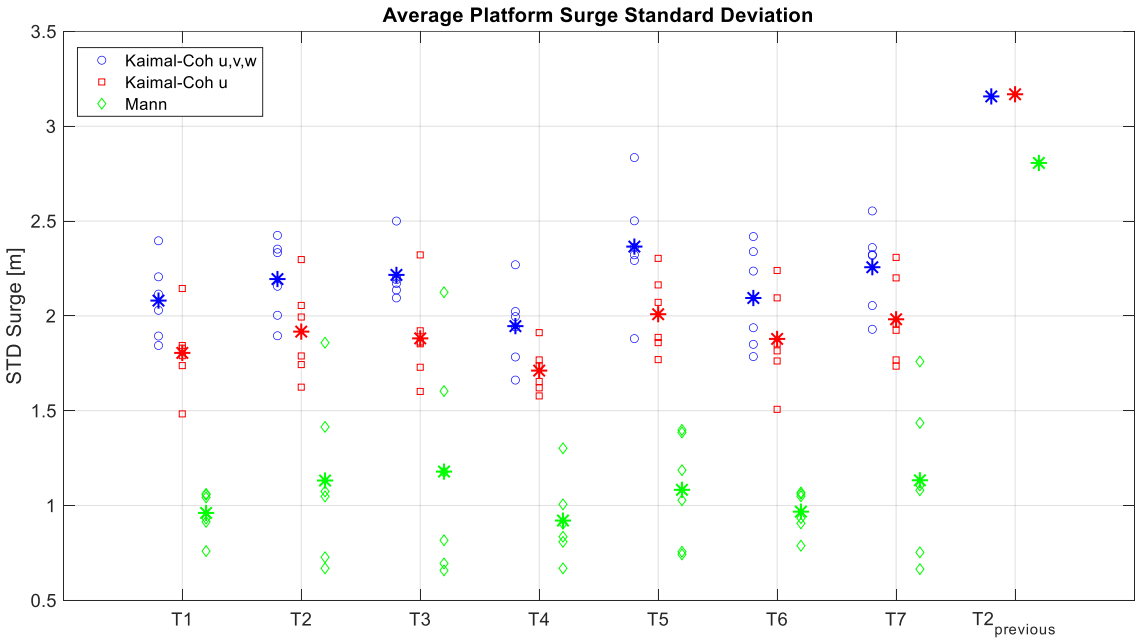

Figure 4.12: Mean platform surge standard deviation for each wind turbine and turbulence case. Each marker represents the value of one simulation except for the asterisk, which represents the average over the six simulation.

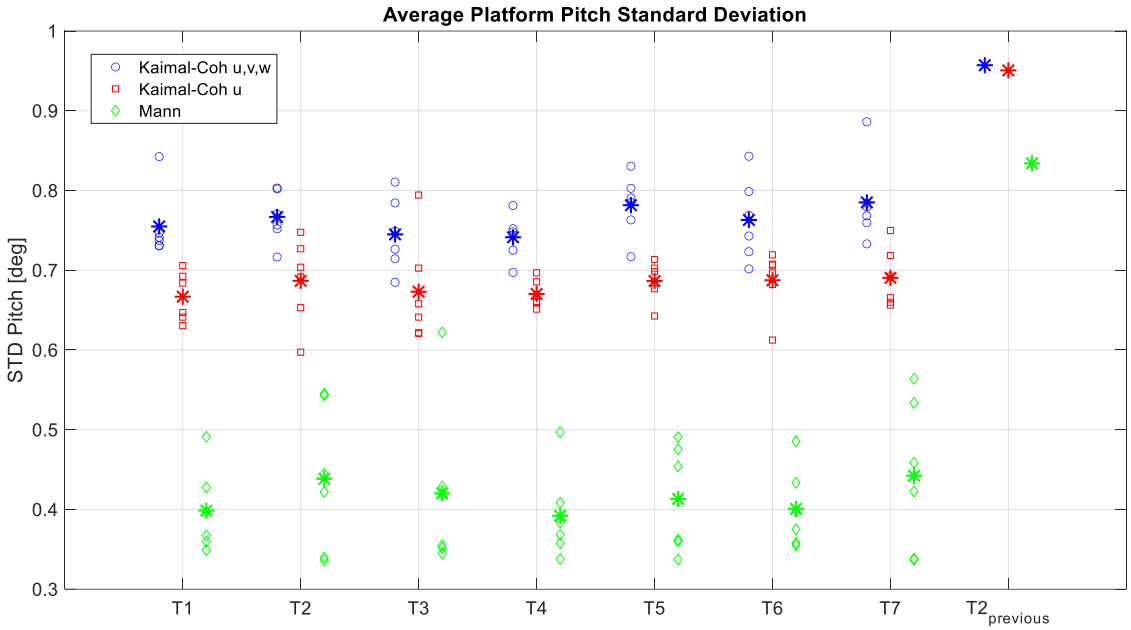

Figure 4.13: Mean platform pitch standard deviation for each wind turbine and turbulence case. Each marker represents the value of one simulation except for the asterisk, which represents the average over the six simulation.

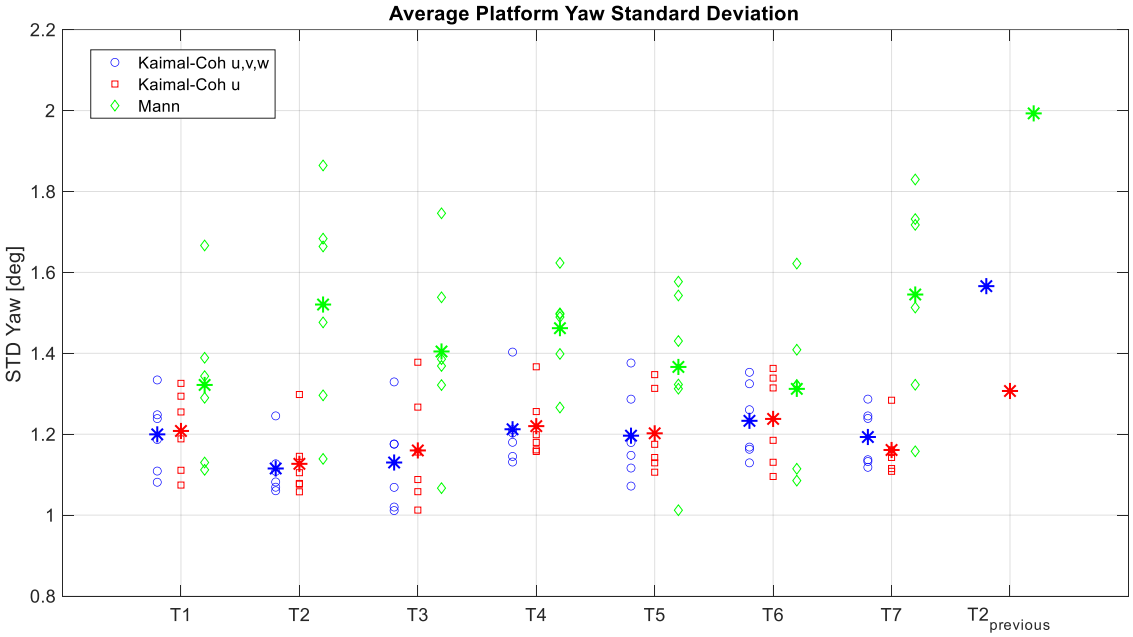

Figure 4.14: Mean platform yaw standard deviation for each wind turbine and turbulence case. Each marker represents the value of one simulation except for the asterisk, which represents the average over the six simulation.

Figure 4.15, Figure 4.16 and Figure 4.17 depict, instead, the PSDs of the platform motions for each turbine and for each turbulence typology.

For all the motions, the low-frequency (0-0.02 Hz) response is always the dominant; this is mainly due to the wake meandering, occurring in this frequency range.

In addition, the peaks for surge, pitch and yaw natural frequency, respectively 0.007 Hz, 0.036 Hz and 0.011 Hz (Section 1.4), can be distinguished in the corresponding figures.

The *Mann* inflow is characterized by a lower PSD for surge and pitch and by a greater one for yaw, with respect to the *Kaimal* spectra, confirming the aforementioned result of the standard deviation figures.

It is also important to note that the motions PSD responses in the 0 Hz -0.02 Hz band are, for all the turbines and turbulence models, similar to the upwind turbines (T1 and T2) and lower than the ones of the two-turbines case downstream turbine ($T2_{previous}$), which reaches peaks of 0.58 m^2/Hz for surge, 0.022 deg^2/Hz for pitch and 0.021 deg^2/Hz for Yaw (Section 3.2.3). This confirms that the 5D staggered seven-turbines layout keeps the platform motions limited.

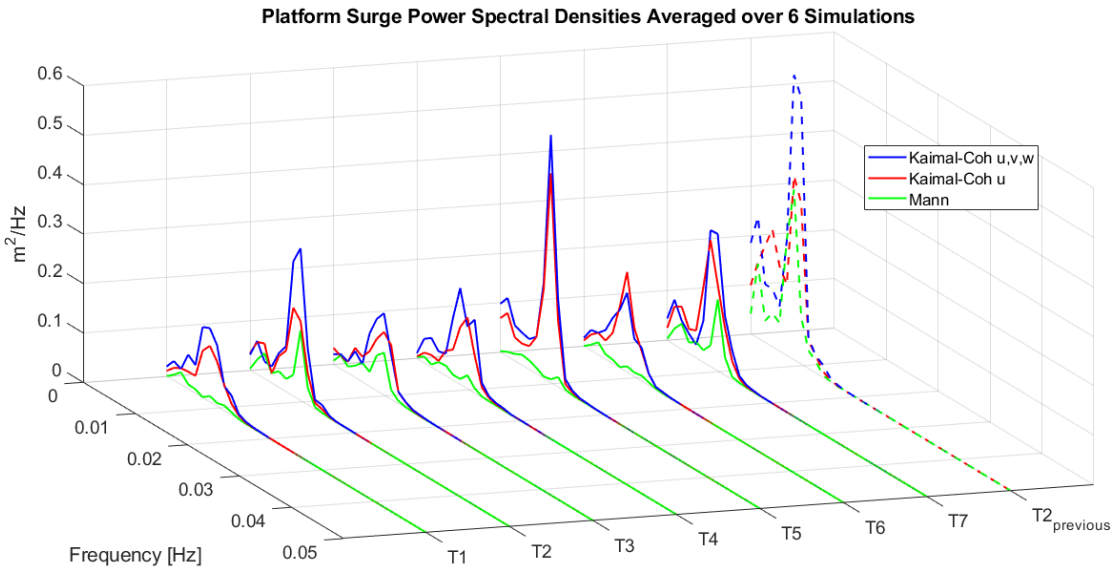

Figure 4.15: Platform surge power spectral density for each wind turbine and turbulence case.

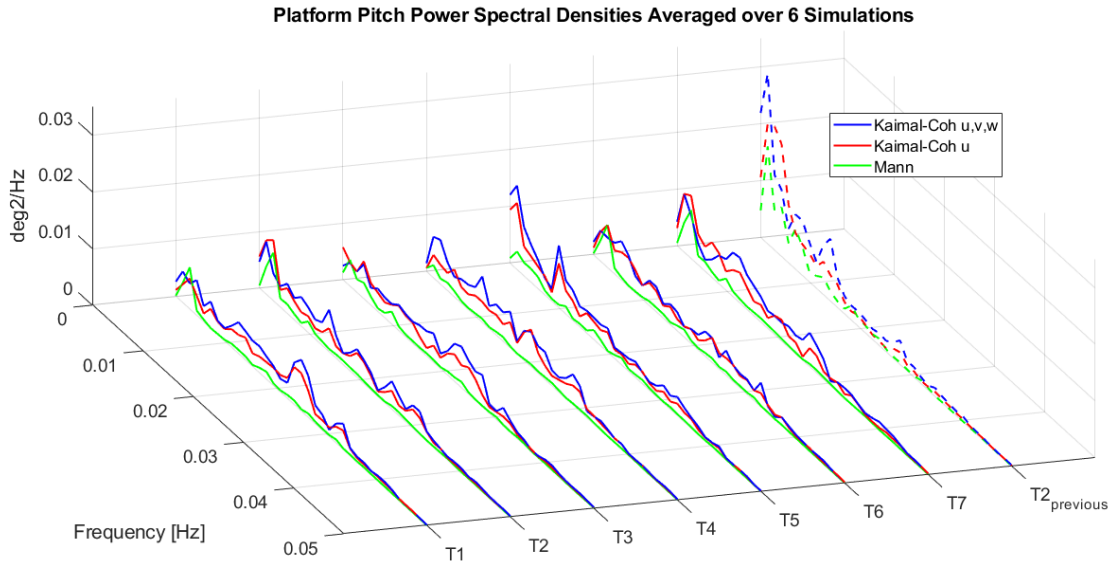

Figure 4.16: Platform pitch power spectral density for each wind turbine and turbulence case.

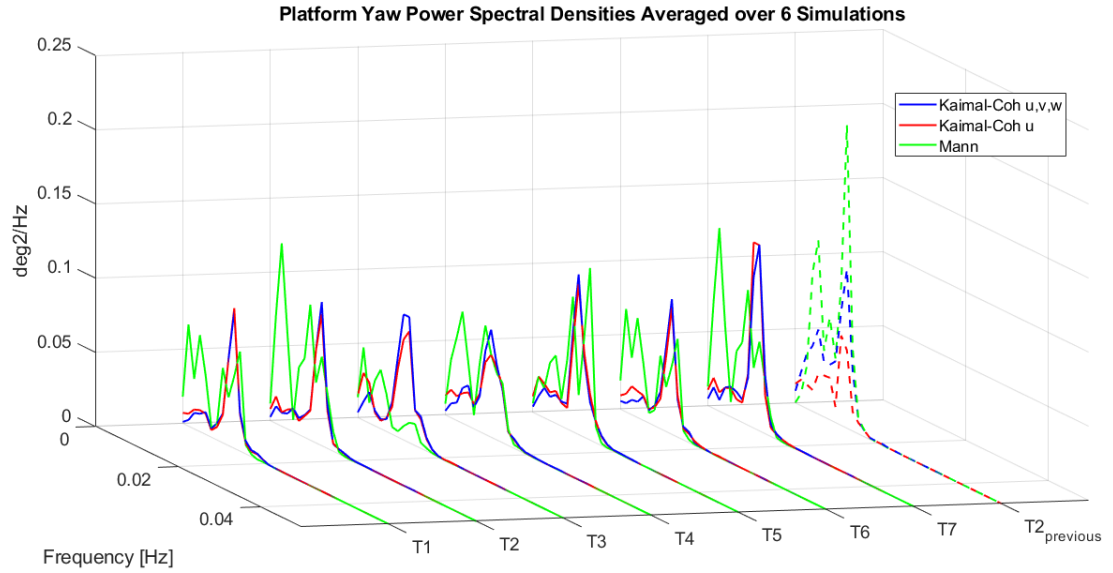

Figure 4.17: Platform pitch power spectral density for each wind turbine and turbulence case.

4.2.4. Axial Stresses

In the next three figures (Figure 4.18, Figure 4.19, Figure 4.20), the power spectral densities of the tower base axial stresses, in the downstream point of the external shell, averaged over the six simulations, are plotted, respectively for the low-, wave- and tower-frequency ranges.

The biggest amount of energy is in the low-frequency range (0-0.06 Hz) (Figure 4.18), the one of the wake meandering. That is easy to note by looking at the ordinates' scales.

In this band of frequencies the highest peaks are obtained for T5 and T7 but the PSDs are almost always lower than the ones of the downstream turbine's tower base in the two-turbines geometry ($T2_{previous}$). In this range the peaks for the platform motions natural frequencies (Section 1.4) are visible, except for the surge-sway one (0.007 Hz), distinguishable, instead, in the wave-frequency range (Figure 4.19).
In the tower frequencies (0.25-0.70 Hz) plot (Figure 4.20), instead, it is possible to note the peaks for the 3P excitation (Table 4.1) and for the tower pitch and bending natural frequencies (Section 1.3). Accordingly with the two-turbines analysis (Section 3.2.4) results and with literature [35] [36], the 3P response is greater with the *Mann* model than for the *Kaimal* cases.

Table 4.1: 3P frequency for each wind turbine and turbulence case.

Turbulence Cases	**T1**	**T2**	**T3**	**T4**	**T5**	**T6**	**T7**	**$T2_{previous}$**
Kaimal-Coh u,v,w	0.351Hz	0.351Hz	0.351Hz	0.352Hz	0.352Hz	0.348Hz	0.347Hz	0.327Hz
Kaimal-Coh u	0.355Hz	0.351Hz	0.351Hz	0.354Hz	0.353Hz	0.348Hz	0.346Hz	0.315Hz
Mann	0.357Hz	0.356Hz	0.356Hz	0.357Hz	0.356Hz	0.347Hz	0.346Hz	0.321Hz

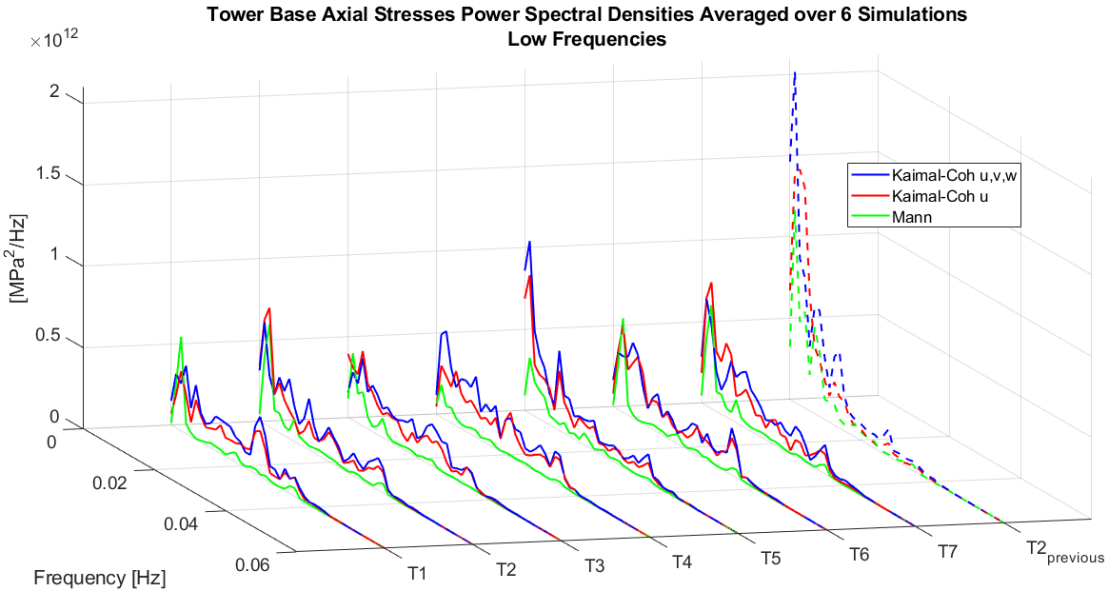

Figure 4.18: Tower base axial stresses power spectral density for each wind turbine and turbulence case, in the low-frequency range.

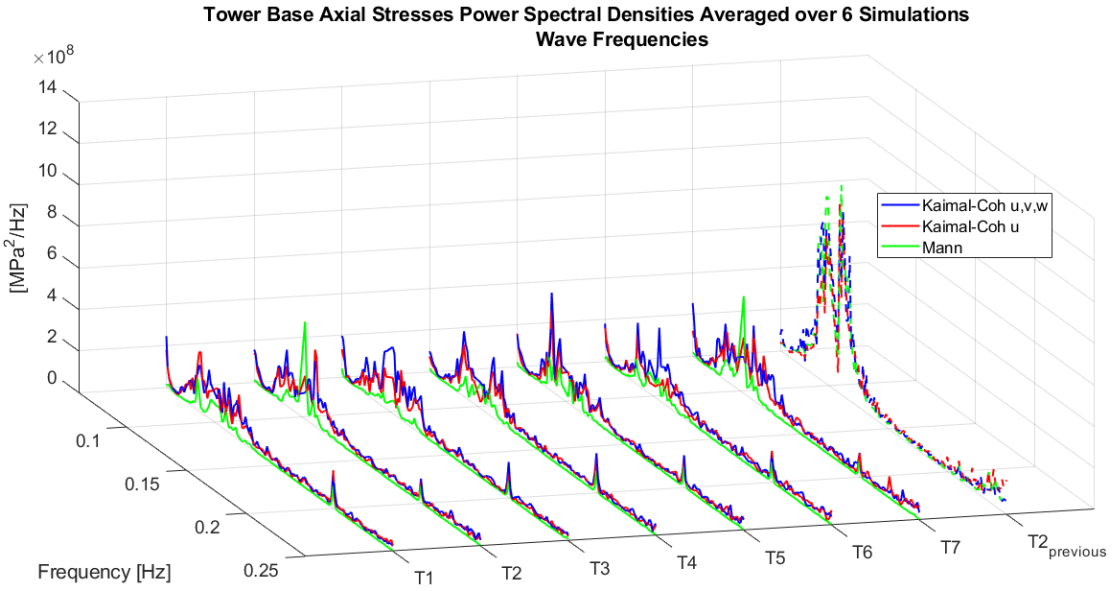

Figure 4.19: Tower base axial stresses power spectral density for each wind turbine and turbulence case, in the wave-frequency range.

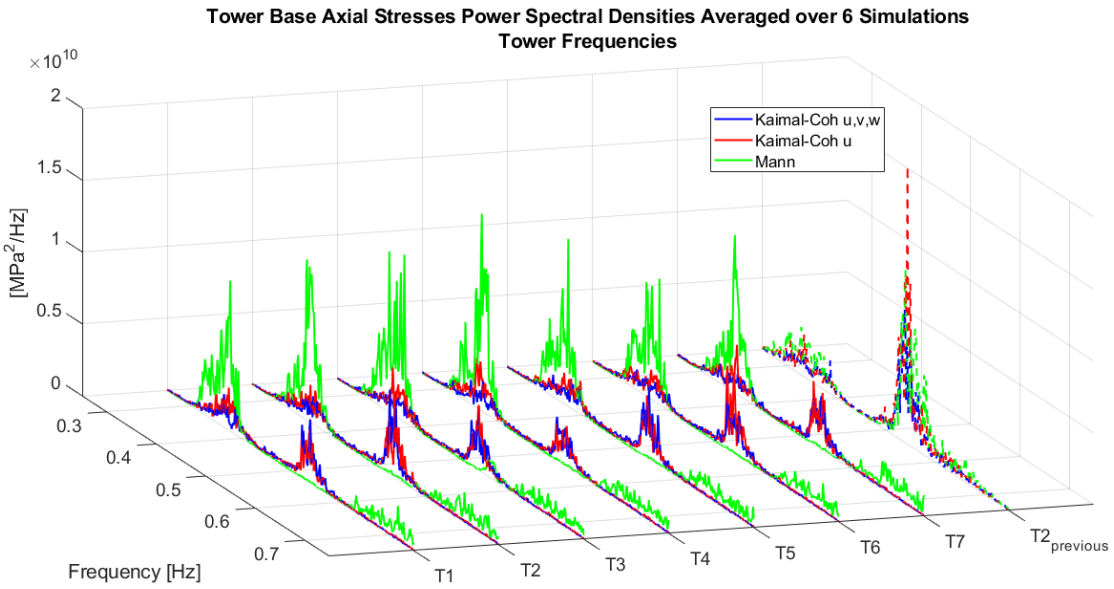

Figure 4.20: Tower base axial stresses power spectral density for each wind turbine and turbulence case, in the tower-frequency range.

Figure 4.21, Figure 4.22 and Figure 4.23, instead, represent the averaged axial stresses power spectral density at the tower top. The first represent the low frequencies (0-0.06 Hz), the second the wave ones (0.06-0.25 Hz) and the last the tower ones (0.25-0.70 Hz).

The responses are about two orders of magnitude higher than at the tower base but, despite that, the same conclusions of the tower base axial stresses PSDs can be made also for the tower top.

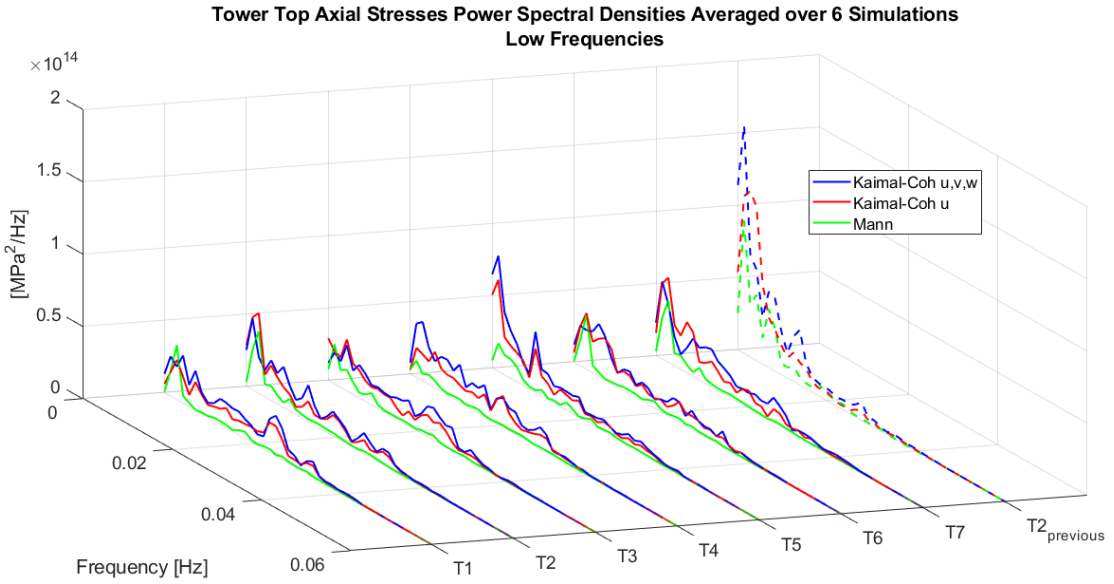

Figure 4.21: Tower top axial stresses power spectral density for each wind turbine and turbulence case, in the low-frequency range.

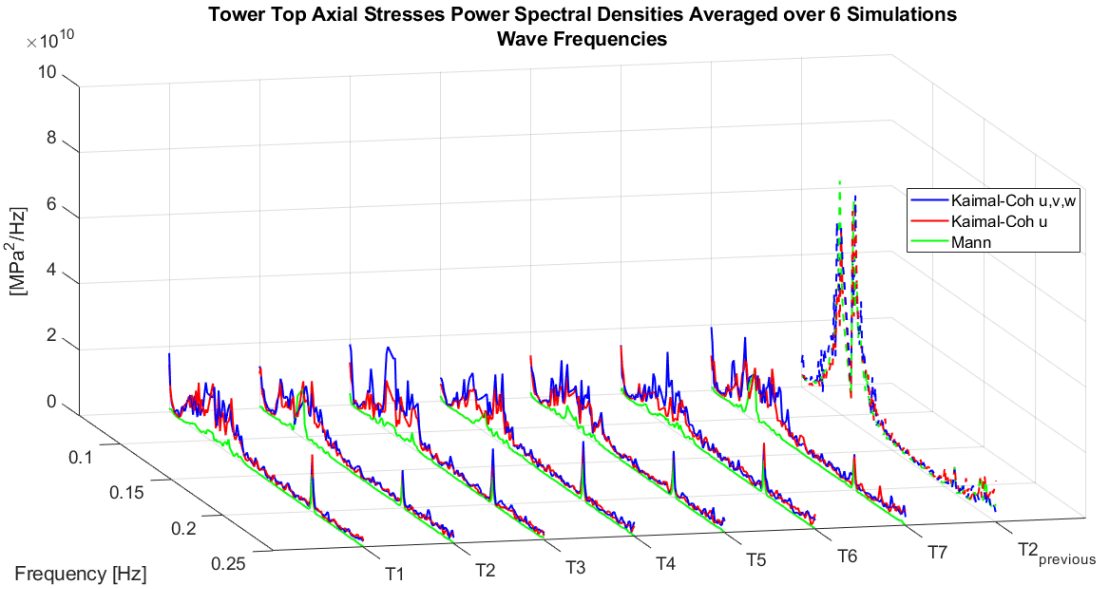

Figure 4.22: Tower top axial stresses power spectral density for each wind turbine and turbulence case, in the wave-frequency range.

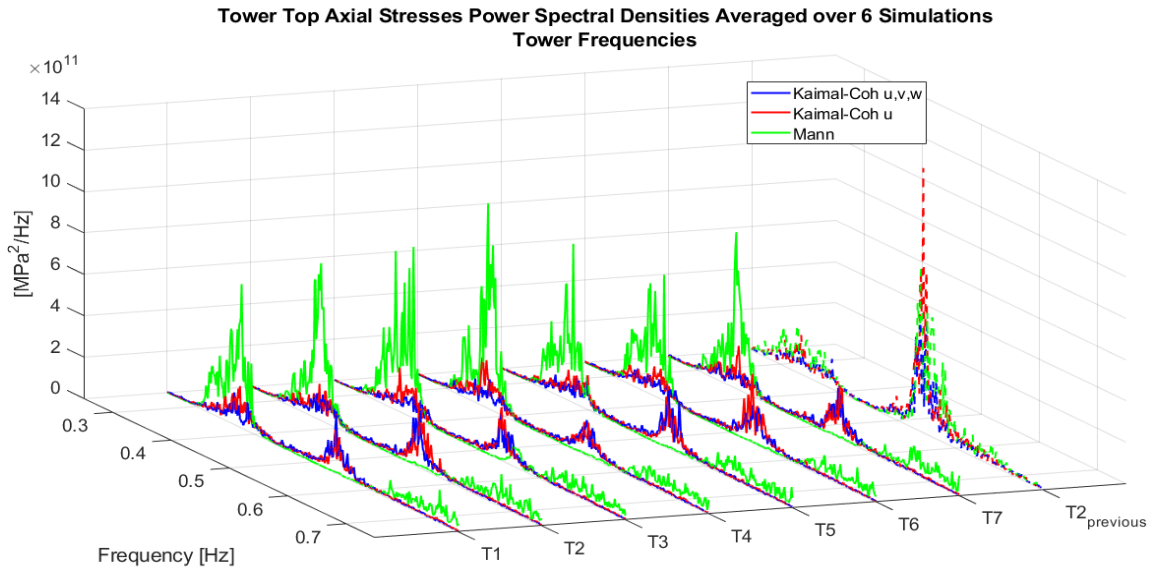

Figure 4.23: Tower top axial stresses power spectral density for each wind turbine and turbulence case, in the tower-frequency range.

Figure 4.24, Figure 4.25 and Figure 4.26 depict the PSDs of axial stresses on the fairlead of the first mooring line (Figure 1.5). Each picture concern one of the aforementioned frequency ranges. In the low-frequency range, (Figure 4.24) the one with the highest energy content, the trends are almost always lower than the ones of the downstream turbine's first mooring line of the two-turbines farm ($T2_{previous}$) (Section 3.2.4). In this band, the greatest responses are obtained with *Kaimal-Coh u, v, w* case, followed by the *Kaimal-Coh u* one, as for the two-turbines case (Section 3.2.4).

In the tower-frequency range (Figure 4.26), the relevant peaks in correspondence of the 3P frequency and at the tower pitch and bending frequencies are visible. Moreover, the rotor torque moment leads to a slight roll offset, making the first mooring line stiffer. For this reason, the first mooring line is always characterized by a higher response in the high-frequency range with respect to the other two mooring lines (Figure 4.29 and Figure 4.32). These tower-frequency band conclusions are in accordance with the ones of the two-turbines layout (Section 3.2.4).

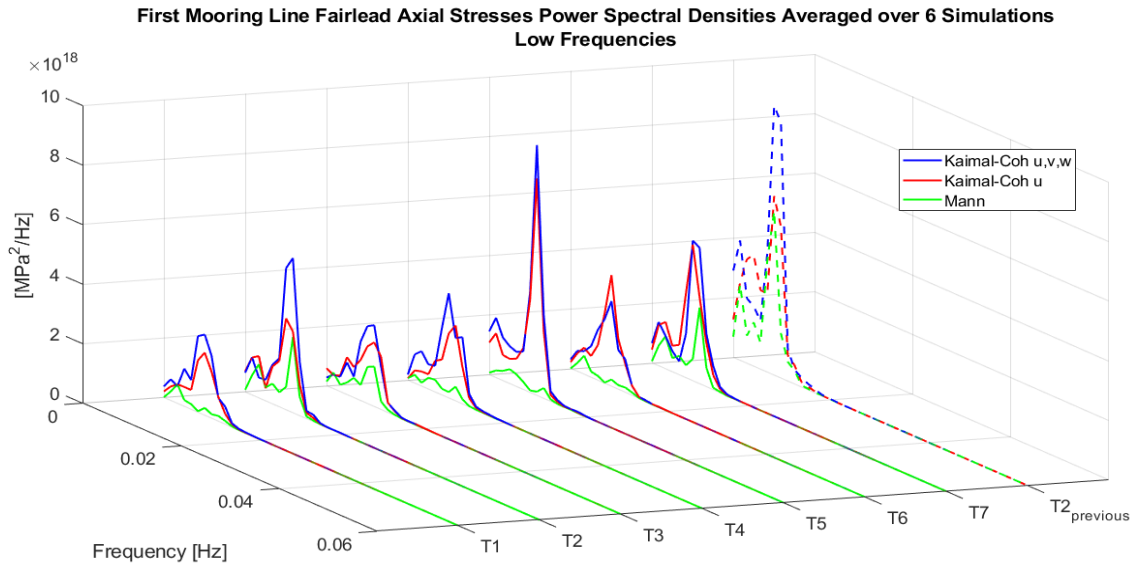

Figure 4.24: Power spectral density of the first mooring line fairlead axial stresses for each wind turbine and turbulence case, in the low-frequency range.

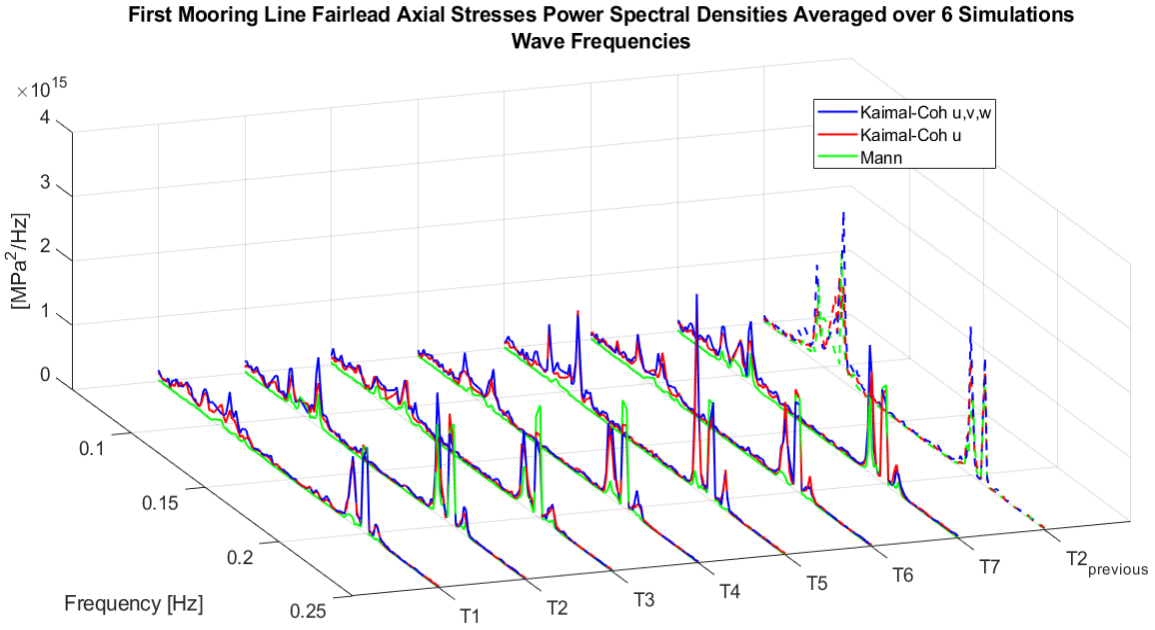

Figure 4.25: Power spectral density of the first mooring line fairlead axial stresses for each wind turbine and turbulence case, in the wave-frequency range.

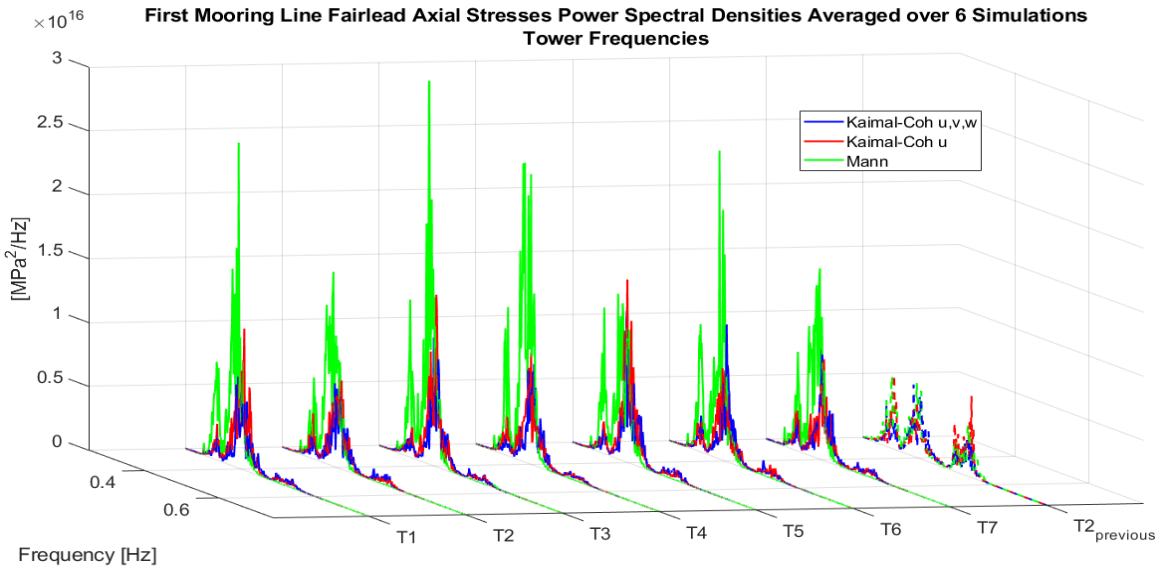

Figure 4.26: Power spectral density of the first mooring line fairlead axial stresses for each wind turbine and turbulence case, in the tower-frequency range.

For what concern the second mooring line axial stresses at the fairlead, PSDs are shown analogously with Figure 4.27, Figure 4.28 and Figure 4.29.

Results are similar to the ones of the first mooring lines. In the low frequency-range (Figure 4.27), the difference is that, when *Mann* inflow is used, the response is higher compared to the one obtained with the *Kaimal* cases, expecially for T3 (Figure 4.2).

In addition, in the high-frequency range (Figure 4.29), the excitation is lower than the first mooring line because of the slight mean roll offset, as mentioned before.

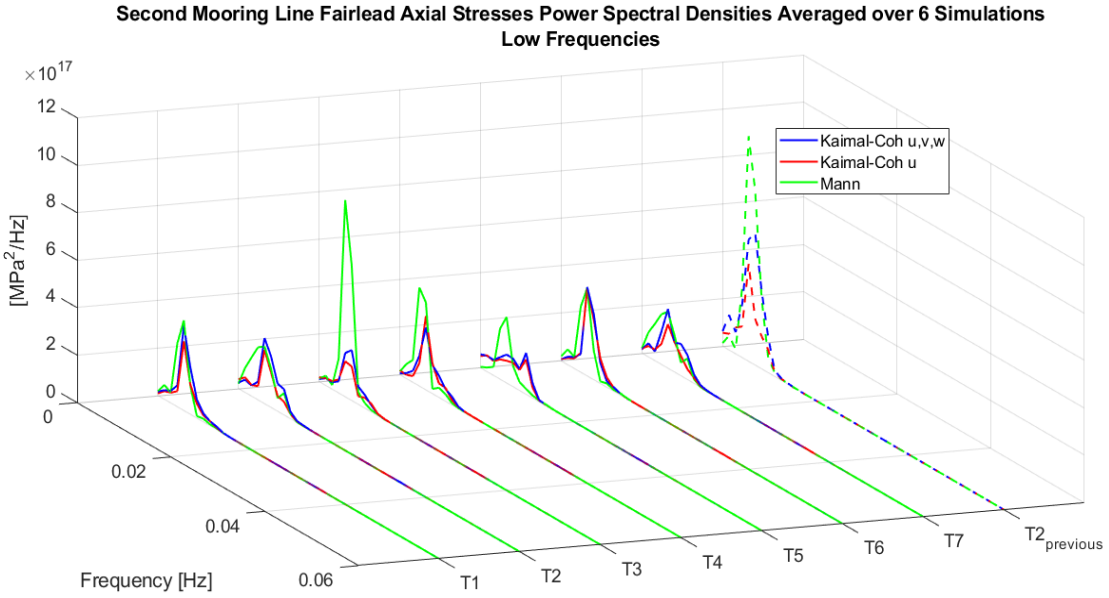

Figure 4.27: Power spectral density of the second mooring line fairlead axial stresses for each wind turbine and turbulence case, in the low-frequency range.

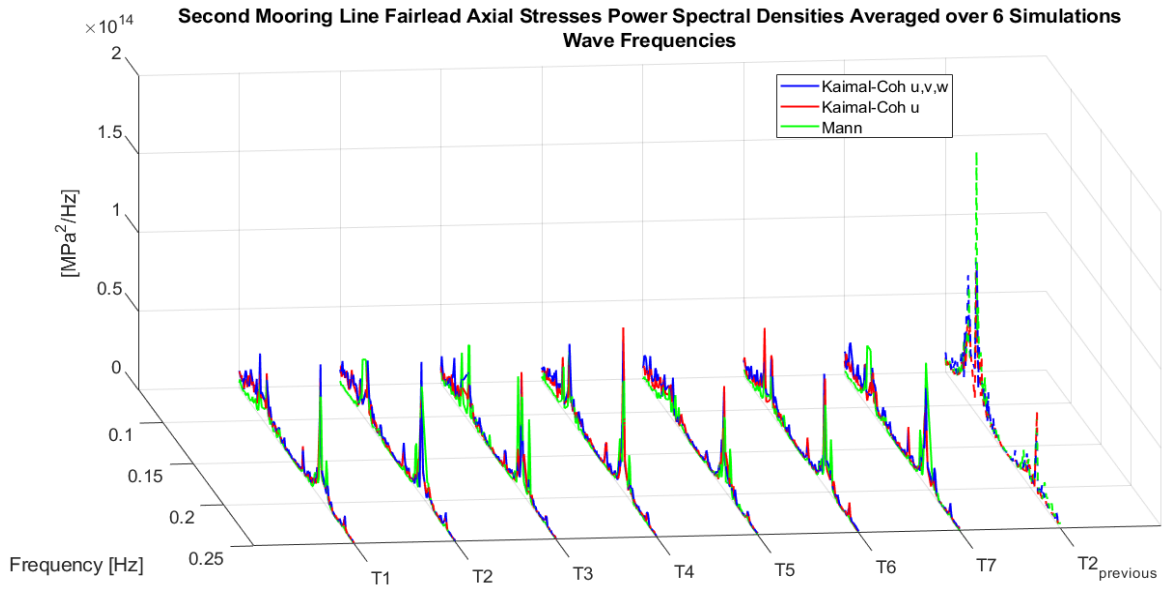

Figure 4.28: Power spectral density of the second mooring line fairlead axial stresses for each wind turbine and turbulence case, in the wave-frequency range.

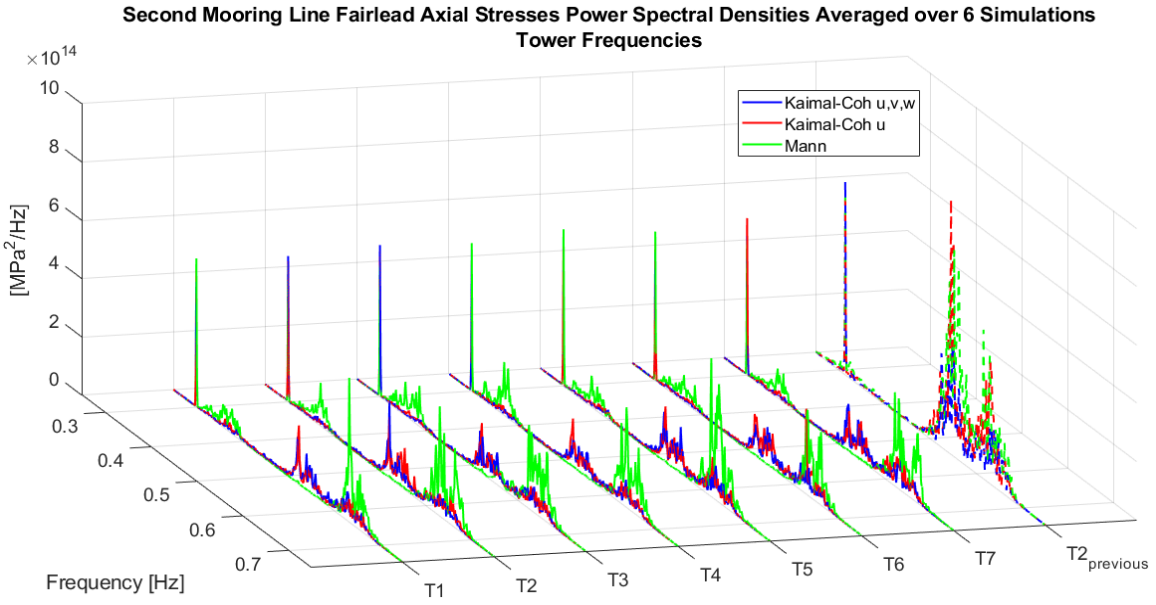

Figure 4.29: Power spectral density of the second mooring line fairlead axial stresses for each wind turbine and turbulence case, in the tower-frequency range.

Considering the third mooring line, the same conclusions of the second mooring line are valid, as shown in Figure 4.30, Figure 4.31 and Figure 4.32.

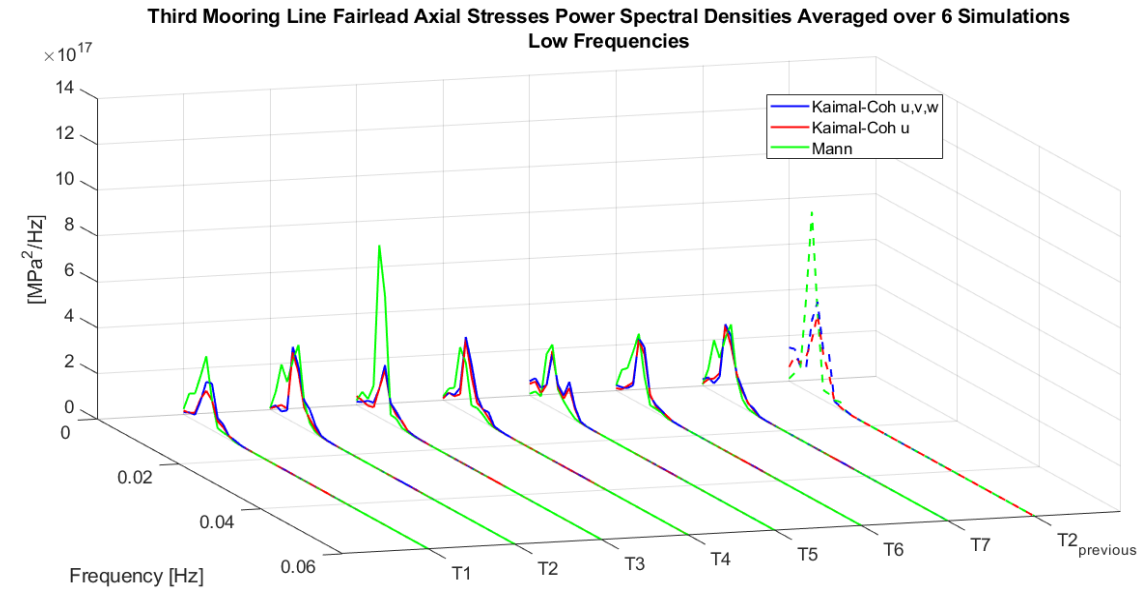

Figure 4.30: Power spectral density of the third mooring line fairlead axial stresses for each wind turbine and turbulence case, in the low-frequency range.

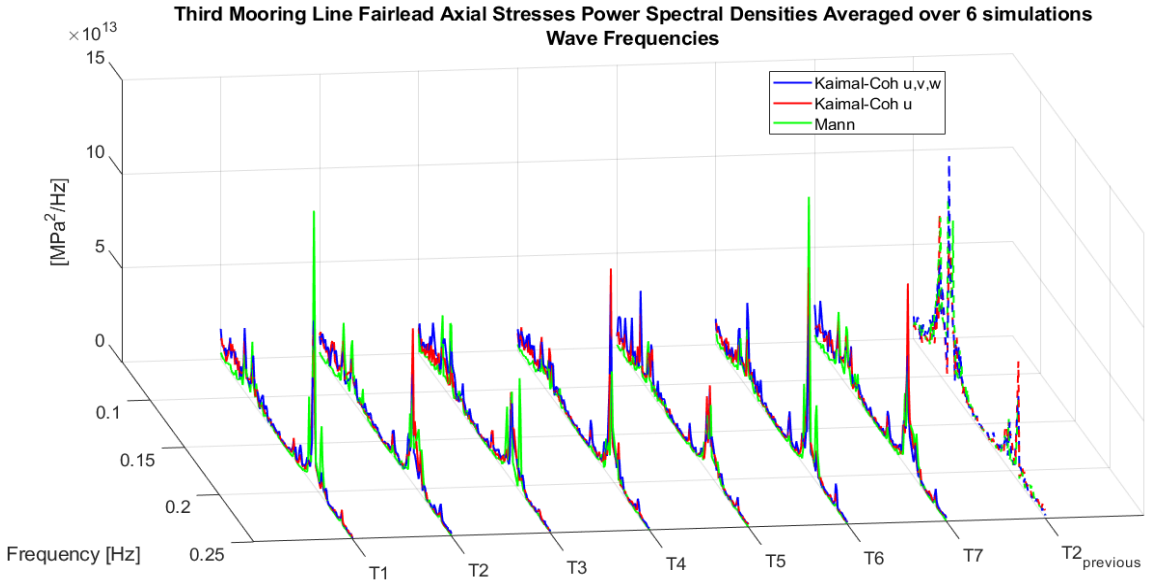

Figure 4.31: Power spectral density of the third mooring line fairlead axial stresses for each wind turbine and turbulence case, in the wave-frequency range.

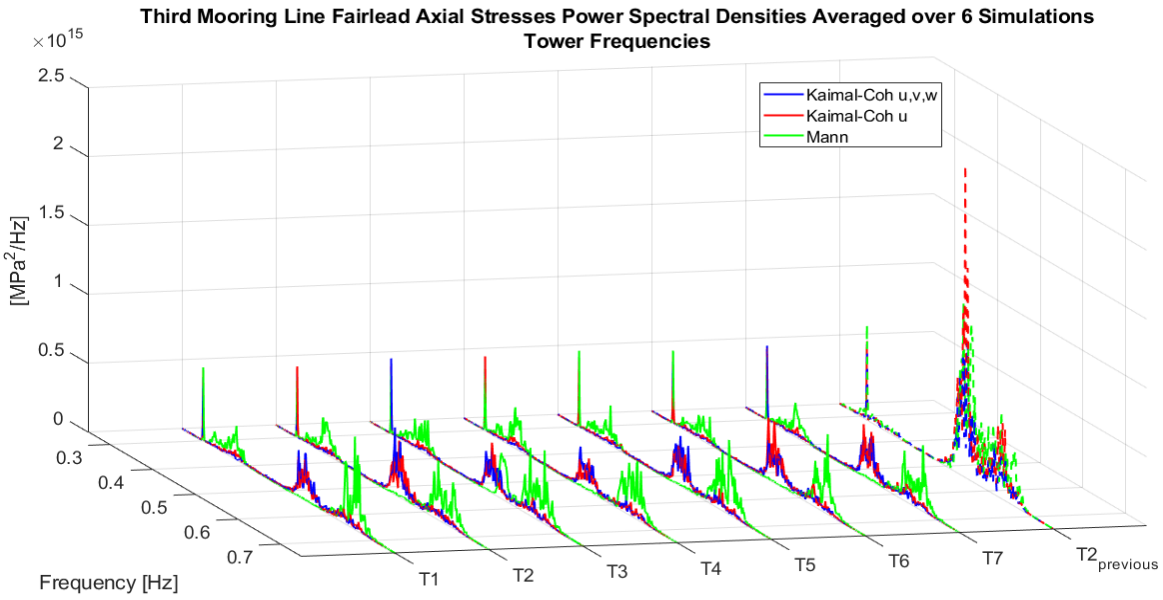

Figure 4.32: Power spectral density of the third mooring line fairlead axial stresses for each wind turbine and turbulence case, in the tower-frequency range.

4.2.5. Fatigue Damages

Figure 4.33 represents the mean 1-h DELs for the combined roll and pitch moments at the tower base and top, showing that they are similar among all the turbines.
For each turbine, with *Kaimal-Coh u, v, w*, *Kaimal-Coh u* and *Mann* the fatigue damages averaged over the six simulations at the tower base are 18.31%-20.48%, 21.59%-22.68% and 26.23%-23.95%, respectively, lower than the ones of the two-turbines case downstream turbine ($T2_{previous}$) (Section 3.2.5).
At the tower top, instead, considering each turbulence case in the same order as above, they are 19.86%-21.6%, 21%-23.36% and 0.4%-5.31% lower (Section 3.2.5).
It is possible hence to conclude that this geometry keeps the tower DELs wake-related increase very limited.

As for the two-turbines case, it is also possible to note that DELs are higher for the tower base than for the top. At the top, moreover, *Mann* damages are significantly greater than the ones obtained with the *Kaimal* inflows; it means that the tower top is more sensitive to the axial stresses 3P frequency responses, which are higher for the *Mann* inflow than in the *Kaimal* cases (Figure 4.23).

As before (Section 3.2.5), the tower axial force fatigue damages have not been shown because they have been found to be much smaller than the moments ones, both for tower base and top.

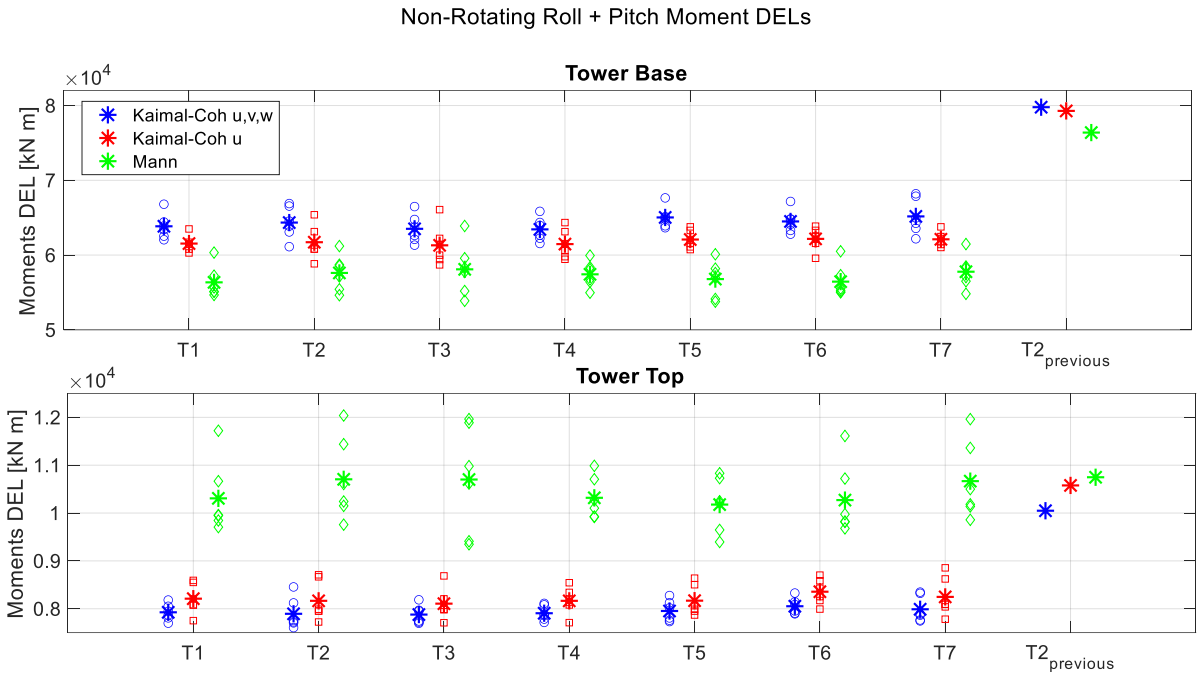

Figure 4.33: Tower base and top short-term DELs for each wind turbine and turbulence case. Each marker represents the mean value of one simulation except for the asterisk, which represents the average over the six simulation.

Considering the mooring system (Figure 4.34), the variations of the averaged fairlead DELs are, for each turbulence case, lower than the ones occurring from the upwind to the downwind turbine in the two-turbines layout ($T2_{previous}$) (Section 3.2.5), for all the mooring lines.

In addition, the values of all the turbines in the current geometry are lower than the ones of the downstream turbine in that case, of:

- 15.03%-26.77% with *Kaimal-Coh u, v, w*, 19.06%-27.94% with *Kaimal-Coh u* and 29.66%-36.76% with *Mann* at the first mooring line fairlead;
- 15.55%-17.52% with *Kaimal-Coh u, v, w*, 14.96%-16.70% with *Kaimal-Coh u* and 14.81%-23.15% with *Mann* at the second mooring line fairlead;
- 14.76%-17.39% with *Kaimal-Coh u, v, w*, 19.90%-18.99% with *Kaimal-Coh u* and 13.01%-23.58% with *Mann* at the third mooring line fairlead;

The response of this seven-turbines arrangement is hence good in terms of DELs even for the mooring lines ones.

As for the two-turbines farm (Section 3.2.5), the first mooring line is the one suffering the highest DELs and their greatest values occur for the *Kaimal-Coh u, v, w* case. In the second and third one, instead, the worst fatigue damages are obtained for the *Mann* turbulence. This is in accordance with the fairleads axial stresses response in the low-

frequency range, which is the one with the highest energy content (Figure 4.24, Figure 4.27, Figure 4.30).

Moreover, in the second and third mooring line, the highest averaged DEL value, obtained for T3 (Figure 4.2) with the *Mann* model, is related to the peak of the *Mann* axial stresses response in the low-frequency range for these mooring lines of T3 (Figure 4.27, Figure 4.30).

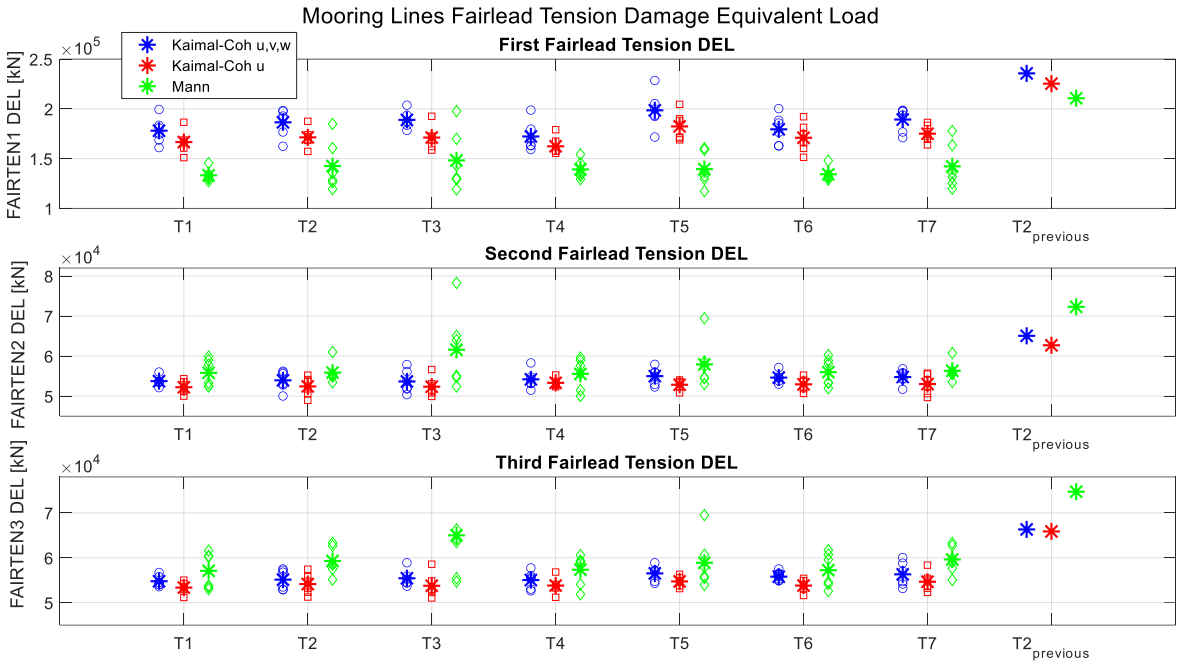

Figure 4.34: Mooring lines short-term DELs for each wind turbine and turbulence case. Each marker represents the mean value of one simulation except for the asterisk, which represents the average over the six simulation.

4.3. Conclusions

As for the two-turbines case, the *Kaimal-Coh u, v, w* spectrum is the one with the highest and most low-frequency lateral meandering, while the *Mann* turbulence is characterized by stretched coherence structures influencing the farm response.

Anyway, the wake meandering behaviour is a low frequencies (0-0.02 Hz) phenomenon and, in a farm layout of this type, it is randomized and characterized by relevant uncertainty.

The horizontal wind velocity "felt" at the hubs is close to the reference one (10 m/s) for all the turbines and turbulence cases. The biggest reductions are obtained for the most downwind turbines (T6 and T7) in the *Kaimal-Coh u* case, but they are anyway limited: for 2.31% for T6 and 3.47% for T7.

The hub turbulence intensity assumes reasonable values for all the turbines and models, considering such a location, and small deviations among them: the 6-simulation averaged values are included between 10.5% and about 14%.

TI is, however, characterized by high uncertainties, which reach even the value of $\pm$ 28.64% with the Mann spectrum. This is probably due to the randomization of the flow field for a farm of this level of complexity.

For concern the platform motions, the surge standard deviation is included among 0.92 m and 2.37 m for each turbine and inflow type, the one of pitch is between 0.39° and 0.79° and the yaw one is in the range 1.12°-1.55°. For the downstream turbine of the two-turbine geometry they are instead bigger: the surge, pitch and yaw averaged values ranges are, respectively: 2.81m-3.17m, 0.83°-0.96° and 1.31°-1.99° .

The platform motions PSDs is lower too, compared with two-turbine case downwind turbine. Anyway, the low-frequency response, characteristic of wake meandering, is always the dominant one and both the standard deviations and PSDs are with the *Mann* model are the highest for surge and pitch and the lowest for yaw, due to the coherent structures organization. The peaks for the motions natural frequencies are visible too in the response.

Considering the axial stresses, the mooring lines are always subjected to higher stresses at the fairlead comparing to the tower top and base downstream point and the first line is the worst in these terms. Tower top, instead, endures bigger stresses than tower base.

In any case, the biggest amount of energy is in the low-frequency range. Peaks at the 3P, especially for *Mann*, and tower pitch and bending natural frequencies are however well visible and influence the fatigue damages.
Tower top is more sensible to the 3P excitation with respect to tower base, from the DELs point of view. In the first case, infact, Mann inflow leads to the biggest DELs for all the turbines. Tower base DELs are anyway bigger than the top ones and also of the mooring lines ones.

Among the mooring lines, the first has the biggest fatigue damages and the present the worst case for the *kaimal-Coh u,v,w* model. The other two reach the highest DELs with *Mann* for each turbine. This reflects the low-frequency behaviour of the axial stresses mooring system axial stresses.

Analysed DELs averaged values are similar among the turbines and, with respect to the ones characterizing the downstream turbine in the two-turbines analysis, they are:

- 18.31%-26.23% lower at the tower base;
- 19.86%-23.36% lower for the *Kaimal* models and 0.4%-5.31% lower for *Mann* at the tower top;

- 15.03%-27.94% lower with *Kaimal-Coh u* and 29.66%-36.76% lower with *Mann* at the first mooring line fairlead;
- 14.81%-23.15% lower at the second mooring line fairlead;
- 13.01%-23.58% lower at the third mooring line fairlead.

In conclusion, the analysed seven-turbines hexagonal arrangement, keeps the horizontal hub-wind velocity reduction from the reference one limited and the TI around reasonable values for the considered site. The platform motions and the short-term fatigue damages at the tower base and top and at the mooring lines fairlead are maintained relatively contained too.

In addition, the results obtained in the two-turbines study, concerning the effect of the different turbulence models on the farm response, are confirmed.

5 Seven-Turbines Layout Floating and Monopile Comparison

The final step of this work consists in a comparison among the floating arrangement and a monopile farm with the same hexagonal seven-turbines layout (Figure 4.2).

The analysis inspires always to the A. Wise and E. E. Bachynski wakes study [29] and the considered turbine model is the IEA 15-MW Floating Offshore Wind Turbine (Chapter 1), adapted to simulate the monopile case.

This juxtaposition permits to evidence additional conclusions, indispensable to correctly interpret the response of this configuration.

5.1. Methodology

The methodology is similar to the previous section one (4.1), always inspired to the A. Wise and E. E. Bachynski analysis [29].

The monopile model, for each turbines, has been obtained from the IEA 15-MW Floating Offshore Wind Turbine (Chapter 1): the platform has been completely fixed within the FAST.Farm simulations, preventing any of its motions. Blades, tower, rotor nacelle assembly and control dynamic have been maintained unchanged with respect to the floating case, while the substructure and the transition piece have been not modelled. The monopile turbine, with also the not considered parts and a water depth different by the one assumed, is visible in Figure 5.1 [8].

The same seven-turbines hexagonal layout (Figure 4.2) and FAST.Farm set-up for what concerns the low- and high-resolution domains (Figure 4.3) and wake-dynamics grid have been considered (Section 4.1.1).

Analogous environmental conditions and location have been assumed too (Section 4.1.2). The water depth has been maintained to 200 m, even if it is unrealistic for a monopile wind power plant, since the substructures have been not considered.

For both floating and monopile case, the *Kaimal-Coh u,v,w* (3.1.4) inflow, the one characterized by more meandering among the analysed spectra, have been considered, with the same discretization of the previous analysis (4.1.4). Six different inflow fields, each encompassing the entire farm, have been generated by changing the casual seed,

and for each of them one FAST.Farm simulation of 3600s, excluding pre-simulation (Section 4.1.3), for the floating case and one for the monopile case have been run.

Twelve simulations has been launched in total, six for the floating farm and six for the monopile one.

Axial stresses and DELs have been calculated in the same way (Sections 3.2.4 and 3.2.5) at the external downstream (with respect to the wind inflow) point of the tower base and top cross section (Figure 3.6).

In addition with respect to the previous analyses, the power coefficient values and the plant generator power time history, both outputted by FAST.Farm, have been shown.

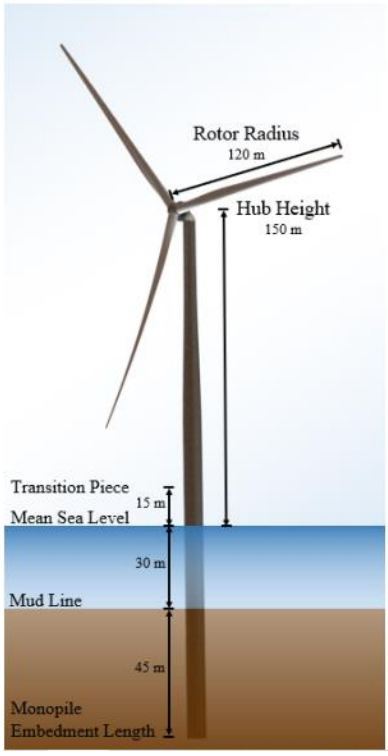

Figure 5.1: The IEA Wind 15-MW monopile reference wind turbine.

5.2. Results

5.2.1. Flow Visualization and Wakes Centre

Figure 5.2 provides an instantaneous hub-height flow field colormap in the low-resolution domain x-y plane, for the last instant of the first simulation (*Kaimal-Coh u,v,w*) for the floating and the monopile case respectively.

It is possible to note that the flow-field part just before T1, T2, T3, T4 and T5 (Figure 5.2) in x-direction, is equal for both the two farm typologies. It means that the hubs of

these rotors "feel" the undisturbed turbulent flow, without suffer the other turbines' wakes; the horizontal wind velocity inhomogeneities present in these zones, visible also in the colormaps, are due to the randomization of the turbulence inflow and not to the wakes of the near turbines. It means that the hubs of these turbines "feel" the undisturbed turbulent flow, without suffer the other turbines' wakes.
The most downwind rotors (T6 and T7, Figure 4.2), instead, are interested at their hubs by the merged wakes of the more upwind turbines.
This conclusion is also confirmed in the next Section (5.2.2).

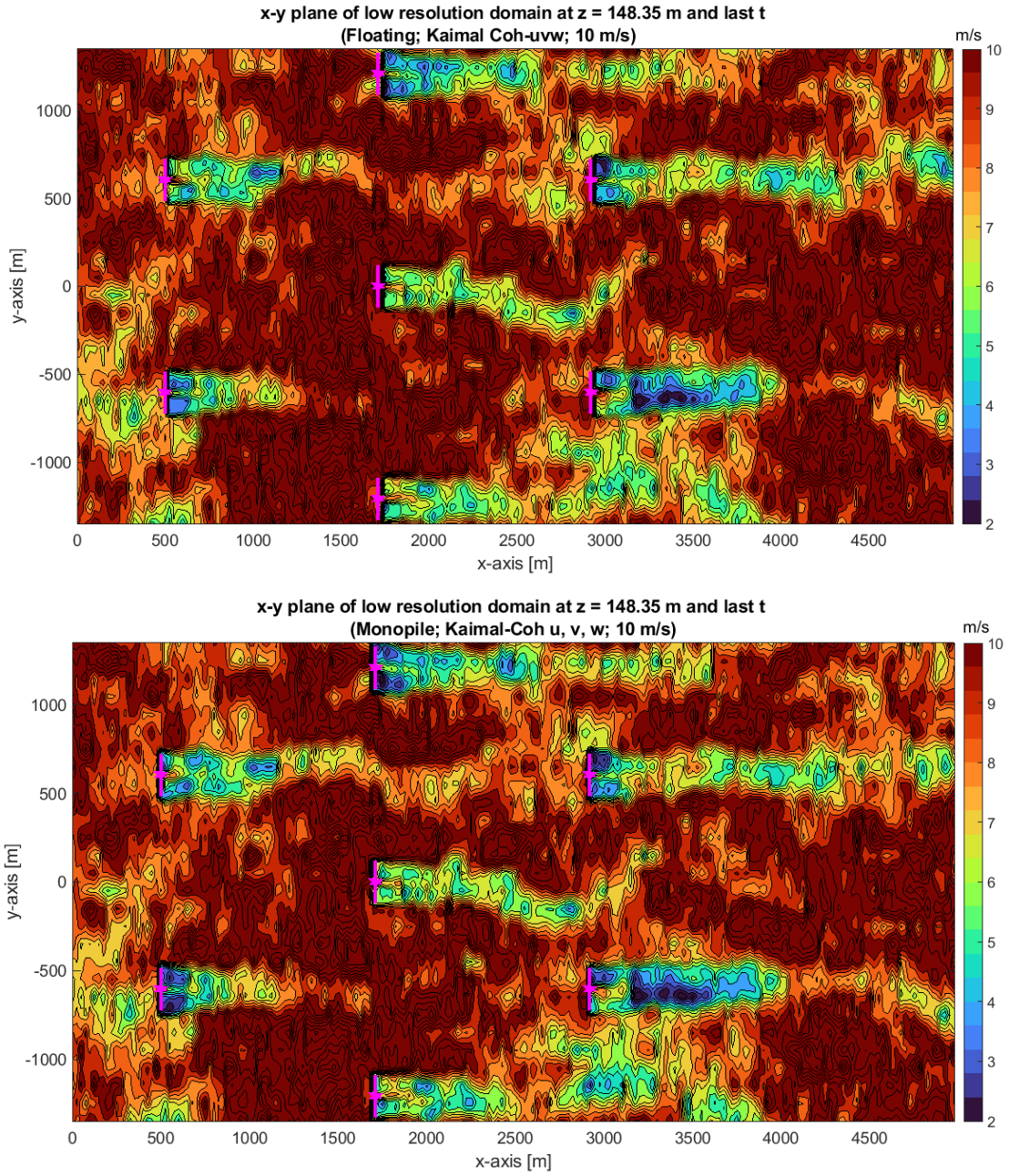

Figure 5.2: Instantaneous (last simulation instant) *Kaimal-Coh u, v, w* wind flow field for the first simulation of the floating (top) and monopile (bottom) farm in the low-resolution domain. Rotors are represented in magenta.

Figure 5.3 depicts, instead, the instantaneous wake centre positions in the low-resolution domain x-y plane normalized on the turbines' diameter at the hub height, for the last instant of the first simulation for both cases. From this figure and from the colormaps (Figure 5.2) it is possible to distinguish wakes merging and defections and the differences in the meandering among the two farm typologies, but it is not possible to quantify them, even because one instant is not enough to generalize the results.

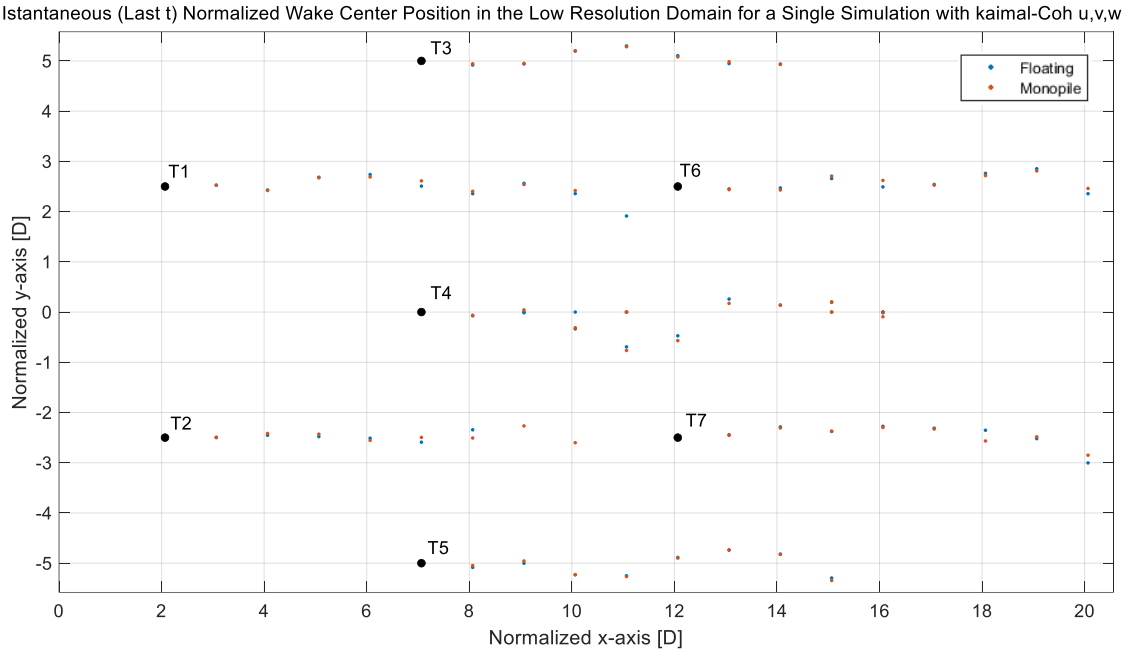

Figure 5.3: Instantaneous (last simulation instant) wake center position till 9D for the first *Kaimal-Coh u,v,w* simulation for the floating and monopile farm in the normalized low-resolution domain. Rotors are represented in black.

For this reason, Figure 5.4 has been introduced. It represents the wake centre lateral (y) position standard deviation at 5D for each simulation and its average value over the six realizations, for all the turbines and for both floating and monopile layout.

The averaged STD in the floating case is always 9.90%-16.01% greater than the monopile farm and the first case is also characterized by more uncertainty (max ±34.86% against a max of ±20.22% for the monopile, both for T3).

It is possible hence to conclude that in the monopile case all the turbines' wakes are characterized by less lateral meandering with respect to the floating plant.

The greatest averaged values occur for T3 and T5 for both the typologies. They are hence, for sure, not related to the platform motions, but rather their dependency from the inflow randomization and wakes deflections and merging as explained in Section 4.2.1, is confirmed.

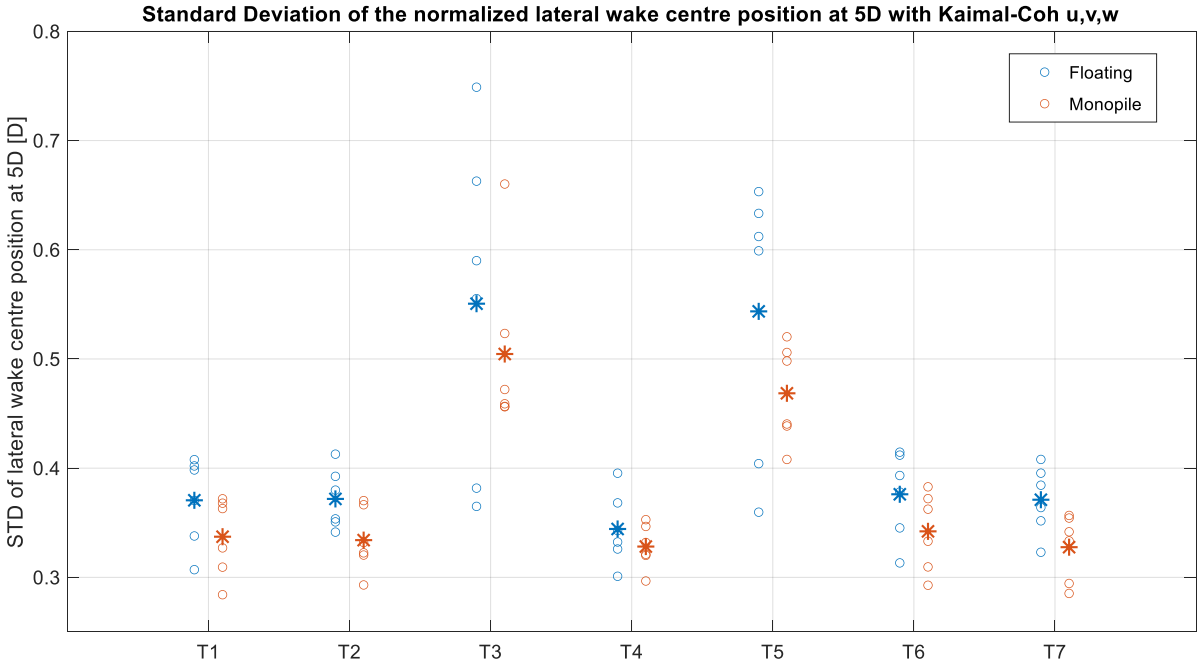

Figure 5.4: Standard deviation of lateral wake center position at 5D downstream from each wind turbine and for both the floating and monopile case with *Kaimal-Coh u, v, w* turbulence. Each marker represents the value of one simulation except for the asterisk, which represents the average over the six simulation.

In Figure 5.5, the power spectral density of the 5D lateral wake meandering for each turbine and support typology configuration is depicted. The vast majority of energy content is concentred in the 0-0.02 Hz frequency range, for all the turbines and farms, but sometimes also components at higher frequencies are present, as expected from the previous analyses (Section 3.2.1, Section 4.2.1) and the Wise and Bachynski study [29].

The monopile wake meandering responses are generally lower then the floating ones, for all the turbines, confirming that the monopile plant is characterized by less wake meandering.

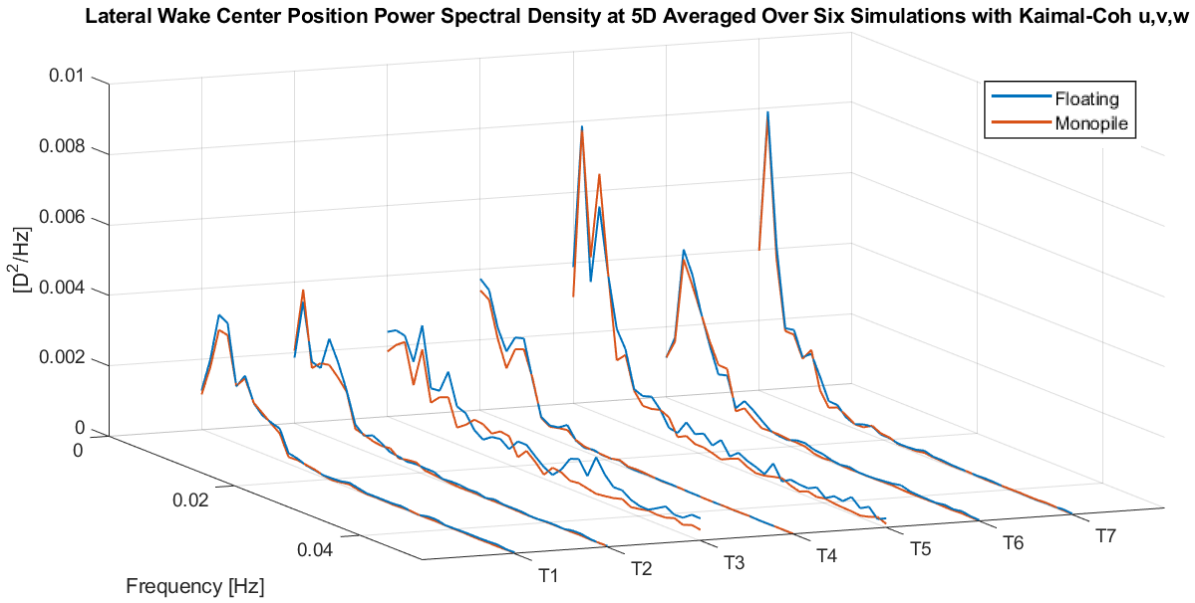

Figure 5.5: Lateral wake center position power spectral density for each wind turbine and support typology configuration with *Kaimal-Coh u, v, w* turbulence.

5.2.2. Wind Velocity and Turbulence Intensity at the Hubs

The mean horizontal wind velocity and turbulence intensity (TI) at the hubs (Figure 5.6 and Figure 5.7, respectively), are identical among the floating and monopile case, considering each of the first five turbines (T1, T2, T3, T4 and T5), for all the simulations. It is a confirmation of the fact that these turbines, at the hubs, "feels" the undisturbed turbulent inflow and are not hit by the wakes.

For these turbines the six-simulations averaged hub mean horizontal wind velocity are close to the reference one (10 m/s). The very contained deviations, both increases and reductions, are caused by the flow field inhomogeneities due to the randomization of the turbulence generation. This is also the cause of the difference in the TI among these five undisturbed rotors.

The most downwind turbines (T6 and T7), are, instead, influenced at the hub by the wakes of the more upwind rotors.

For them, infact, the averaged mean hub wind speed shows bigger reductions, but anyway contained, from 10m/s, with respect to the undisturbed turbines: for the floating case they are 1.86% for T6 and 2.37% for T7, while for the monopile they are respectively 1.98% and 2.66%.

The wind velocity values for these two rotors are slightly lower for the monopile case. This farm typology is, in fact, characterized by less meandering (Section 5.2.1 compared to the floating one and so the downstream turbines (T6 and T7), affected at

hubs mainly by the first five turbines' wakes, operate in a more persistent waked condition.

For what concern the T6 and T7's averaged TI, it is lower too for the monopile case (of 2.76% and 2.49% respectively) compared to the floating one. On the contrary, by considering just the fact that these turbines are more persistently waked in the monopile farm, an increase of their averaged hub TI with respect to the floating plant was expected. Obtaining, instead, a reduction indicates that TI is related to the platform motions and decreases with their fixity.

Is also important to note, as mentioned before (Section 4.2.2), that TI is characterized by an important uncertainty.

Anyway, since the values of the reductions from the reference velocity are very small, and that the TI values are always reasonable for such a site, it is possible to conclude that this layout keeps the wakes influence on the "felt" hub wind velocity and TI, affecting just T6 and T7, very limited.

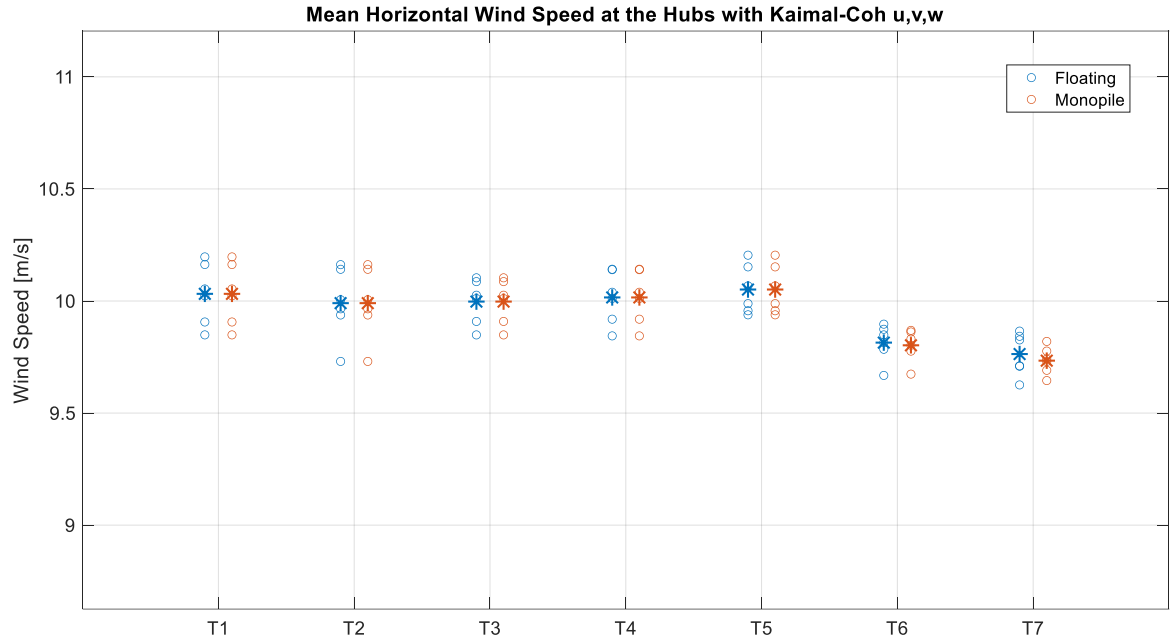

Figure 5.6: Hub wind speed for each wind turbine and farm typology with *Kaimal-Coh u, v, w* turbulence. Each marker represents the mean value of one simulation except for the asterisk, which represents the average over the six simulation.

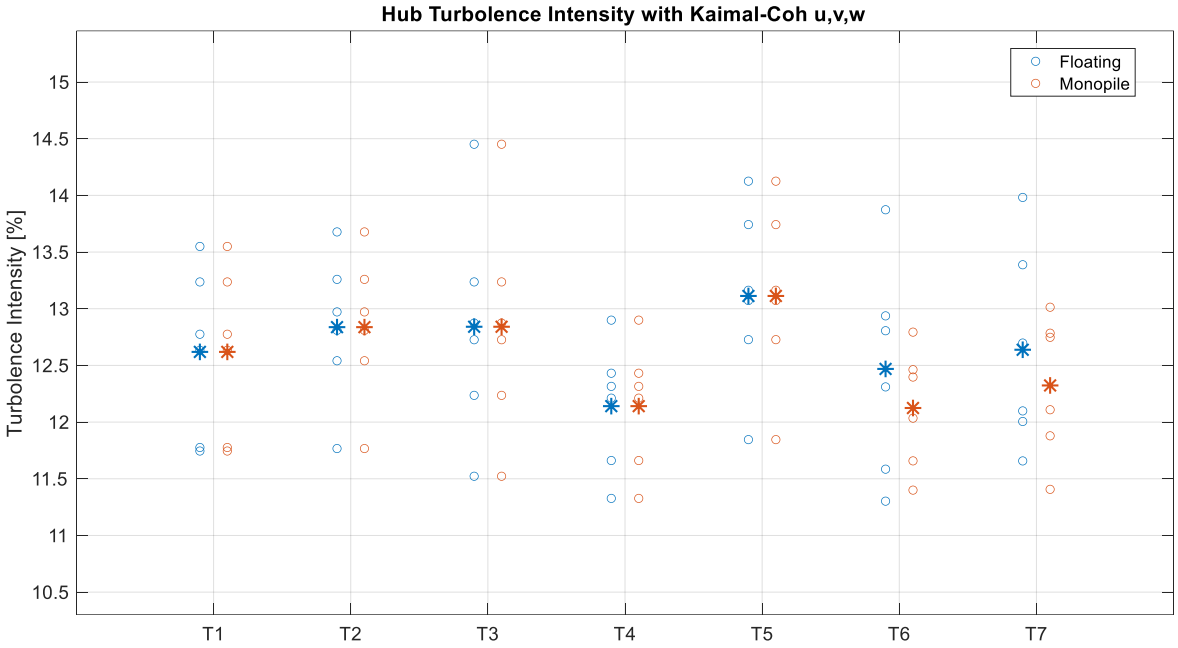

Figure 5.7: Hub turbulence intensity for each wind turbine and farm typology with *Kaimal-Coh u, v, w* turbulence. Each marker represents the mean value of one simulation except for the asterisk, which represents the average over the six simulation.

5.2.3. Axial Stresses

Figure 5.8, Figure 5.9 and Figure 5.10, show the power spectral density of the low, wave and tower frequencies axial stresses, in the downstream point of the tower base external shell, averaged over the six simulations.

In the low-frequency range (0-0.06 Hz, Figure 5.8), the one containing the biggest amount of energy, the axial stresses PSD is always higher for the floating turbines. In this case the peaks in correspondence of the platform yaw, roll pitch and heave natural frequencies (Section 1.4) are visible, while they are not in the monopile case. That is an evidence of the negative influence of the platform DOF on the tower base axial stresses.

For both the farm typologies, the biggest low frequency stresses at the bottom of the tower occurs for T5.

A peak around 0.1 Hz, due to the waves, is instead dominant in the dominant one in the wave-frequency range (0.06 Hz-0.25 Hz, Figure 5.9) for the floating case.
The axial stresses PSDs pictures in this frequency range (even for tower top, Figure 5.12) have not been brushed for clarity, differently from the previous analysis.

In the tower frequencies (0.25-0.70 Hz, Figure 5.10), instead, it is possible to distinguish the 3P (Table 5.1) and tower pitch and bending natural frequencies excitations (Section 1.3).

The 3P response is much bigger for the monopile case, for which it melts with the tower natural frequencies peaks.

Table 5.1: 3P frequency for the floating and monopile case for each wind turbine with Kaimal-Coh u, v, w.

Farm Typologies	**T1**	**T2**	**T3**	**T4**	**T5**	**T6**	**T7**
Floating	0.351Hz	0.351Hz	0.351Hz	0.352Hz	0.352Hz	0.348Hz	0.347Hz
Monopile	0.359Hz	0.359Hz	0.358Hz	0.360Hz	0.360Hz	0.354Hz	0.353Hz

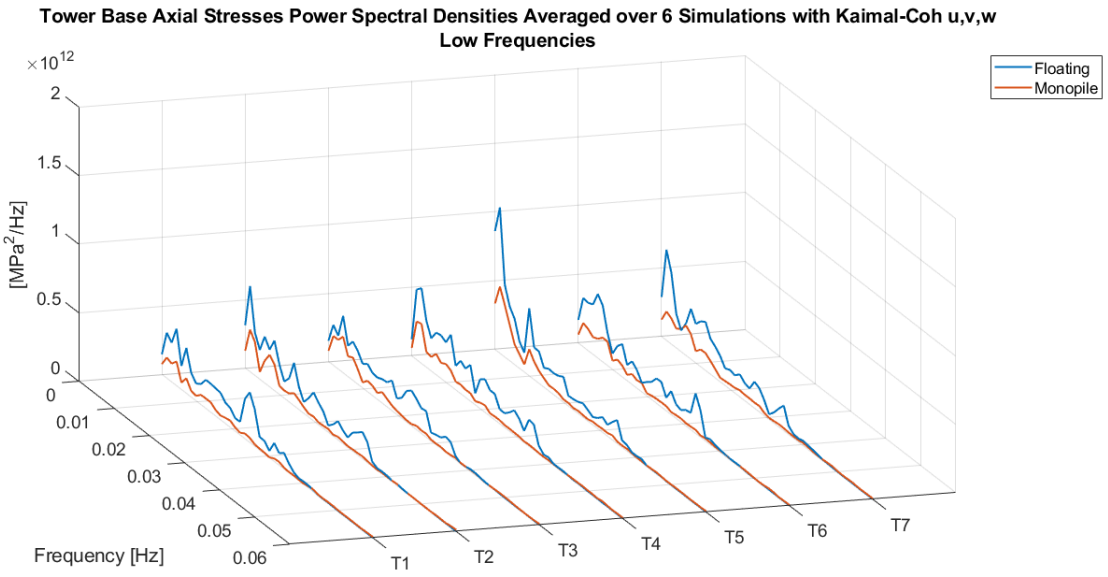

Figure 5.8: Tower base axial stresses power spectral density for each wind turbine and for both floating and monopile case, in the low-frequency range with *Kaimal-Coh u, v, w* turbulence.

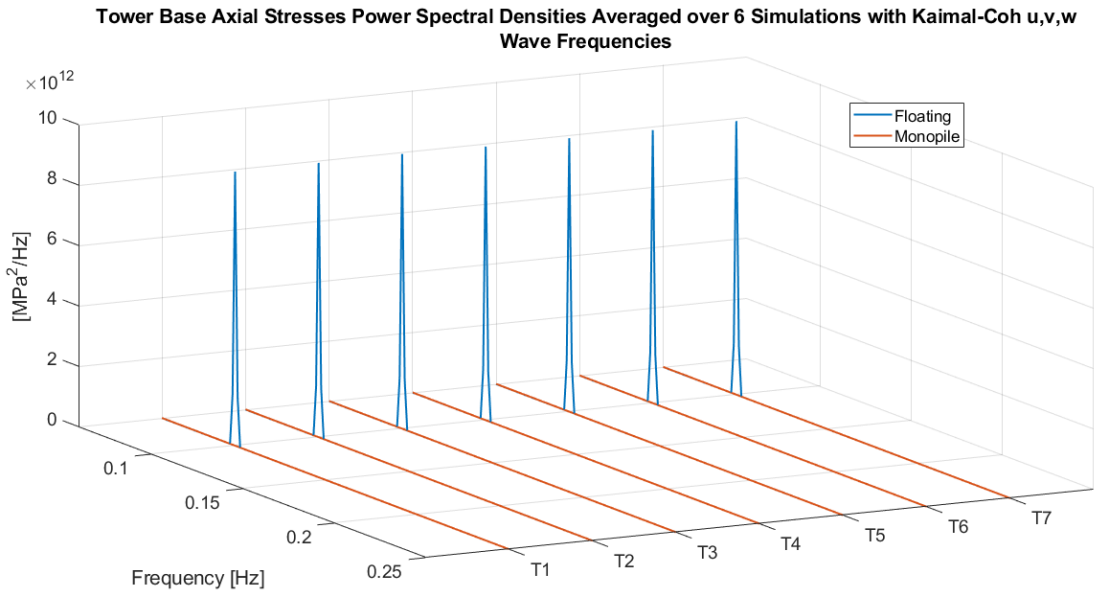

Figure 5.9: Tower base axial stresses power spectral density for each wind turbine and for both floating and monopile case, in the wave-frequency range with *Kaimal-Coh u, v, w* turbulence.

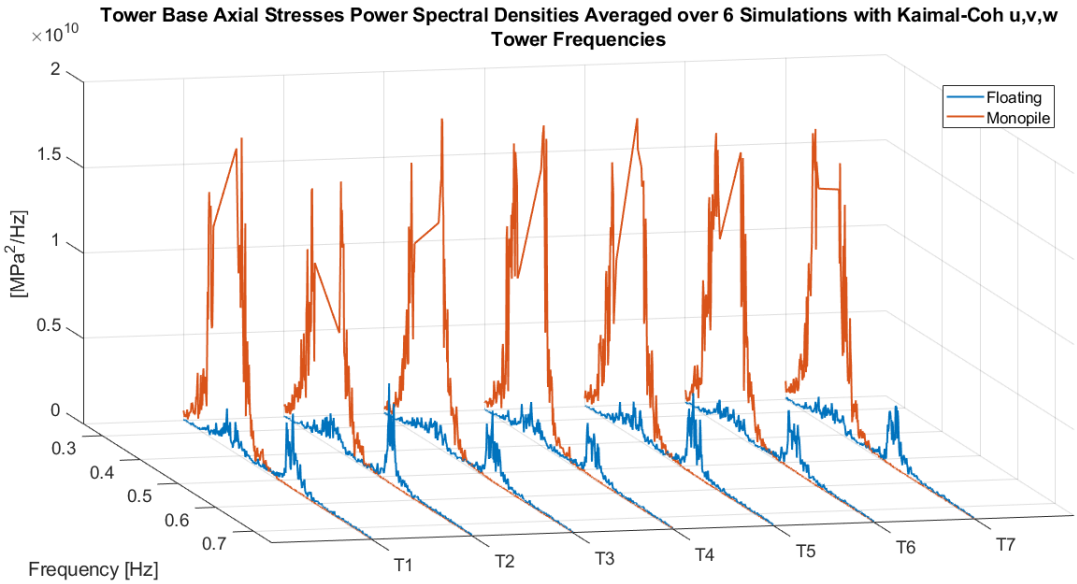

Figure 5.10: Tower base axial stresses power spectral density for each wind turbine and for both floating and monopile case, in the tower-frequency range with *Kaimal-Coh u, v, w* turbulence.

The same conclusions can be made for the axial stresses in the tower top, which however presents higher PSDs in each of the three frequency ranges (Figure 5.11, Figure 5.12, Figure 5.13), compared to the tower base ones.

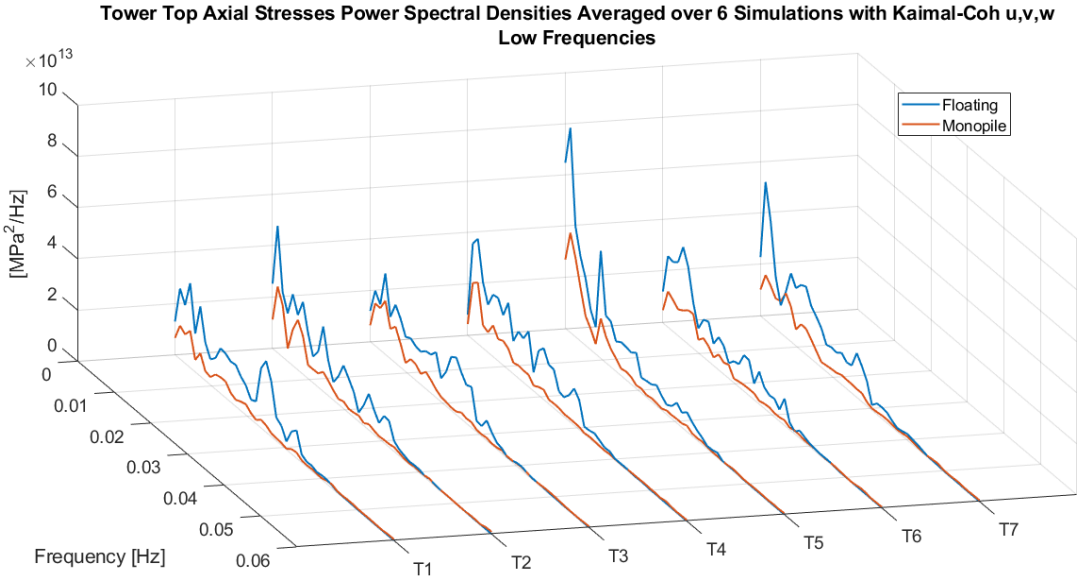

Figure 5.11: Tower top axial stresses power spectral density for each wind turbine and for both floating and monopile case, in the low-frequency range with *Kaimal-Coh u, v, w* turbulence.

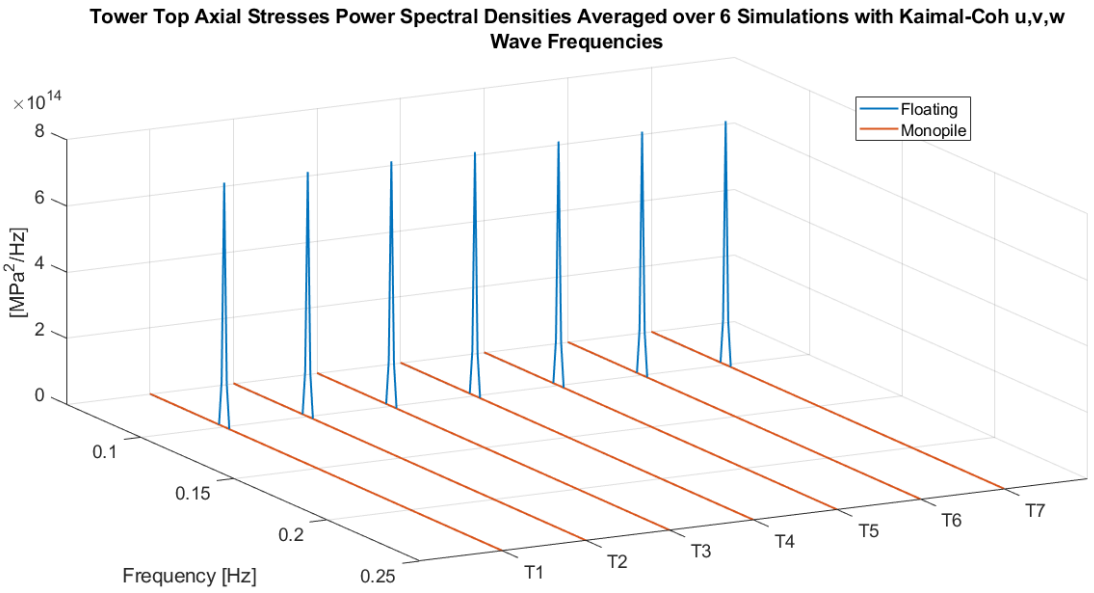

Figure 5.12: Tower top axial stresses power spectral density for each wind turbine and for both floating and monopile case, in the wave-frequency range with *Kaimal-Coh u, v, w* turbulence.

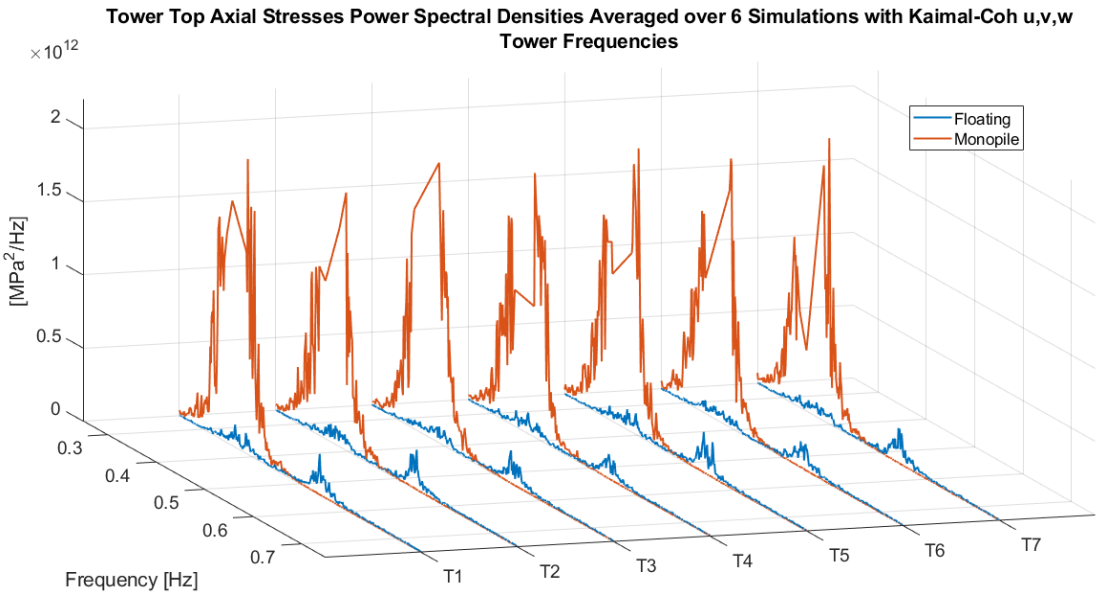

Figure 5.13: Tower top axial stresses power spectral density for each wind turbine and for both floating and monopile case, in the tower-frequency range with *Kaimal-Coh u, v, w* turbulence.

5.2.4. Fatigue Damages

The mean 1-h DELs for the combined roll and pitch moments at the tower base and top are shown in Figure 5.14. Their six-simulations averaged values are very similar for each wind turbines, even for the ones (T6 and T7) affected by the other turbines'

wakes, but are different among the two typologies of farm and also among tower base and top.

At the tower base the floating configuration is characterized by fatigue damages 22.21%–25.43% lower than the monopile ones, while at the tower top they are 14.36%–16.40% higher (biggest uncertainty: ±10.62%).

For the monopile case, the tower base is hence more sensitive, in terms of DELs, to the axial stresses in the 0.25Hz-0.70Hz range, which are higher for this farm typology (Section 5.2.3), while the tower top is more susceptible to the low-frequency axial stresses, higher for the floating case. The contrary is valid for the floating case, as a result of the previous analyses (Sections 3.2.5 and 4.2.5).

Moreover, at the tower top, the averaged DELs for the downstream turbines (T6 and T7) are slightly higher than the other turbines ones, for both the farm typologies. That indicates a more receptiveness, in terms of DELs, of the tower top to the wake meandering, with respect to the tower base.

It is also possible to note that DELs are one order of magnitude bigger for the tower base than for the top, for both the cases.

The tower axial force fatigue damages representation is left because they have been found to be much smaller than the moments ones, both for tower base and top and for both monopile and floating.

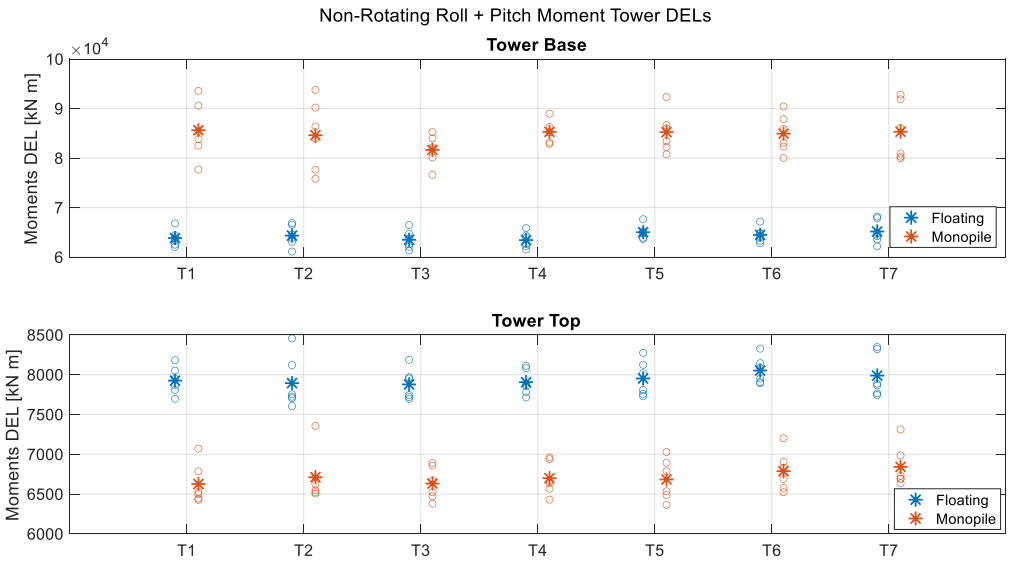

Figure 5.14: Tower base and top short-term DELs for each wind turbine and farm typology with *Kaimal-Coh u, v, w* turbulence. Each marker represents the mean value of one simulation except for the asterisk, which represents the average over the six simulation.

5.2.5. Power Coefficient and Extractable Power

In Figure 5.15, the mean power coefficient (c_p) of each simulation and its six-simulations averaged value are depicted in the floating and monopile cases for each turbine.

For the undisturbed turbines (T1, T2, T3, T4, T5) c_p is around 0.457-0.461 for the floating farm and around 0.461-0.465 for the bottom-fixed plant. For the waked ones (T6 and T7), instead, it is respectively 0.469 and 0.471 with the semisubmersible platform and 0.475 and 0.478 with the monopile support (biggest uncertainty: 1.66%).

The power coefficient is hence higher for the waked turbines and, for all the turbines, it is bigger in the bottom-fixed configuration compared to the floating one.

These differences among the two configurations are due to the different aerodynamic and to the control logic, tuned for the floating case but used also with the bottom fixed-one (Section 1.6).

The increase of c_p for T6 and T7 is due to the control logic too: the first five undisturbed rotors fall in the Region 3, which evidently starts for hub wind velocities a bit lower than the nominal ones (10.59 m/s) for security, while T6 and T7, "feeling" a lower wind velocity, fall in Region 2 (Section 1.6, Figure 1.6 (c)).

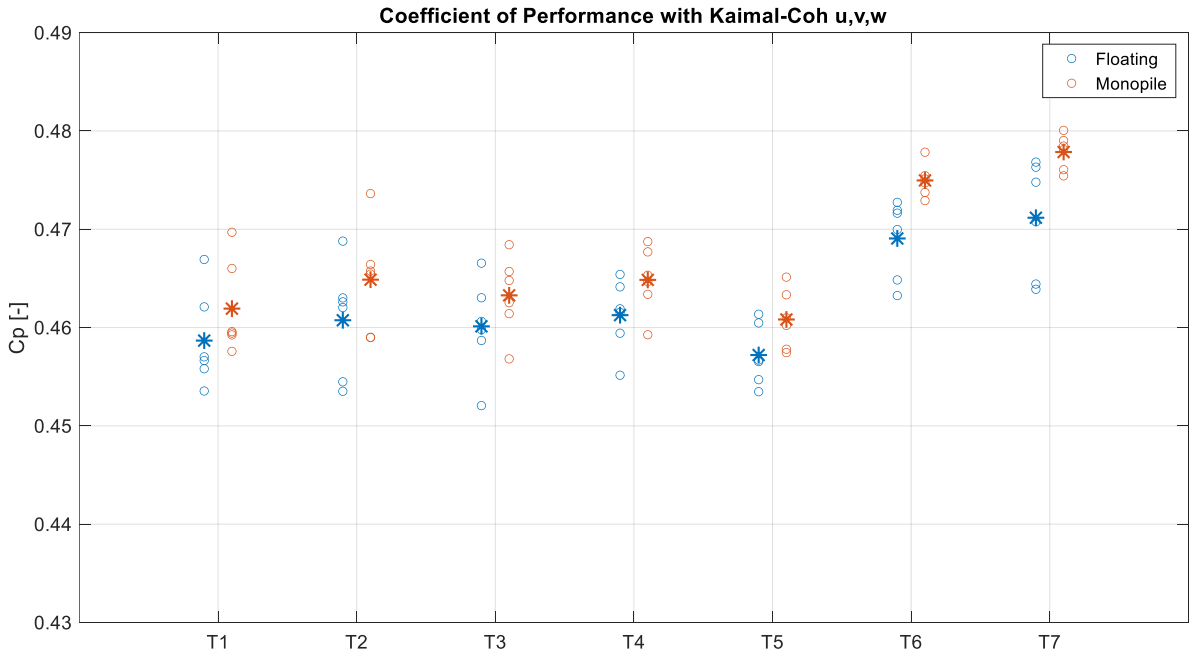

Figure 5.15: Power coefficient for each wind turbine and farm typology with *Kaimal-Coh u, v, w* turbulence. Each marker represents the mean value of one simulation except for the asterisk, which represents the average over the six simulation.

Figure 5.16, depicts, instead, the trend of the six-simulations averaged generator power of the entire plant in both the configurations. The nominal power and the ideal site power are shown too. The power time-history for the single simulations, instead, have not been represented to maintain the picture clear.

For the floating case the power is always lower than in the monopile case. That can be explained with the power formulation (Equation 5.1):

$$P(t) = \sum_{T=1}^{NTurb} \frac{1}{2} c_{P_T}(t) \rho_{air} A_D U_{hub_i}(t)^3 \eta_{mec} \eta_{el} \quad (5.1)$$

Where:

- t is the time;
- T is the turbine index;
- $NTurb$ is the number of aerogenerators in the plant;
- c_P is the power coefficient;
- ρ_{air} is the air density, set constant to 1.225 kg/m^3;
- A_D is the rotor disk area, constant among the two configurations;
- η_{mec} and η_{el} are respectively the mechanical and electrical efficiencies, both constant among the two farm typologies;
- U_{hub} is the hub horizontal wind velocity.

As shown before (Section 5.2.2) the horizontal hub wind velocity is identical for T1, T2, T3, T4 and T5 among the two cases. For T6 and T7, instead, a decrease, although very slight (of 2.76% and 2.49% respectively), is present from the floating to the monopile case. Even if the power has a cubic dependency on U_{hub}, the aforementioned reduction is compensated by the power coefficient, greater for the rotors in the monopile configuration (Figure 5.15).

Compared to the nominal plant power, which is constant to 105 MW since there are seven 15 MW rotors, the trend is anyway always substantially lower for both the farm typologies. This is because this analysis has been conducted at a reference hub-height velocity (10m/s) minor to the nominal one (10.59 m/s, Section 1.6) and also because the environmental conditions are different from the design ones. The ideal plant site power, instead, has been calculated with Equation 5.1 with $\eta_{el} = 0.9655$ (Section 1.2), η_{mec} assumed 0.98, c_P equal to the design one (0.489, Section 1.1) and $U_{hub}$to the reference site one (10m/s), and has been found to be 89.34 MW. It is almost always bigger than the real farms ones except in some instant. The first five undisturbed turbines, in fact, "feel" an hub wind velocity that in some instants is bigger than the reference one (Section 5.2.2). This is due to the randomization of the turbulent wind data.

From Figure 5.16 is also possible to note that for the floating case the power is characterized by more fluctuations, id est by a worse power quality, than in the

monopile plant. This is due to the higher hub turbulence intensity for the downstream turbines (T6 and T7), waked, in the floating case (Section 5.2.2).

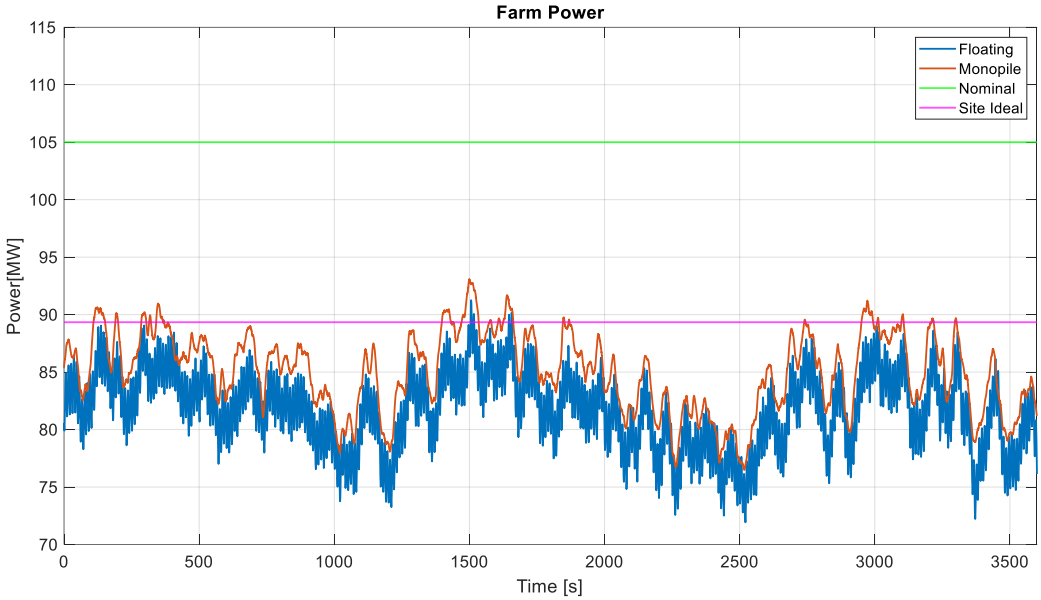

Figure 5.16: Time history of the six-simulations averaged plant generator power with *Kaimal-Coh u, v, w* turbulence for the floating and monopile case and nominal plant power.

5.3. Conclusions

The first conclusion is that, with the analysed hexagonal 5D staggered seven-turbines layout and *Kaimal-Coh u, v, w* turbulence, T6 and T7 are the only rotors waked. T1, T2, T3, T4 and T5 "feel", instead, the undisturbed turbulent flow at their hubs.

Comparing the floating and the monopile case under *Kaimal-Coh u, v, w* inflow, the first case is characterized by higher wake meandering, which mostly a low frequency phenomenum characterized by relevant uncertainty in its quantification.

For all the turbines in both cases the horizontal hub wind velocity deviations from the reference value (10 m/s) are really contained. The biggest reductions are obtained for the waked rotors (T6 and T7): respectively 1.86% and 2.37% with the semisubmersible platform and 1.98% and 2.66% with bottom-fixed substructure.

The monopile configuration is hence characterized by lower horizontal hub wind speed for the two most downwind turbines with respect to the floating case. This difference is anyway really slight and occurs just for T6 and T7, so it is compensated,

in terms of effect on the extractable power, by the coefficient of performances, smaller for all the turbines of the floating farm.

For both cases, anyway, it is always under the nominal one (105 MW), since the nominal wind speed (10.59 m/s) is higher than the site-reference one (10 m/s), and almost always lower than the ideal one 89.34 MW for this site.

Furthermore, for the waked turbines , the averaged hub TI, is also lower for the monopile case (of 2.76% for T6 and 2.49% for T7) compared to the floating one, despite the greater meandering, evidencing that TI is related to the platform motions and decreases by blocking its DOFs. This cause also the worse power quality in the floating layout than in the bottom-fixed one. In both farms, all the rotors present anyway reasonable values of hub TI for such a site.

At the end, it is possible to conclude that the monopile arrangement is better than the floating one for what concern the extractable power, but both are anyway characterized by good performances in these terms.

Considering the axial stresses at the tower base and top, instead, for each turbines the floating case present higher PSDs in the low-frequency range, compared to the monopile towers, and the peaks for the platform motions natural frequencies and for the waves, are visible just in the first case. The bottom-fixed turbines suffer, instead, of higher 3P excitation at both tower base and top.

The averaged 1-h moments DELs for the platform-based towers are 22.21%–25.43% lower than the monopile ones at the base, and 14.36%–16.40% higher at the top. Fatigue damages are anyway one order of magnitude bigger for the tower base than for the top and the axial stresses DELs are much smaller than the moments ones, for both the cases.

6 General Conclusions and Future Developments

In this master thesis the response of a hexagonal 5D staggered layout (Figure 4.2) wind farm composed by seven IEA 15-MW Floating Offshore Wind Turbines (Chapter 1) subjected to three different turbulence inflows, *Kaimal-Coh u, v, w*, *Kaimal-Coh u* and *Mann* (Section 3.1.4), and with the environmental conditions of a North-Sea site (Section 3.1.2), has been evaluated.

The farm operation has been simulated through FAST.Farm (Section 2.1) and the turbulent wind time-series data have been generated with TurbSim (Section 2.2.1) and Mann Turbulence Generator (Section 2.2.2).

The first step has been the study of a farm with two aligned turbines 8D distanced in order to reproduce the A. Wise and E. E. Bachynski wakes study [29] with some modifications on our turbine model; then the method has been applied to the plant configuration under analysis.

The last step has been a comparison between the floating farm and a monopile farm, with the same layout and environmental conditions, with *Kaimal-Coh u, v, w* turbulence, to draw further results.

The main conclusions of the study have been the following:

- The results of A. Wise and E. E. Bachynski wakes study [29] have been confirmed even for the analysed turbine model with some differences due to the different control logic.
- Within the analysed layout (Figure 4.2), the first five turbines (T1, T2, T3, T4 and T5) "feel" the undisturbed turbulent flow fields at their hubs, while just the two most downwind rotors, T6 and T7, operate in waked conditions.
- The flow field after the interaction with the plant, becomes characterized by wakes meandering, deflection and merging phenomena, which make it more randomized than it already was.
- The floating wind park under study is characterized by hub wind velocity values, which deviate just slightly from the reference wind speed, and by reasonable values of hub TI for the considered site. This is valid for all the rotors, even for the waked ones and with all the three turbulence typologies modelled.

- The platform motions of all the turbines, T6 and T7 included, are contained with all the turbulent inflows.
- This layout keeps the moments DELs, at the tower base and top and at the mooring lines fairleads, similar among the seven turbines and their wake-related increase for T6 and T7 negligible, with all the three inflows.
- The floating configuration, compared to an analogous monopile configuration, is characterized by more wake meandering behind its turbines and by a lower extractable power with less quality. Moreover its turbines are subjected axial stresses at the tower base and top which have an higher low-frequency response and present lower 3P excitations. The moments DELs are lower at the tower base and higher at the tower top, with respect to the ones of the bottom-fixed turbines

All things considered, the floating farm under study is valid from all the analyzed points of view. Using instead bottom-fixed turbines would be better, in terms of performance, but unfeasible with these environmental conditions; the water depth characterizing the site (200m) does not permit the installation of this type of technology.

In addition, the real main contributions of this master thesis have been those of increasing the robustness of the FAST.Farm (Section 2.1) use and developing models for the future studies of Politecnico di Milano's Galleria del Vento. They are, in fact, focusing on the offshore floating wind energy, contributing to the spread of this promising technology, and so to the decarbonisation.

This type of analysis opens to several future developments:

- It could be, for example, applied to different and more complex layouts, taking in consideration also economical parameters to identify the optimal geometry.
- The FAST.Farm, TurbSim and Mann Turbulence Generator spatial and temporal resolutions can be improved, to obtain more precise results with less uncertainty. The resolution, and the related computational cost for the simulations, has been in fact the main limitation of this work.
- Imposed motions can be applied to the platforms in order to reduce the wakes effect on the most downstream turbines or to avoid it at all.
- The response with different floating supports can be investigated.

Bibliography

[1] TERNA, "La produzione totale nazionale netta oraria, suddivisa per fonti primarie, compreso l'autoconsumo," [Online]. Available: https://www.terna.it/it/sistema-elettrico/transparency-report/actual-generation.

[2] TERNA, «L'andamento del fabbisogno totale del sistema elettrico italiano,» [Online]. Available: https://www.terna.it/it/sistema-elettrico/transparency-report/installed-capacity .

[3] Ministero dello Sviluppo Economico, Ministero dell'Ambiente e della Tutela del Territorio e del Mare, Ministero delle Infrastrutture e dei Trasporti, "PIANO NAZIONALE INTEGRATO PER L'ENERGIA E IL CLIMA," Dicembre 2019. [Online]. Available: https://www.mise.gov.it/images/stories/documenti/PNIEC_finale_17012020.pdf.

[4] TERNA, «La capacità installata degli impianti di generazione,» [Online]. Available: https://www.terna.it/it/sistema-elettrico/transparency-report/installed-capacity.

[5] Statista, «Total installed wind power capacity in Italy from 2012 to 2022,» 2022. [Online]. Available: https://www.statista.com/statistics/421815/wind-power-capacity-in-italy/#:~:text=The%20total%20installed%20wind%20power%20capacity%20of%20Italy,in%20regions%20such%20as%20Apulia%2C%20Sicily%2C%20and%20Campania.

[6] FRAUNHOFER INSTITUTE FOR SOLAR ENERGY SYSTEMS ISE, «LEVELIZED COST OF ELECTRICITY RENEWABLE ENERGY TECHNOLOGIES,» June 2021. [Online]. Available: https://www.ise.fraunhofer.de/content/dam/ise/en/documents/publications/studies/EN2021_Fraunhofer-ISE_LCOE_Renewable_Energy_Technologies.pdf.

[7] NREL, «Annual Technology Baseline,» [Online]. Available: https://atb.nrel.gov/electricity/2022/offshore_wind.

[8] E. Gaertner, J. Rinker, L. Sethuraman, F. Zahle, B. Anderson, G. Barter, N. Abbas, F. Meng, P. Bortolotti, W. Skrzypinski, G. Scott, R. Feil, H. Bredmose, K. Dykes, M. Shields, C. Allen, and A. Viselli, «Definition of the IEA 15-Megawatt Offshore Reference,» 2020. [Online]. Available: https://www.nrel.gov/docs/fy20osti/75698.pdf.

[9] C. Allen, A. Viselli, H. Dagher, A. Goupee, E. Gaertner, N. Abbas, M. Hall and G. Barter, "Definition of the UMaine VolturnUS-S Reference Platform Developed for the IEA Wind 15-Megawatt Offshore Reference Wind Turbine," University of Maine, National Renewable Energy Laboratory, July 2020. [Online]. Available: NREL/TP-5000-76773. https://www.nrel.gov/docs/fy20osti/76773.pdf.

[10] National Renewable Energy Laboratory, «ROSCO. Version 0.1.0,» 2019. [Online]. Available: https://github.com/NREL/rosco.

[11] L. Abbas, J. Nikhar, Wright, D. Alan, Pao, «An Update to the National Renewable Energy Laboratory Wind Turbine,» February 2020. [Online]. Available: https://www.osti.gov/biblio/1601147.

[12] Garrett Barter et Al., "15MW reference wind turbine repository developed in conjunction with IEA Wind," February 2022. [Online]. Available: https://github.com/IEAWindTask37/IEA-15-240-RWT.

[13] J. Jonkman a. K. Shaler, "FAST.Farm User's Guide and Theory Manual," National Renewable Energy Laboratory, 2021. [Online]. Available: https://www.nrel.gov/docs/fy21osti/78485.pdf.

[14] M. L. Buhl Jr., J. M. Jonkman, «FAST User's Guide,» National Renewable Energy Laboratory, United States, August 2005.

[15] G. C. Larsen, H. A. Madsen, K. Thomsen, T. J. Larsen, "Wake meandering: a pragmatic approach," 7 April 2008. [Online]. Available: https://doi.org/10.1002/we.267.

[16] B. J. Jonkman, «TurbSim User's Guide v2.00.00,» National Renewable Energy Laboratory, 1 June 2016. [Online]. Available: https://www.nrel.gov/wind/nwtc/assets/downloads/TurbSim/TurbSim_v2.00.pdf.

[17] K. Siegrist, «Non-homogeneous Poisson Processes,» LibreTexts Statistics, April 2022. [Online]. Available: https://stats.libretexts.org/Bookshelves/Probability_Theory/Probability_Mathematical_Statistics_and_Stochastic_Processes_(Siegrist)/14%3A_The_Poisson_Process/14.06%3A_Non-homogeneous_Poisson_Processes.

[18] k. Siegrist, «The Lognormal Distribution,» LibreTexts Statistics, April 2022. [Online]. Available: https://stats.libretexts.org/Bookshelves/Probability_Theory/Probability_Mathematical_Statistics_and_Stochastic_Processes_(Siegrist)/05%3A_Special_Distributions/5.12%3A_The_Lognormal_Distribution.

[19] Technical University of Denmark, «Command-line Version of Mann 64bit Turbulence Generator,» 22 August 2018. [Online]. Available: https://www.hawc2.dk/-/media/sites/hawc2/hawc2-download/pre-processing-tools/mann_turb_x64.zip?la=da&hash=F0E221C7213AA61E3BF3B31092D261C5A0EC730E.

[20] Technical University of Denmark, «HAWC2; Pre-processng tools,» [Online]. Available: https://www.hawc2.dk/download/pre-processing-tools.

[21] J. Mann, «The Spatial Structure of Neutral Atmospheric Surface-Layer Turbulence,» 1994. [Online]. Available: https://doi.org/10.1017/S0022112094001886.

[22] L. Dong, W. Hou Lio, E. Simley, «On turbulence models and lidar measurements for wind turbine control,» 2021. [Online]. Available: https://doi.org/10.5194/wes-6-1491-2021.

[23] J. Mann, «Wind field simulation,» 1998. [Online]. Available: https://doi.org/10.1016/S0266-8920(97)00036-2.

[24] G. K. Batchelor, The Theory of Homogeneous Turbulence, Cambridge: Cambridge University Press, 1953.

[25] T. v. Kármán, «Progress in the Statistical Theory of Turbulence,» 1 November 1948. [Online]. Available: https://doi.org/10.1073/pnas.34.11.530.

[26] International Electrotechnical Commission, «IEC: Wind energy generation systems – Part 1: Design requirements,» Geneva, Switzerland, 2019.

[27] G. J. Hayman, «MLife Theory Manual for Version 1.00,» National Renewable Energy Laboratory, 19 October 2012. [Online]. Available: https://www.nrel.gov/wind/nwtc/assets/pdfs/mlife-theory.pdf.

[28] International Electrotechnical Commission, «Wind Turbines – Part 1: Design requirements,» IEC 61400-1 Ed.3, 2005.

[29] A. Wise, E. E. Bachynski, "Analysis of wake effects on global responses for a floating two-turbine case," 16th Deep Sea Offshore Wind R&D conference, 2019. [Online]. Available: https://doi.org/10.1088/1742-6596/1356/1/012004.

[30] C. Bak, F. Zahle, R. Bitsche, T. Kim, A. Yde, L. C. Henriksen, M. H. Hansen, J. P. A. A. Blasques, M. Gaunaa, A. Natarajan, "The DTU 10-MW Reference Wind Turbine," EventDanish Wind Power Research 2013 - Trinity, Fredericia, Denmark, 2013. [Online]. Available: https://orbit.dtu.dk/en/publications/the-dtu-10-mw-reference-wind-turbine.

[31] Q. Wang, Design and dynamic analysis of a steel pontoon-type semi-submersible floater supporting the, Master's thesis NTNU/TU Delft, 2014.

[32] L. Li, Z. Gao, T. Moan, «Joint Distribution of Environmental Condition at Five European Offshore Sites for Design of Combined Wind and Wave Energy Devices,» Journal of Offshore Mechanics and Arctic Engineering, 2015. [Online]. Available: https://doi.org/10.1115/1.4029842.

[33] International Electrotechnical Commission (IEC), "Wind turbines: Part 3: Design requirements for offshore wind turbines," Tech. Rep. IEC61400-3, 2009.

[34] Y. Ma, P. Martinez-Vasquez, C. Baniotopoulos, «Buckling Analysis for Wind Turbine Tower Design: Thrust Load Versus Compression Load Based on Energy Method,» ResearchGate, October 2020. [Online]. Available: https://doi.org/10.3390/en13205302.

[35] E. Bachynski, L. Eliassen, "ASME 2017 36th International Conference on Ocean, Offshore and Arctic," in *no OMAE2017-61179*, Trondheim, Norway, 2017.

[36] E. E. Bachynski, L. Eliassen, "The effects of coherent structures on the global response of floating offshore wind turbines," Wind Energy, 30 October 2018. [Online]. Available: https://doi.org/10.1002/we.2280.

[37] S. Lee, M. J. Churchfield, P. J. Moriarty, J. Jonkman, J. Michalakes, "A Numerical Study of Atmospheric and Wake Turbulence Impacts on Wind Turbine Fatigue

Loadings," Journal of Solar Energy Engineering, 3 August 2013. [Online]. Available: https://doi.org/10.1115/1.4023319.

[38] TotalControl, « Reference Wind Power Plant,» Deliverable no.: D1.03, 13 April 2018. [Online]. Available: https://www.totalcontrolproject.eu/-/media/sites/totalcontrol/publications/public-deliverables/totalcontrol-d1-03-reference-wind-farm.pdf?la=da&hash=8396213B7D998E73A1914ED35FE203581C5DD62A.

List of Figures

List of Tables

List of symbols

Variable	Description	SI unit
c_p	Power coefficient	-
TSR	Tip speed ratio	-
U_{hub}	Horizontal hub wind velocity	m/s
t	time	s
t_{pre}	Pre-simulation end time	s
Δt	FAST.Farm discrete time step	s
dr	FAST.Farm wake dynamics grid radial increment	m
$NumRadii$	FAST.Farm wake dynamics grid number of nodes	-
U_h	Horizontal ambient wind speed at a generic height	m/s
$Uref$	Horizontal ambient wind speed at a reference height	m/s
h_h	Generic height	m
h_{ref}	Reference height	m
α_{PL}	Power law exponent	-
Coh_{i,j_k}	Spatial coherence between two points i and j for the k velocity component	-
r_{ij}	Distance between points i and j	m
f	Cyclic frequency	Hz
a_k	Coherence decrement parameter for the k velocity component	-
b_k	Coherence offset parameter for the k velocity component	m^{-1}
V_{advect}	Hub height average wind speed	m/s
$\Phi_{i,j}$	Spectral tensor	$(m/s)^2/Hz$
K	Non dimensional spatial wave number	-
$\bar{U}$	Mean wind speed	m/s
$\delta_{i,j}$	Dirac's delta function between the points i and j	-
E	Energy Spectrum	m^3/s^2

α	Kolmogorov constant	s^{-1}
ϵ	specific turbulent kinetic energy viscous dissipation	m^2/s^3
L	Length scale	m
Γ	Eddies lifetime-related non-dimensional parameter	-
D_j^{ST}	Short-term accumulated damage for the time-series j	~
n_{ji}	Extrapolated cycle count for the i^{th} cycle and j^{th} time-series	-
N_{ji}	Number of cycles to failure	-
L^{ult}	Ultimate design loas	~
L^{MF}	Fixed-load mean	~
m	Whöler exponent	-
L_{ji}^{RF}	Load range of the cycle about a fixed load-mean value	~
n_j^{STeq}	Total equivalent fatigue counts for time-series j	-
f^{eq}	Damage equivalent load frequency	Hz
T_j	Elapsed time of time-series j	s
N_j^{eq}	Equivalent number of cycles until failure for the j^{th} time-series	-
DEL_j^{STF}	Short-term DEL for time-series j about a fixed mean	~
D	Rotor disk diameter	m
Δx	FAST.Farm spatial step in x direction	m
Δy	FAST.Farm spatial step in y direction	m
Δz	FAST.Farm spatial step in z direction	m
r	Circular cross-section radial coordinate	m
r_e	Circular cross-section external radius	m
r_i	Circular cross-section internal radius	m
θ	Circular cross-section angular coordinate	°
σ	Axial stresses	Pa
A	Cross-sectional area	m^2
π	Pi-greco	-
N_z	Axial force	N
M_x	Roll or side-to-side moment	N m
M_y	Pitch or fore-aft moment	N m
I_x	x second moment of area	m^4
I_y	y second moment of area	m^4

D_{nc}	Nominal chain diameter of the mooring lines	m
TI	Turbulence intensity	%
P	Generator power	W
ρ_{air}	Air density	Kg/m^3
A_D	Rotor disk area	m
η_{mec}	Mechanical efficiency	-
η_{el}	Electrical efficiency	-
T	Turbine index	-
$NTurb$	Number of wind turbines in the farm	-

Acknowledgments

I primi ringraziamenti vanno sicuramente a mia madre e mio padre. Grazie per avere permesso il mio percorso di studi, con sacrifici non scontati, credendo sempre nelle mie possibilità e lasciandomi sempre scegliere da solo ciò che volessi fare. Se sono riuscito ad arrivare fin qua è perché siete sempre stati presenti. Spero, nel mio lavoro, di essere bravo quanto voi lo siete nel vostro. Se c'è una cosa che ho sempre pensato è infatti che voi eccelliate nel vostro lavoro e che continuiate ad eccellere anche ora, nonostante vi manchino pochi anni alla pensione. Inoltre sappiate che nella vita siete e sarete sempre per me un modello di comportamento e di onestà. Non c'è modo di ringraziarvi ma… grazie, veramente.

Ringrazio la Professoressa Sara Muggiasca per avermi concesso, anche senza conoscermi, l'opportunità di svolgere la tesi nell'ambito ingegneristico che più mi appassiona.
Ringrazio Alessandro per avermi seguito con attenzione durante tutto il lavoro, avendo sempre la risposta per i miei dubbi, e per avermi lasciato usare i computer della Galleria.
Un sentito grazie va anche a Marco, anche lui sempre disponibile, tempestivo ed amichevole nel rispondere ai miei chiarimenti.

Grazie Ila e Marty. Sappiate che è fin dall'infanzia che prendo i vostri passi come ispirazione. Non potrebbe che essere riduttivo esprimere il mio attaccamento e affetto nei vostri confronti a parole.

Concludo ringraziando i miei amici, parte importantissima della mia vita. Grazie per esserci, per il supporto e per avere rappresentato una valvola di sfogo durante questo percorso.

Alessio